ROTATIONAL EFFECTS ON TURBINE BLADE COOLING

by

Pamela S. Barry

B.S., Aeronautical Engineering
Rensselaer Polytechnic Institute, 1991

SUBMITTED TO THE DEPARTMENT OF
AERONAUTICS AND ASTRONAUTICS IN PARTIAL
FULFILLMENT OF THE REQUIREMENTS FOR THE
DEGREE OF
MASTER OF SCIENCE

at the

MASSACHUSETTS INSTITUTE OF TECHNOLOGY

May 1994

Signature of Author _____
Department of Aeronautics and Astronautics
May 17, 1994

Certified by _____
Professor Jack. L. Kerrebrock
Richard Cockburn Maclaurin Professor of Aeronautics and Astronautics
Thesis Supervisor

Accepted by _____
Professor Harold Y. Wachman
Chairman, Department Graduate Committee

Rotational Effects on Turbine Blade Cooling

by
Pamela S. Barry

Submitted to the Department of Aeronautics and Astronautics
on May 16, 1994 in partial fulfillment of the requirements
for the Degree of Master of Science in
Aeronautics and Astronautics

Abstract:

An experimental study was performed to determine the effects of rotation on turbine blade cooling. The method of cooling under investigation was convection cooling in the first outward-flowing channel of a convection cooling system with the external heat transfer to the model being simulated by imposing a constant heat flux on the model. Rotational effects were induced by rotating the model about an orthogonal axis. The effects of rotation were examined for three different models, a smooth square tube, a smooth rectangular tube and a ribbed rectangular tube.

Experiments were performed for ranges of Reynolds number and buoyancy parameter not examined previously. Further, the experiment utilized a technique that was able to obtain a level of resolution which is much finer than existing data. The results showed that the experimental technique was able to reproduce, within experimental accuracy, the results obtained by other researchers.

The results showed that the heat transfer generally increased on the leading and trailing surface with increased buoyancy parameter for all three models. The actual heat transfer distribution and magnitude of the heat transfer rate depended on the geometry and internal surface conditions of the model. The ribbed rectangular tube showed considerable heat transfer enhancement over the smooth rectangular tube and the smooth square tube. The relative trailing/leading Nusselt number however, was found to be lower for the square model than either of the rectangular models. For each model, evidence of the coupling between the buoyancy forces and Coriolis forces could be seen as the rotation was increased, the effects developing as the flow proceeded outward from the axis.

Thesis Supervisor: Professor Jack L. Kerrebrock
Title: Richard Cockburn Maclaurin Professor of Aeronautics and Astronautics

Acknowledgements

First and foremost, I would like to thank Professor Kerrebrock for taking me on as a research assistant and for introducing me to experimental work. Professor Kerrebrock has been a constant source of support and encouragement. His guidance and trust in me has given me the opportunity to realize that I can accomplish more then I ever thought I could.

Next, I would like to thank Andrew Jones for all of the long, and sometimes frustrating hours, he spent working in the lab as we tried to get the experiment up and running and then as we spent taking data. The experiment works and it works very well. Andrew's outlook and personality made even the long days go by faster. I am also grateful to Gerry Guenette and the GTL staff for continuously providing invaluable advice and assistance.

I would also like to extend my appreciation to General Electric, for funding this research, and to Alan Maddaus and Fred Staub, of General Electric, for their direction and valuable insight into turbine blade cooling.

In addition, I am indebted to Professor Trilling for giving me the opportunity to attend MIT by providing the first year of funding, and to Bob Knowlden of Lincoln Laboratory for helping me design the optical system which is currently being used.

Finally, I would like to express my gratitude to my family and especially to Daniel Clancy, for their endless supply of love, encouragement and support.

Table of Contents

List of Tables

List of Figures

Chapter 1
Introduction

1.1 Introduction

Turbine blades, in air and land based gas turbine engines, are subjected to extremely high external flow pressures and temperatures. In order for a turbine blade to endure these harsh conditions the blades need to be cooled. Turbine blades are cooled by applying a combination of techniques such as impingement cooling, film cooling, and internal convection cooling. Employment of these cooling techniques enables the surface of the blade to be kept a few hundred degrees lower then the external flow temperature.

Improving gas turbine engines often implies higher external flow temperatures, higher stage pressure ratios and faster rotor speeds, all of which increases the demands on turbine blades. As a result, efficient cooling of turbine blades becomes exceedingly important as engineers strive to improve gas turbine engines. To provide the engineer with knowledge to design efficient cooling systems different research activities have been established. The research described in this thesis is focused on collecting data for the first passage of an internal convection cooling system. In internal convection cooling, channels, that travel up and down the inside of the turbine blade, are used to pass low temperature flow through the inside of the blade. A schematic of typical internal cooling passages is presented in figure 1.1. The low temperature flow convectively removes the heat from the blade material. Since convection is the process that removes the heat from the blade the local heat transfer coefficient of the passage is the most important parameter to the designer.

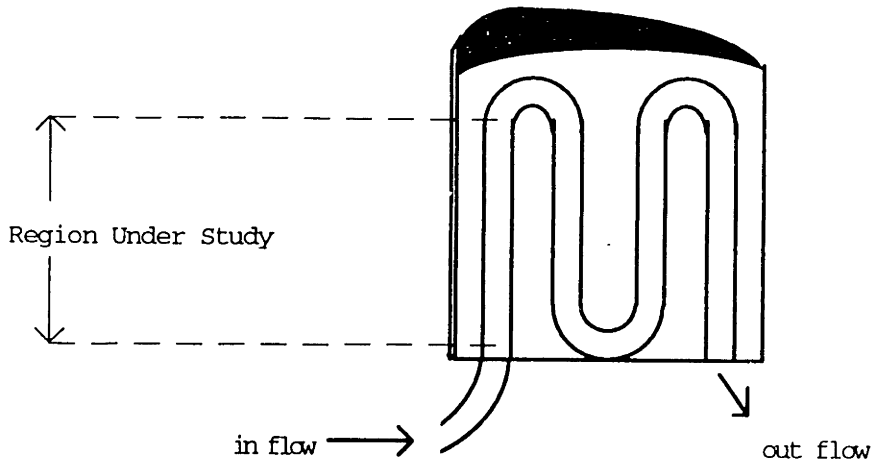

Figure 1.1 Conceptual Schematic of Convective Cooling Passages in a Turbine Blade

1.2 Background

In the past, engineers have used heat transfer predictions based on stationary conditions to design cooling passages. However, under rotation the heat transfer characteristics of the passage are significantly altered due to Coriolis and buoyancy driven secondary flows. To account for rotational effects engineers would apply adjustment factors to the stationary data to make it applicable to actual engine conditions. This approach, however, is unsatisfactory when designs outside the range of past experience are necessary.

The current experiment aims to generate a database of these correction factors for a much wider range of operating conditions than is currently available. The results are presented in terms of a Nusselt Number ratio, Nu/Nu_{∞}, where Nu, the measured local Nusselt number, and Nu_{∞}, the Nusselt number predicted by stationary correlations, are based on the same thermodynamic properties. This ratio provides the required extension from stationary to rotating conditions.

A large number of experiments have been conducted for the purpose of investigating the effects of rotation on cooling passages. References [1]-[5],[7], and [9]-[13], comprise a small sample of the literature available. Hwang et. al. [5], has compiled a chart of past experiments that have been performed. The current research will be compared to the results presented by Wagner et. al. [11]-[13], Han et.al. [3]-[4], and Guidez [1]. In addition, reference will be made to [2] as being "Wagner data" but was

published under the authors Hajek, Wagner et. al. Comparisons were focused on these authors since other researchers were not able to get significant rotation numbers at Reynolds number on the order of 25,000 - 50,000.

Previous experiments, are classified according to the method used to simulate the external heat transfer to the blade. In the experiments the heat transfer is simulated either by keeping the passage at a constant temperature or by enforcing a constant heat flux. The present experiment uses a constant heat flux, Wagner et.al, used a constant temperature channel, Guidez used a constant heat flux, and Han et.al. performed experiments with constant heat flux and constant temperature channels. In actuality, the external heat transfer to the convective cooling channels is neither purely constant heat flux nor purely constant temperature. Rather, the external heat transfer is a combination of the two extremes, the combination being prescribed by the details of the thermal and mechanical design of the blade.

Researcher	Re	Ro	Density Ratio	Buoyancy Parameter	External Heat Transfer
Wagner	12,500 - 50,000	0.0 - 0.48	0.0 - 0.22	0.0 - 1.4	const. Temp.
Han	2,500 - 25,000	0.0 - 0.35	0.06 - 0.1	0.0 - 0.6	const. Temp. const. Flux
Guidez	17,000- 41,000	0.02 - 0.20	not avail.	not avail.	const. Flux
GTL	25,000- 114,000	0.04 - 0.64	0.21-0.36	0.04-5.59	const. Flux

The results from each experiment are correlated in terms of various parameters including rotation number, Reynolds number, density ratio and buoyancy parameter. The buoyancy parameter includes the rotation number and density ratio. Each parameter is discussed further in Chapter 3.

Wagner et al found that the heat transfer on the trailing surfaces increased with increased rotation. For example, as the rotation number was increased from 0.12 to 0.48 the heat transfer increased from approximately 1.5 to almost 4 times the stationary heat transfer. In addition, Wagner discovered that the heat transfer on the leading surface

decreases and then increases with increased rotation. Further, Wagner et al showed that the heat transfer is correlated well by the buoyancy parameter for locations far downstream of the inlet.

Han et al showed that there is a significant difference in the internal heat transfer distribution when the external heat transfer is simulated by maintaining the channel at a constant heat flux as compared to maintaining a constant temperature. The local internal heat transfer for the constant heat flux experiment is 10-20% larger on the trailing surface and 40-80% larger on the leading surface than the results for a constant temperature passage. The difference stems from the internal flow temperature gradient that results in the channel. This difference will also be discussed in Chapter 3.

The findings of Wagner, Han and others show the same general trends. The results of the research described in this thesis are consistent, under similar test conditions, with the general results obtained by Wagner, Han and others. This present research, however, goes further and presents results for operating conditions outside of the range tested by other researchers. Data is obtained for larger buoyancy parameters, larger rotation numbers and larger Reynolds number than previously reported as can be seen from the above chart. Further, the results are presented for models representing three types of cooling passages, a smooth square channel, a smooth rectangular channel and a rectangular channel that has turbulators. Where appropriate, comparisons are made with the results of other researchers.

A major difference between the current work and that of others is the detail that is obtainable with the surface temperature measurement system employed. The experiments of Wagner, and Han use thermocouples and heaters in sections of the channel wall to measure the channel surface temperature and heat flux. Guidez heated the model by a radiative furnace but also measured the wall temperature with thermocouples. As a result, they were limited to four radial regions per side where they could ascertain the heat transfer coefficient as pictured in figure 1.1a. The present research uses an infrared detector to determine the channel surface temperature, the heat flux being fixed by resistance heating of the channel walls. This method enables the experiment to determine the heat transfer coefficient with a resolution on the order of 1 mm (figure 1.1b). With this resolution, heat transfer distribution maps which are able to show the heat transfer distribution on the entire surface of the model are possible.

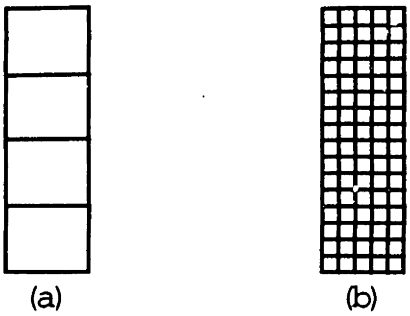

Figure 1.2 Comparison between the current resolution and the resolution of published data. [a] Wagner, Han, Guidez and others were able to obtain heat transfer data for approximately four regions per side. (b) Present research can obtain heat transfer data for a larger number of smaller sized regions.

1.3 General Approach

The experiment is designed to study the heat transfer coefficient on the inside of the first radial passage of an internal convective cooling system. Simulation of a cooling passage requires a channel that can be heated, to represent the external heat flux, and cooled internally with a cooling flow while rotating at high speeds. The cooling passage is represented by a thin-walled metal tube. Throughout this thesis, the thin-walled metal tubes that represent different types of cooling passages shall be referred to as "models". To give a feel for the size of the channels of interest, one of the models is a four (4) inch long, quarter (1/4) inch wide, square channel. The material of the model is such that the external heat transfer to the turbine blade is simulated by passing current through the model. Freon is passed through the model as the cooling flow and rotation of the model is obtained by placing the model on a shaft which rotates at high speeds in a vacuum chamber.

The local heat transfer coefficient is calculated from an energy balance that relates the energy supplied to the model to the energy absorbed by the bulk cooling flow. In performing the heat balance, the amount of current passing through the channel wall, the cooling mass flow rate, the model's interior surface temperature and the bulk cooling temperature, are required. In the experiment the current level and the cooling mass flow rate are directly measured. The model's interior wall temperature is assumed to be equal to the exterior wall temperature due to the thinness of the model and the exterior wall

temperature is directly measured. The bulk temperature used in the local heat balance includes the temperature rise of the cooling flow as it travels along the model. The local bulk temperature is calculated by assuming a linear variation of bulk temperature from the inlet to the outlet. The inlet and outlet bulk temperatures are directly measured.

Chapter 2
Experimental Approach

2.1 Fundamental Experimental Concept

Under rotation, Coriolis and buoyancy driven secondary flows complicate the coolant flow structure as it passes through a convectively cooled channel. These secondary flows greatly alter the heat transfer characteristics of the channel. Engineers designing cooling channels need more information on the effects of rotation, buoyancy parameter, density ratio and Reynolds number on heat transfer in order to design more efficient convective cooling systems.

The experiment is designed to simulate the first channel of an internal convective cooling system. The channel is represented by a thin-walled metal tube that is referred to as a "model" throughout this thesis. Each model is made of Nichrome 80-20. The heat transfer to the channel is simulated by passing current through the model's walls. Nichrome 80-20 has nearly constant resistance and thermal conductance with temperature. Each model is four inches long and is placed on one end of a 32 inch diameter rotor. The rotor's rotational speed is controlled by a variable speed motor and is monitored by counting the number of pulses emitted by Channel A of an optical encoder. An oil free compressor circulates Freon through the heated channel. Thermocouples are used to measure the bulk inlet and outlet temperature of the cooling flow. The model's surface temperature is determined using an infrared detector. A set of curved mirrors, which constitutes an all-reflective telescope, focuses the radiation from each point on the model, onto the detector element. The detector element is a 1mm x 1mm square. A schematic of the imaging process is shown in figure 2.1.

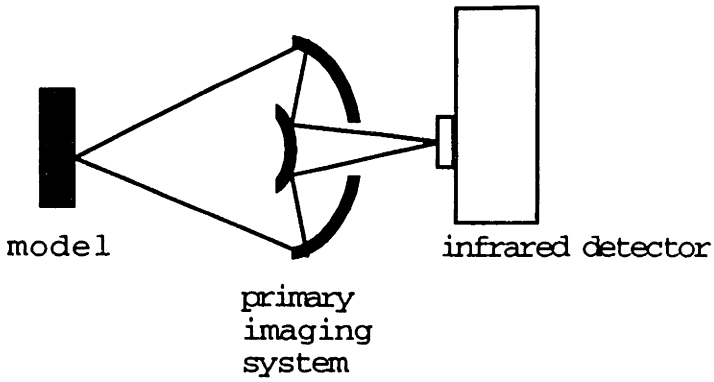

Figure 2.1. Side View of the Primary Imaging System Focusing a cone of radiation from the Side Front surface onto the infrared detector.

The front surface of the model is in clear view of the infrared detector. However, in order to collect the radiation from the leading, trailing and back surfaces of the model, flat mirrors behind the model are used to redirect the cone of radiation. Figure 2.2 shows an example of how the radiation is reflected for one of the side surfaces.

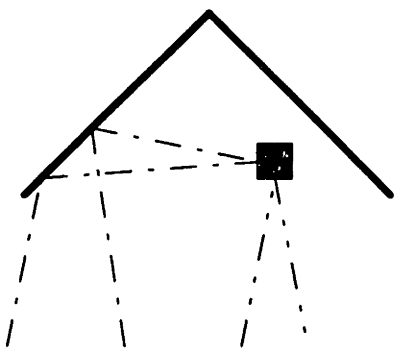

Figure 2.2 Example of how the flat mirrors redirect the cone of radiation from non side front surfaces

The imaging system provides a level of detailed information on local heat transfer characteristics not previously reported.

From the energy supplied to the model, the coolant mass flow rate, the model's surface temperature and the local bulk temperature of the cooling flow an energy balance can be applied to find the local heat transfer coefficient distribution on the model. Below is the heat balance applied to one element of the model.

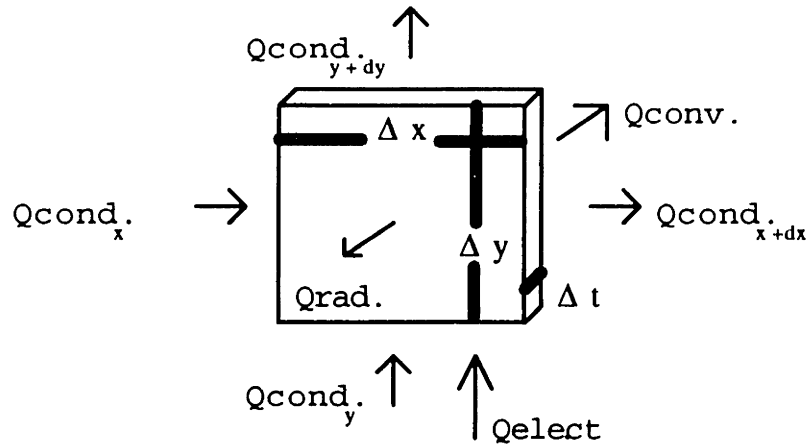

The overall heat balance for an element relates the energy entering the element to the energy leaving the element. The heat balance equation in it's most general form is written below.

$$(I^2R_f/A_f)*\Delta x*\Delta y = -\Sigma\, k\,(\Delta T/\Delta S)*\Delta t*\Delta D + h(Tw - Tb)*\Delta x*\Delta y + \varepsilon\sigma(Tw^4 - T^4_0)$$

The term on the left side of the above equation represents the energy supplied to the element through joule heating. The right side contains the amount of energy released by the element by conduction, convection and radiation. The conduction term is the summation of the conduction of that element to the four elements surrounding the cell of interest. ΔS and ΔD can be either Δx or Δy depending on the direction of the conduction. In general, the radial conduction and the radiation are negligible and are not included in the calculation of the heat transfer coefficient h.

$$h = [\,(I^2R_f/A_f)*\Delta x*\Delta y + \Sigma\, k\,(\Delta\Gamma/\Delta x)*\Delta t*\Delta y)]\ /\ [(Tw - Tb)*\Delta x*\Delta y]$$

It should be noted that in the actual calculation of the heat transfer coefficient the lateral conduction is taken to travel from the leading surface to the trailing surface. In the rotating experiments the leading surface is hotter than the trailing surface and the side surfaces provide the continuation from the leading to trailing surface. The temperature profile on the side surface is linear, decreasing from the leading surface temperature to

the trailing surface temperature. The lateral conduction is based on the slope of the temperature profile on the side surfaces, and is uniformly subtracted from the leading surface and added to the trailing surface.

Typical values involved in the calculation of the heat transfer coefficient are listed in the table along with their description.

Table 2.1 Typical Experimental Values

Variable	Typical Value	Description
I	≅ 100 amps	current passing through the test section
Rf	≅ 0.015 Ω	resistance of the test section
A_f	≅ 3.99e-3 m	test section surface area
Δy	= 6.35e-3 m	radial spacing between points
Δx	= 5.0e-4 m	circumferential spacing between points
Δt	= 0.254e-3 m	test section thickness
k	= 15 W/mK	thermal conductivity of the model
Tb	≅ 340 °K	coolant bulk temperature
Tw	≅ 500 °K	wall temperature
dT/dy	≅ 2669 °K/m	temperature gradient across a side surface

Tw is the wall temperature obtained using the infrared detector, and Tb is the coolant bulk temperature for the radial height of interest. The radial bulk temperature includes the temperature increase that occurs due to the heat addition to the flow as the flow travels through the passage.

The rest of this chapter describes the experimental system in more detail. The description is broken into three major categories. Section 2.2 describes how the model is heated and rotated. Section 2.3 discusses the method used to control and measure the thermodynamic properties of the cooling gas. Section 2.4 reviews the method used to obtain the non obtrusive model surface temperature measurements. Most of the experiment is enclosed and operated under a vacuum which enables the model to rotate at high speeds, limits the loss in the infrared measurements and limits external convective loss from the model. Figure 2.3 displays the major features of the enclosed vacuum system and is referred to in the following sections.

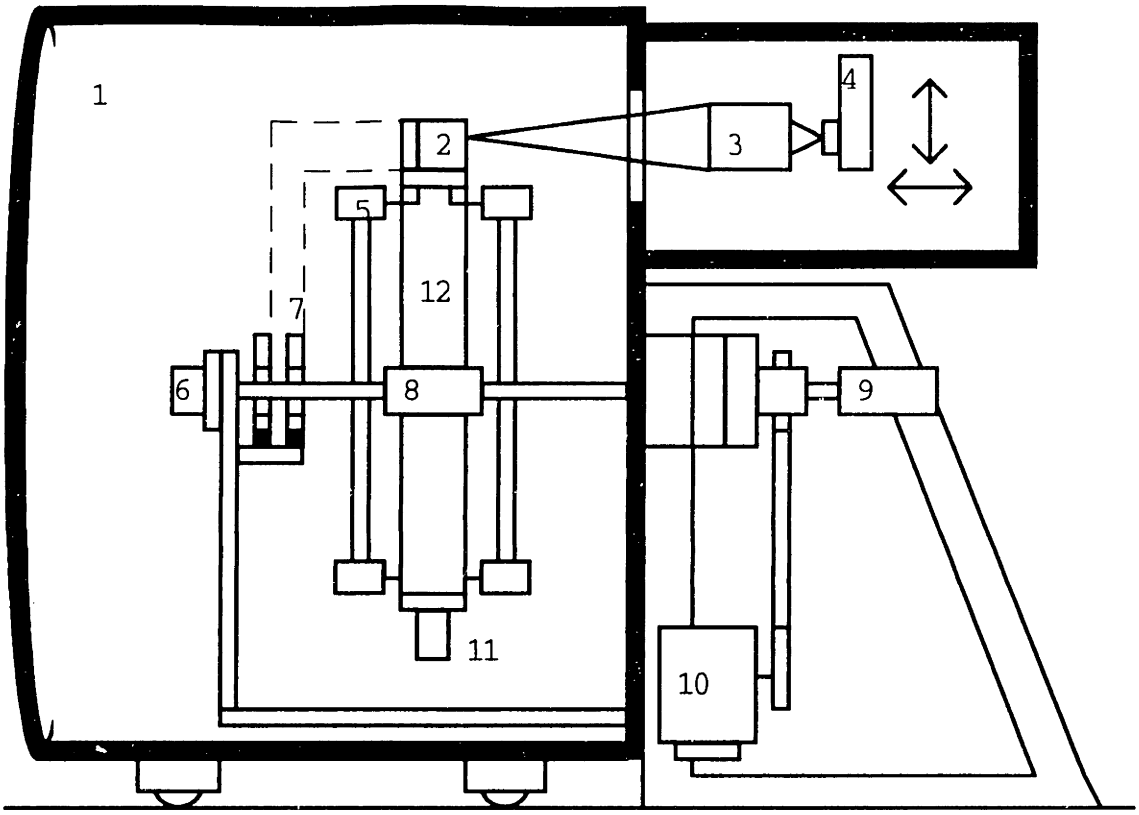

1. Vacuum Chamber
2. Model and Flat Mirrors
3. Imaging System (Primary and Secondary Mirror)
4. Infrared Detector
5. Heat Exchangers
6. Optical Encoder
7. Power Slip Rings
8. Gun Bored Shaft
9. Instrument Slip Ring
10. Variable Speed Motor
11. Counter Balance
12. Rotor

Figure 2.3 Overall Schematic Drawing of the Experimental Apparatus (not to scale)

2.2 Model Heat Generation and Rotation

Experimental results are presented for three different models; a smooth square model, a smooth rectangular model and a ribbed rectangular model. Each test section is four inches long, and is mounted on a shaft that has a 32 inch diameter (12 of figure 2.3). Individual model dimensions are listed below.

Table 2.2 Model Dimensions

Test Section	Rectangular Smooth	Rectangular Ribbed	Square Smooth
Outer Length	0.635 in.	0.635 in.	0.295 in.
Outer Width	0.193 in.	0.193 in.	0.295 in.
Height	4.0 in.	4.0 in.	4.0 in.
Thickness	0.019 in.	0.01 in.	0.01 in.
Resistance (installed)	0.0064 Ω	0.014 Ω	0.0178 Ω
Hydraulic Diameter	0.295	0.295	0.295

For the ribbed model the ribs are at a 45 degree angle, with a height e of 0.030 in. and a spacing of L = 10e. Figure 2.4 shows a schematic of the ribs which are on the leading and trailing surface of the ribbed rectangular model. The ribs are designed to enhance turbulent mixing which in turn enhances the heat transfer on the leading and trailing surfaces.

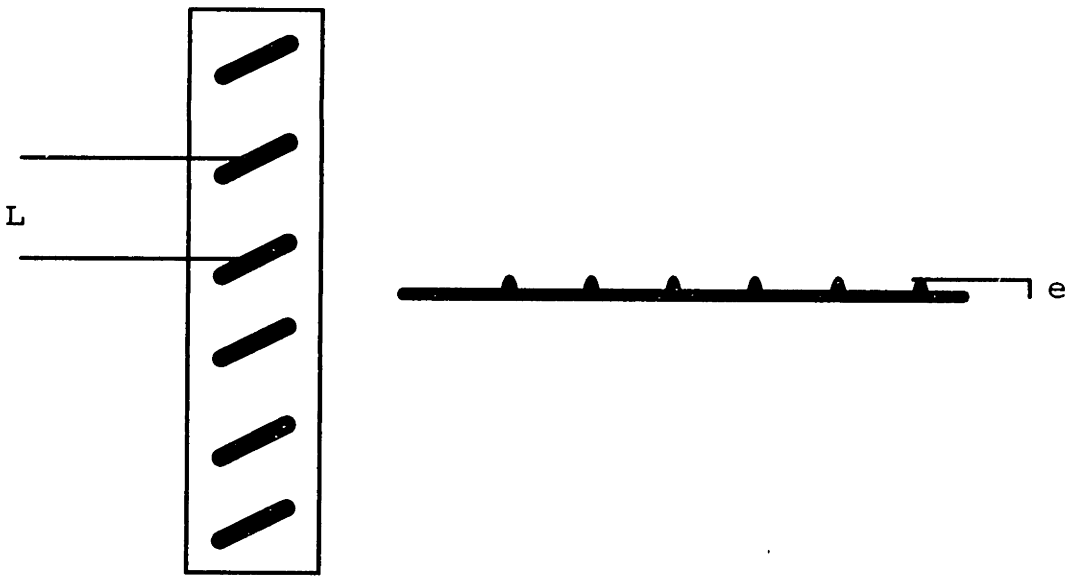

Figure 2.4 Front and Side View of the Turbulence Promoting Ribs

Each model is made of Nichrome 80-20 which has a thermal conductivity of 20 W/mK and an approximate resistivity of 1.4×10^{-4} Ω-cm. Nichrome is an ideal material since it's resistivity and thermal conductivity are nearly independent of temperature. The

manufacturing of each test section is performed by H & B Tool and Engineering Company for General Electric.

The model is heated through resistive heating, in which the model acts as a uniform resistor that heats up as current is passed through it. The current is brought into the vacuum chamber through copper strips and transferred from the stationary to rotating frame of reference through the use of carbon brushes in a power slip ring (7 of figure 2.3).

The model, along with the flat mirrors behind the model, (2 of figure 2.3) is attached to one end of a thirty two inch diameter rotor. A counter balance (11 of figure 2.3) is attached to the other end of the rotor. The speed of the shaft is regulated by a 7.5 HP variable speed motor (10 of figure 2.3) that is connected to the rotor by the use of pulleys. Although the motor is able to turn the shaft a maximum speed of 30 rev/sec, the arm is balanced to rotate at a maximum speed of 27 rev/sec with resonance between 19-24 rev/sec.

The speed of the rotating arm is measured by using the pulses emitted by the BEI optical encoder that is attached to the shaft (6 of figure 2.3). The optical encoder, powered by a 5 volt source, provides three (3) channels of information. Channel A gives 500 pulses per revolution, Channel B gives 500 pulses per revolution which are 90 degrees out of phase of Channel A, and an Index pulse is emitted once per revolution. The rotor speed is monitored using a Universal Counter which displays the frequency of the index pulse. A more accurate determination of the rotation speed is obtained through the use of a computer routine that counts the number of Channel A pulses collected during a certain time frame.

2.3 Cooling Flow System

Freon 12 is currently used as the cooling gas. Although Freon 12 has properties that are desirable for the experiment it is detrimental to the environment. As a result, Freon will be phased out and will be replaced with 134-A.

An oil free compressor circulates the gas through the rig as shown in figure 2.5. A series of valves and a supply tank are used to set the pressure and mass flow of the

Freon. Ideally, the gas flows in a closed loop, traveling out of the compressor, through the model, and then back into the compressor. Measurements of the flow rate, flow temperature and flow pressure are made at the exit of the compressor. The flow pressure upon entering the compressor is also measured and gives the pressure drop through the entire system. Thermocouples located at the inlet and outlet of the model are used to measure the coolant bulk temperature. Two thermocouples are located at each location for redundancy. Further, pressure taps, which are located at the inlet and outlet of the model, are available but are not currently utilized and are not pictured in figure 2.5.

An added complexity to the flow system is introduced due to the requirement of a low gas temperature entering and exiting the vacuum through rotating seals. High temperature flow would cause the vacuum seals to burn. Yet as cooling flow cools the model, the bulk flow temperature increases to potentially dangerous levels. As a result, counter flow heat exchangers are placed on the rotating shaft. The heat exchangers transfer the heat from the high temperature flow, which is exiting the model, to the low temperature flow that will be entering the model. In this way low temperature flow (around $77^{o}F$) is passed through the seals while higher temperature flow (around $300^{o}F$) is passed through the model.

As pictured in figure 2.5, the inlet to the model is an inlet plenum. The velocity profile at the entrance to the model is not known but is assumed to be similar to the conditions of actual turbine blade cooling passages.

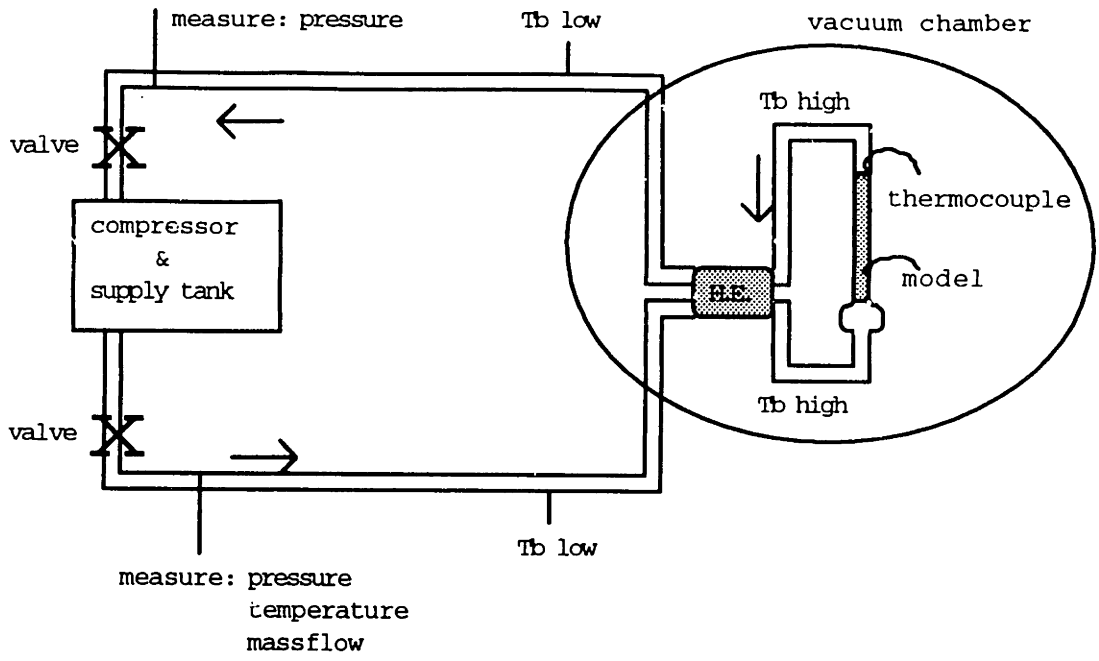

Figure 2.5 Schematic of the cooling gas flow system

2.4 Surface Temperature Measurements

Surface temperatures are measured using an infrared detector and an imaging system (3 and 4 of figure 2.3). A side view of the system is also pictured in figure 2.1. The primary imaging system collects a cone of radiation that is emitted from a point on the surface, and focuses the radiation onto the detector element. The infrared detector output voltage varies depending on the amount of radiation focused onto the detector element. Since the amount of radiation that is emitted from a point is dependent on the temperature of that point, variation in the IR signal corresponds to variations in the surface temperature. The surface of each model is coated with high temperature flat black paint, to minimize the variations in emissivity.

The imaging system and infrared detector are mounted on a platform that can travel horizontally and vertically. The horizontal motion allows the system to focus onto a point on the surface and the vertical motion allows the system to scan certain radial locations on the model. Each time the model rotates by the imaging system, the infrared detector scans across the width of the model. The infrared detector is fast enough to

detect any variation in surface temperatures even when the model is rotating at high speeds.

Flat mirrors are placed behind the model, in order to collect the radiation from the leading, trailing and back surfaces. The mirrors are at a 45 degree angle with respect to the model. Pictured in figure 2.2 is the way the cone of radiation gets reflected off the leading surface. In a similar manner, the trailing surface cone of radiation gets reflected once off the opposite mirror. The cone of radiation for the back surface gets reflected twice, once off of each mirror. The imaging system is moved horizontally in order to keep the distance that the radiation travels from a point on the surface to the IR detector constant.

With the imaging system, the rotation of the model, and the two directional platform, radiation can be collected from each point on the model. The process of collecting the IR signal from each point on the model is called a 'scan' and is controlled by a computer program. A calibration process is used to convert the IR signal voltage into temperature. The calibration process is described in more detail in the appendix but essentially involves a series of *Calibration Runs* in which the IR signal is recorded for each point on the model and is matched with a presumed temperature. Five such temperature voltage pairs are obtained for each location and are used to generate a 'local' function of temperature based on voltage. The voltage obtained during a *Test Run* is converted into temperature by using this 'local' function. By performing a 'local' calibration, location dependent geometric effects and mirror losses that occur as the radiation travels from the model to the detector are factored out. In addition, even though each model is coated to promote uniform emissivity, any variations of surface emissivity are also factored out.

Chapter 3
Discussion of Experimental Phenomena

3.1 Introduction

Experimental results are presented in the subsequent chapters. Each model is discussed in turn as the density ratio, the rotation number, the Reynolds number and the buoyancy parameter are varied. This chapter, discusses each of the above parameters of interest as well as the basics of the internal coolant flow structure. Since internal flow characteristics and surface heat transfer distribution are coupled, examination of the experimental results provides additional information on the internal flow structure.

3.2 Internal Flow Discussion

This paragraph applies knowledge of flow characteristics in stationary ducts to describe the cooling flow in the present experiment. First of all, the cooling flow is turbulent as it passes through the channel. Transition from laminar to turbulent flow in stationary ducts occurs for Reynolds number about 2300 which is at least an order of magnitude smaller then the experimental operating Reynolds number. Further, the flow through most, if not all, of the channel is not fully developed since at the exit of the model $x/d_h = 14$ and the entry length for fully developed hydrodynamic and thermal boundary layers for stationary ducts is at $x/d_h > 10$. However, as the thermal boundary layers grows, the convective heat transfer coefficient decreases since the temperature gradient in the boundary layer decreases. The convective heat transfer is driven, in part, by the slope of the thermal boundary layer. In addition, in turbulent flows, the heat transfer takes place through molecular diffusion as well as through turbulent mixing [6].

When the model is heated and rotated the structure of the cooling flow becomes quite complicated. The equations of motions below [10] are the result of applying Newton's Second Law of Motion to the flow in the channel, in the coordinate system that is rotating with the channel and is pictured in figure 3.1.

Continuity: $\text{div}(\rho \mathbf{u}) = 0$

x-Momentum $\text{div}(\rho u u) = -\partial p/\partial x - 2\rho\Omega w + \rho\Omega^2 x + \text{div}[(\mu + \mu_t)\text{grad}(u)]$

y-Momentum $\text{div}(\rho \mathbf{u} v) = -\partial p/\partial y + \text{div}[(\mu + \mu_t)\text{grad}(v)]$

z-Momentum $\text{div}(\rho \mathbf{u} w) = -\partial p/\partial z + 2\rho\Omega u + \rho\Omega^2 z + \text{div}[(\mu + \mu_t)\text{grad}(w)]$

Enthalpy $\text{div}(\rho \mathbf{u} h) = \text{div}[(\mu/Pr + \mu_t/Pr_t)\text{grad}(h)]$

where:

x,y,x = coordinates as defined in figure 3.1

u,v,w = flow velocity in the x,y,z directions

μ, μ_t = laminar and turbulent viscosity, respectively

Pr, Pr_t = laminar and turbulent Prandtl number, respectively

p = pressure

h = enthalpy

Ω = angular rate of rotation

In the x and z momentum equations, the second term is the effect of the Coriolis force and the third term is a result of centrifugal forces. The Coriolis force induces a secondary cross stream flow which is also pictured in figure 3.1. Flow is carried from the leading surface, through the center of the channel, to the trailing surface. The flow then travels back to the leading surface along the side walls. This action can be seen in the second term of the x momentum equation where the Coriolis force acts in the negative x direction and is proportional to the flow velocity. At the inlet of the test section the peak velocity will occur in the center of the channel, but as the flow travels up the channel, the Coriolis force continues to push the higher momentum flow towards the trailing surface, and the peak velocity shifts towards the trailing surface. The lower temperature, higher momentum flow significantly cools the trailing surface. The flow then continues to increase in temperature as it travels by the side walls and gains the heat from the side walls. By the time the flow returns to the leading surface the flow temperature is higher and the leading surface is cooled less. This is part of the reason why the trailing surface heat transfer coefficient is much greater than the leading surface heat transfer coefficient for large rotation numbers. Another important characteristic is the thickness of the boundary layer on the leading and trailing surface. The combination of Coriolis cross stream flows and buoyancy effects tend to cause the boundary layer on the trailing surface to be thinner than the leading surface. The thinner boundary layer increases the potential for heat transfer. Further, the centrifugal force has a stronger

effect on the lower temperature (heavier) flow that is near the trailing surface then it has on the warmer (lighter) flow located near the leading surface. Due to this imbalance of force the velocity near the trailing surface increases and the velocity near the leading surface decreases. If the imbalance of forces is strong enough, flow reversal could occur [10].

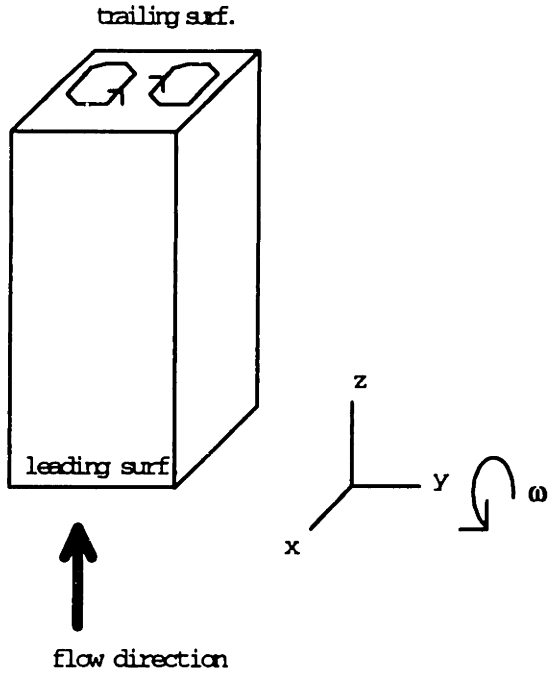

Figure 3.1 Schematic of the model, bulk flow direction, and direction of rotation

The way in which the flow cools the model is a function of a number of variables. The variables are combined into non dimensional parameters that serve to show the strength of certain flow physics. The parameters and their description are listed in Table 3.1.

Table 3.1 Non Dimensional Parameter Definition and Description

Parameter	Definition	Description
Density Ratio ($\Delta\rho/\rho$)	(Tw - Tb)/Tw	indicates the strength of the centrifugal buoyancy force
Rotation Number (Ro)	$\omega d_h/v$	relates the strength of the Coriolis force to the inertia force and governs the formation of the secondary cross stream flow (v = bulk flow velocity)
Reynolds Number (Re)	$\rho v d_h/\mu$	compares the inertia force to viscous forces and is an indication of the forced convection
Buoyancy Parameter (B)	$\Delta\rho/\rho * Ro^2 * R/d_h$	combines the effect of the centrifugal buoyancy force, the Coriolis force and geometric effects

3.3 Wall Condition Effects on Convection

Convection is driven by the difference between the wall temperature and the near surface coolant temperature. However, it is conventional to define the film coefficient in terms of the difference between the wall temperature and the bulk coolant temperature. The wall and bulk temperature difference changes as the flow travels out the model and these downstream variations in temperature difference are greatly dependent on the wall conditions. For example, looking at a power balance of an element in a stationary tube, figure 3.2,

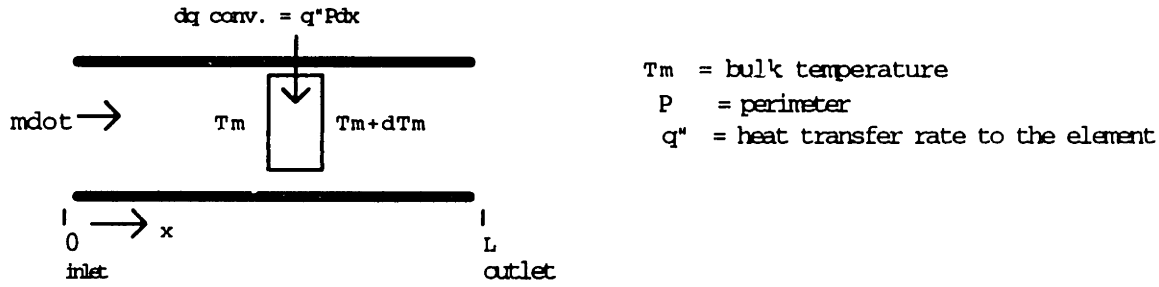

Figure 3.2 Power balance of an element in a stationary tube

then the temperature dependence on distance dT_m/dx is described by the relationship below, which is valid regardless of the wall conditions.

$dT_m/dx = (P)/(mdot*c_p)*h(T_s - T_m)$

where:

P = perimeter

h = heat transfer coefficient

T_s= surface temperature

T_m = mean bulk temperature

mdot = mass flow rate

c_p = specific heat at constant pressure

If the surface of the wall is held at a constant flux, as in the present experiments, then the mean bulk flow temperature varies with increased distance down the channel as $T_m(x) = T_{mi} + (q_s"*P)/(mdot*c_p) *x$ where T_{mi} is the inlet bulk temperature. This equation is linear in x. However, if the wall is held at a constant temperature then the mean bulk temperature varies as $T_m(x) = T_s - (T_s - T_{mi})*exp[(-Pxh)/(mdot*c_p)]$ which is exponential in x. The diagrams in figure 3.3 depict the distinct temperature differences that drive the convective heat transfer.

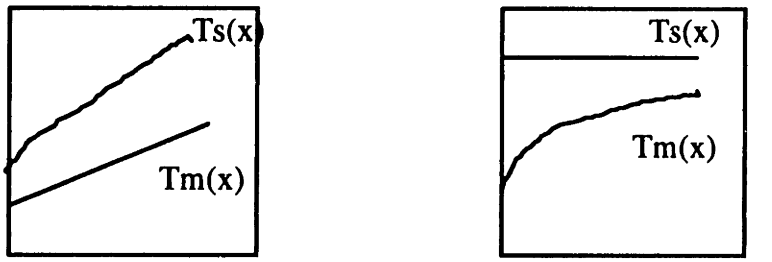

Figure 3.3 Example of the temperature difference that drives convection in a stationary tube.

In addition, the constant heat flux and constant wall temperatures cause a different temperature distribution across the tube, as shown in figure 3.4. Also indicated in figure 3.4 is the enhancement of the heat transfer for the uniform heat flux experiment as

compared to the uniform wall temperature experiment. Han et. al. [4] found that the heat transfer in the uniform heat flux experiment was enhanced by 40-80% on the leading surface and 10-20% on the trailing surface when compared to the uniform temperature experiment.

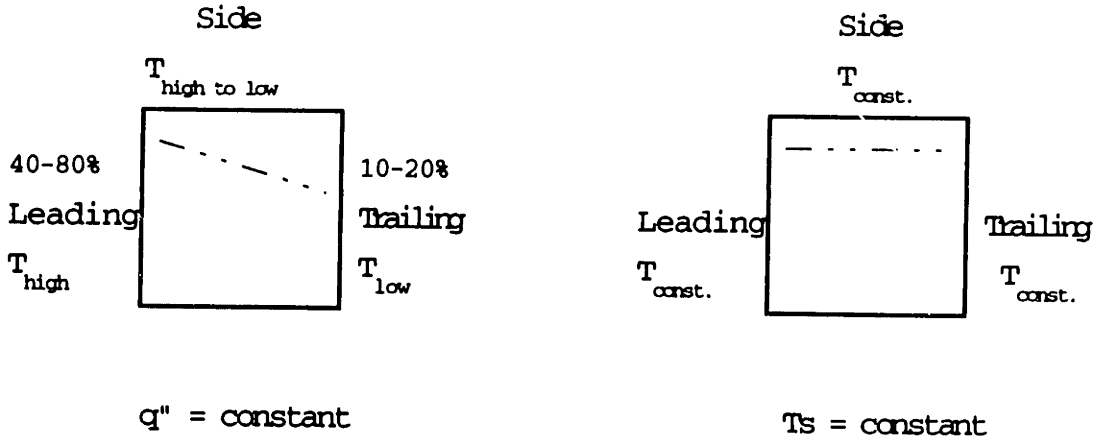

Figure 3.4 Temperature distribution across the tube

In the constant heat flux experiment the trailing surface will get cooled more than the leading surface and as a result the trailing surface temperature will be lower than the leading surface temperature. The difference between the leading and trailing surface temperatures increases the imbalance in buoyancy force across the test section. Further, the Coriolis force circulates the flow from the center of the channel, to the trailing surface, along the side walls and back to the leading surface. Since the trailing wall is at a lower temperature then the leading surface, and the maximum temperature of the fluid near the trailing wall is the trailing wall temperature, when this fluid is carried to the leading surface the difference between the wall and flow temperature is larger than it would be in the uniform wall temperature scenario and the heat transfer is greatly enhanced. The temperature of the flow near the leading surface increases and the outward buoyancy force is less, which in turn, enables the Coriolis force to circulate the flow more effectively.

Finally, the results are in terms of the local Nusselt Number ratio Nu/Nu_{∞}, where Nu, is the local Nusselt number, and Nu_{∞} is the Nusselt number based on the Dittus-Boelter correlation $Nu_{\infty} = 0.023*Re^{.8} * Pr^{.4}$ which is valid for $0.7 \leq Pr \leq 160$, $10{,}000 \leq Re$, and $10 \leq x/d_h$.

Chapter 4
Experimental Results and Discussion

4.1 Introduction

In this chapter, the results from a series of GTL test runs are presented. Section 4.2 validates the experimental technique by showing that the GTL data is in agreement with the results of Han et.al.[4], Guidez [1] and Wagner et. al. [3],[11]-[12] where they overlap. Comparisons were focused on these three authors since other researchers were not able to obtain significant rotation numbers at Reynolds numbers of 25,000 -50,000. Section 4.3 shows the variation in heat transfer as the rotation number, Reynolds number and density ratio are changed. Sections 4.4 and 4.5 show the effect of buoyancy parameter on the heat transfer for the smooth and ribbed rectangular model, respectively. The final section combines the results from each model and shows how the shape of the heat transfer distribution is dependent on the geometrical characteristics of the model. Table 4.1. lists the test numbers and the associated non-dimensional parameters of the data that is presented throughout this Chapter. The buoyancy parameter, rotation number, Reynolds number, and density ratio, are calculated based on the bulk and/or wall temperature averaged over the length of the tube. The transport properties, μ and k, used in calculating the local Nu and Nu_∞ are based on the local bulk flow temperature.

Table 4.1

Test	Buoyancy Parameter	Rotation Number	Density Ratio	Reynolds Number
Smooth Square: Calibration File: calss.mat				
m42	0.14	0.08	0.36	32,000
m43	5.59	0.64	0.22	25,000
m44	2.76	0.41	0.27	25,000
m45	1.40	0.28	0.30	25,000
m46	0.39	0.14	0.32	26,000
m47	0.88	0.25	0.23	28,000
m48	0.24	0.11	0.31	51,000
m49	0.24	0.11	0.31	53,000
m50	1.52	0.30	0.27	49,000
m51	0.52	0.18	0.28	51,000
m52	0.04	0.04	0.29	114,000
m53	0.21	0.12	0.25	107,000
m54	0.07	0.07	0.25	104,000
Smooth Rectangular: Calibration File: calsr.mat				
m23	0.03	0.05	0.24	68,000
m24	0.18	0.10	0.30	28,000
m25	1.81	0.32	0.29	25,000
m26	3.77	0.49	0.25	25,000
Ribbed Rectangular: Calibration File: calrr.mat				
m33	0.27	0.12	0.30	26,000
m34	0.72	0.21	0.26	24,000
m35	1.38	0.30	0.25	26,000
m36	3.63	0.53	0.21	26,000

4.2 Validation

Data from the smooth square and smooth rectangular model are used to compare GTL results with the findings reported by Han, Guidez, and Wagner. GTL data agrees with the results reported by these researchers when corrected for differences due to holding the wall temperature constant rather than heat flux.

4.2.1 Comparison with Han

Figure 4.1 below overlays the GTL data and the Han published data [4]. Han performed tests by simulating the heat transfer as a constant heat flux, constant wall temperature and uneven wall temperature condition. The data presented in the overlay is from the constant heat flux results. Figure 4.1 is a plot of Nu/Nu_{∞} versus X/Dh increasing radially along the model. The dashed line corresponds to the GTL data and the solid line to the Han data. The 'x's indicate the trailing surface and the 'o's identify the leading surface. The GTL data is actually an average across the width of the surface at each X/Dh.

The GTL data is at a rotation number, density ratio and Reynolds number, of 0.08, 0.36 and 32,000 respectively. The Han data is at a condition of rotation number, density ratio and Reynolds number of 0.0352, 0.10 and 25,000 respectively. The variation in Reynolds number is not significant. The large difference in density ratio is also believed to have little effect on the heat transfer at the low rotation rates of interest. The variation in rotation number is minor.

Figure 4.1: Overlay of GTL Data and Han Data

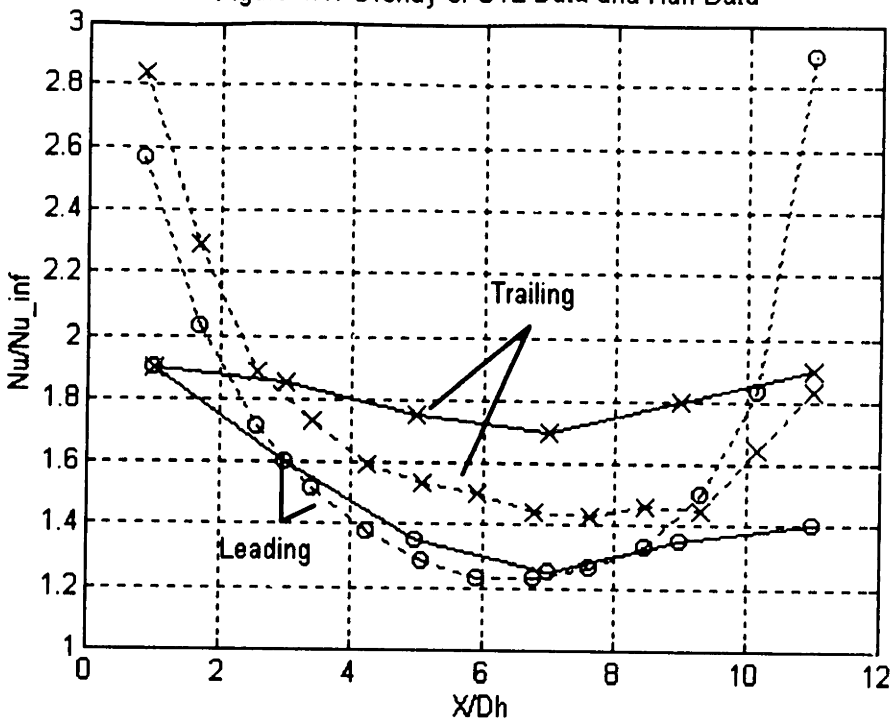

Key for Figure 4.1:

Line	Origin	Re	Ro	Δρ/ρ
Solid	Han	25,000	0.0352	0.10
Dashed	GTL (m42)	32,000	0.08	0.36

In the range of X/Dh of 3 up to 10, the GTL data demonstrates the same trend and magnitude as the Han data, with the exception of the trailing surface. In this case, the GTL data is around 1.42 and the Han data is about 1.75 at X/Dh of 7. The two values are within 20% of each other and when taking into consideration the experimental accuracy of each experiment this difference is believed to be acceptable. The disagreement between the GTL and the Han data below X/Dh of 3 is attributed to the significantly different inlet conditions of the two experiments. The inlet of the GTL model is simply an inlet plenum, whereas Han ensures fully developed flow at the entrance of the channel. Similarly, the differences at X/Dh greater than 10 can be attributed to outlet effects as the cross sectional pressure must match as the flow exits the channel and is turned.

4.2.2 Comparison with Guidez

Figure 4.2 compares the GTL data with the data published by Guidez [1]. Guidez simulated the external heat transfer to the model with a uniform heat flux and performed experiments with a rectangular model with an aspect ratio of 2.0. The plot shows Nu/Nu_∞ versus rotation number for X/Dh of 7.4. The square model GTL data is represented by the dashed lines, the smooth rectangular model GTL data by the dash-dotted lines and the data from Guidez is represented by the solid lines. Again, 'o' is used for the leading surface and 'x' for the trailing surface. Since the data is presented in terms of Nu/Nu_∞ it is acceptable to compare the three cases although they are at different Reynolds numbers. By normalizing the data to the stationary case, some Reynolds number effects are removed. Again, the GTL data is an average over the width of each surface corresponding to an X/Dh of about 7.4.

Figure 4.2: Comparison of GTL Data with Guidez Results

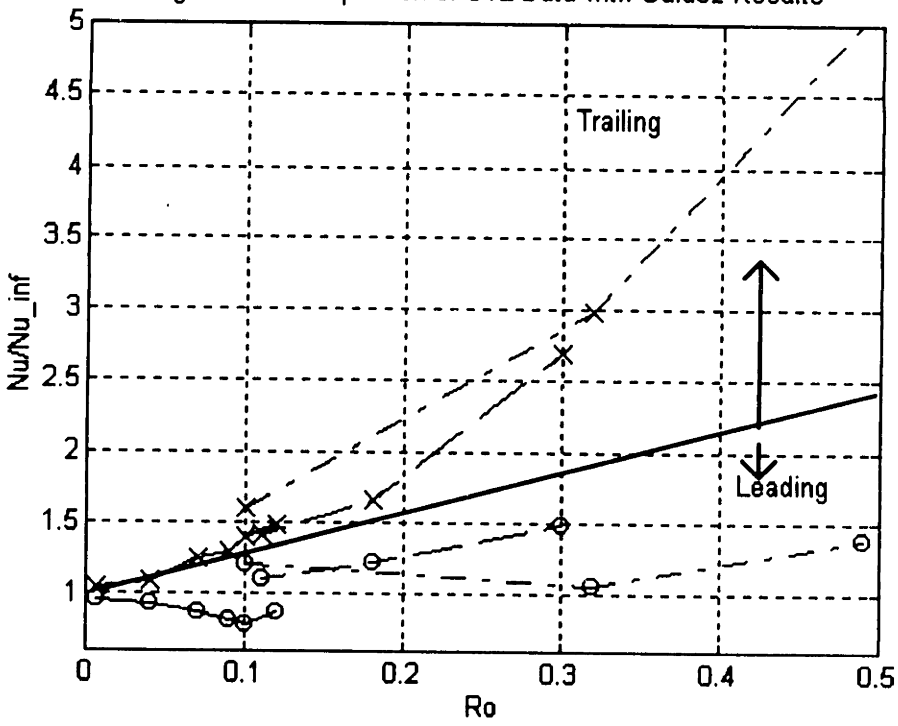

Key for Figure 4.2:

Line	Origin	Re	Aspect Ratio	Δρ/ρ	X/Dh
Solid	Guidez	41,000	2.0	not avail.	7.4
Dashed	GTL(m48-51)	≈50,000	1	≈0.29	7.4
Dash Dot	GTL(m24-26)	≈25,000	3.3	≈0.27	7.4

The GTL data for the square and the smooth rectangular plot show similar trends and magnitude as the Guidez results. Although the GTL data agrees with the Guidez results, care must be taken to avoid misinterpreting the results. From figure 4.2, it appears that at the location of X/Dh of 7.4 a definite trend can be seen as rotation is increased, and that the trend seems to be quite similar for each aspect ratio. Although this may be true for the particular location of X/Dh = 7.4, the actual heat transfer distribution on the ENTIRE surface of the model is shown to change considerably based on the geometry of the model. (see Section 4.6)

4.2.3 Comparison with Wagner

Figure 4.3 shows the excellent agreement between the heat transfer results of Wagner [2] and GTL. The plot displays Nu/Nu_{∞} versus X/Dh, with the solid line representing Wagner's data test number 102 [2], and the dashed line representing GTL's data. The trailing surface is indicated by the 'x's and the leading surface is identified by the 'o's. The two cases were at essentially identical Reynolds number, rotation number and density ratio.

In Wagner's experiments, a square channel was tested but the external heat transfer to the blade was simulated by imposing a uniform wall temperature on the channel. According to Han, the heat transfer obtained from a uniform heat flux experiment will be larger than the heat transfer found in a uniform wall temperature experiment. In fact, Han [4] determined that the trailing surface heat transfer will be 10-20% and the leading surface heat transfer will be 40-80% larger in the uniform heat flux experiment than in the uniform wall temperature experiment. Although, the trailing surface GTL points are the values that were obtained in the experiments, the leading surface points have been adjusted to account for the 40-80% difference between experiments. The actual leading surface GTL data was multiplied by 0.50 (i.e. 50%) and then plotted. With this approximate correction for the different methods of simulating the heat transfer to the model, GTL results match extremely well with the results published by Wagner. The trend and the magnitude of the GTL data match that of the Wagner data. Differences in the results for X/Dh below 3 and above 10 are attributed to different inlet and outlet conditions.

Figure 4.3: Overlay of GTL Data and Wagner Data

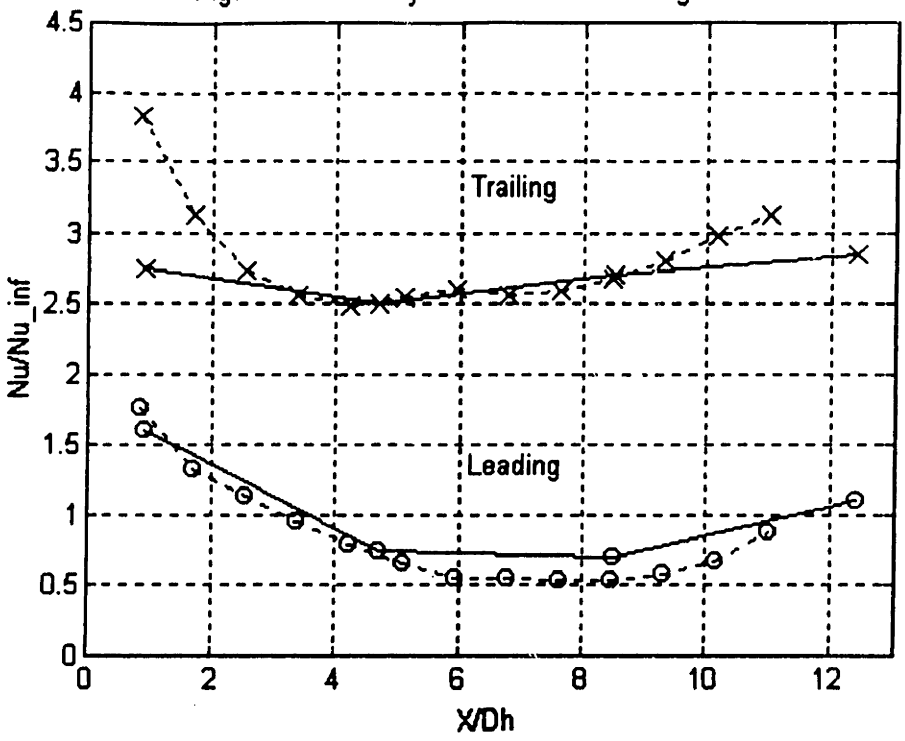

Key for Figure 4.3:

Line	Origin	Re	Ro	Δρ/ρ
Solid	Wagner(102)	25,000	0.24	0.22
Dashed	GTL (m47)	28,000	0.25	0.23

4.3 Smooth Square Model Results

The data for the square model demonstrates that as the buoyancy parameter is increased the magnitude of the Nusselt number ratio also increases. In addition, due to the way the flow enters the model, the heat transfer near the inlet is enhanced. As the Reynolds number is increased the heat transfer near the inlet of the trailing surface is further enhanced.

4.3.1 Effect of Rotation at Re ≈ 25,000 and Re ≈ 50,000

The following series of Nusselt number maps shows how the heat transfer distribution on the surface of the model changes as the buoyancy parameter is increased from 0.39 to 5.59. The maps picture the surface of the model unwrapped. From left to right, the images represent the leading, side-front, trailing, and side-back surfaces. The scale shows how the shading relates to the Nusselt number. These maps are useful in describing the shape of the heat transfer distribution. The magnitude of the heat transfer is more clearly displayed in the plots that will follow.

The model heat transfer map at each rotation number shows a distinctive cooling near the inlet and outlet of the test section. The inlet cooling region appears to increase as the rotation number increases, especially on the trailing surface. Due to the way the flow enters the model, it appears as if the flow is highly turbulent which is enhancing the inlet heat transfer. It is suspected that the flow may actually be impinging on the trailing surface and thus further enhancing the trailing surface inlet region heat transfer.

The maps also show the development of the Coriolis driven flow. The Coriolis force causes cross stream flows to develop in the channel. As the these cross stream flows develop, enhanced heat transfer on the trailing surface becomes apparent. For example, the increased cooling near the trailing surface outlet region of the B = 1.40 map is an indication of the development of the Coriolis generated cross stream vortices. With increased rotation, the region on the trailing surface that experiences enhanced heat transfer due to the development of the cross stream vortices is observed to extend closer to the inlet. This implies that with increased rotation, the Coriolis induced vortices develop faster.

The heat transfer maps also show that the side surfaces provide the continuity in heat transfer from the leading to trailing surfaces.

Heat Transfer Map M46

Re = 26,000, Ro = 0.14, $\Delta\rho/\rho$ = 0.32, B = 0.39

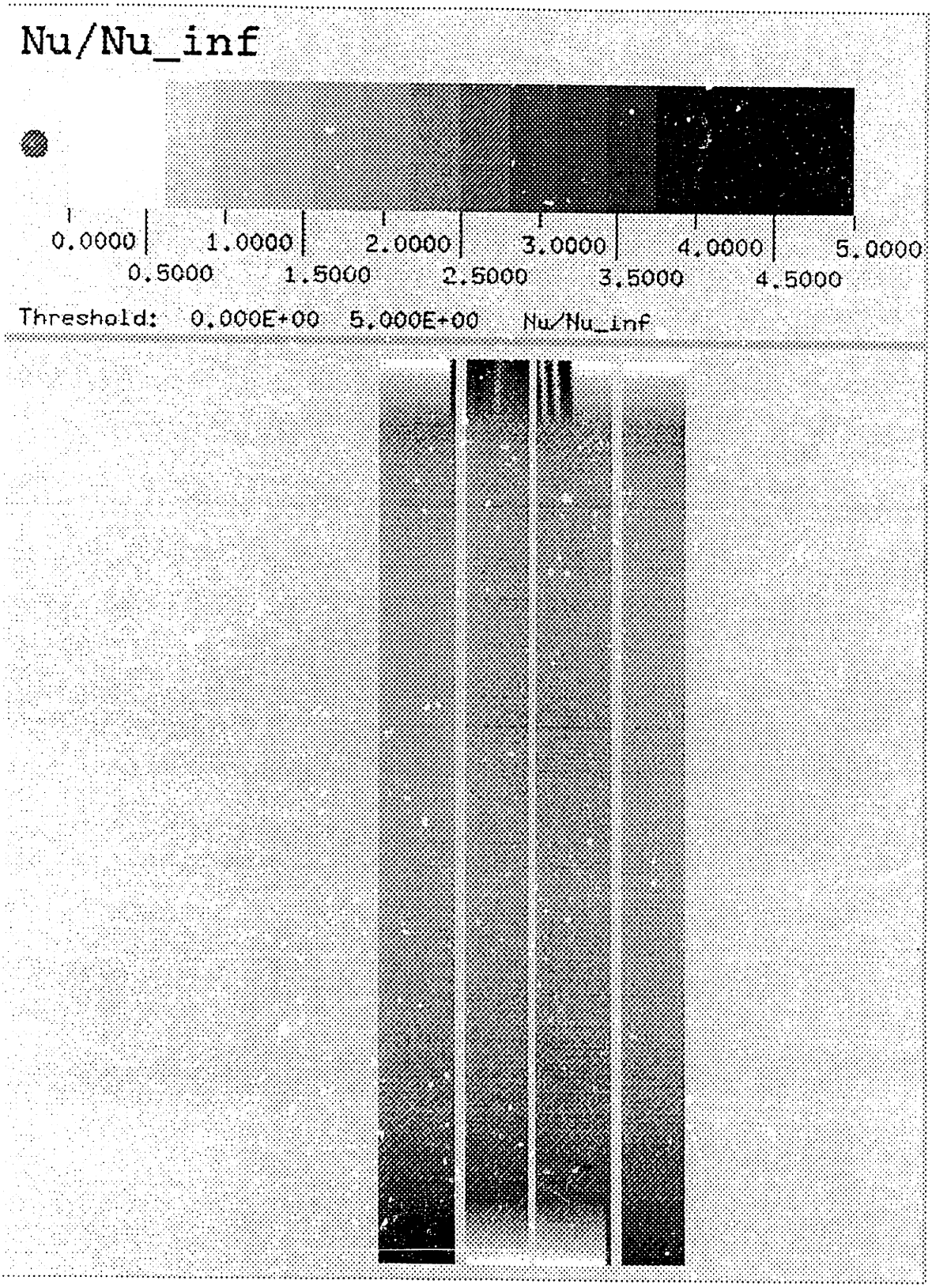

Heat Transfer Map M45

Re = 25,000, Ro = 0.28, $\Delta\rho/\rho$ = 0.30, B = 1.40

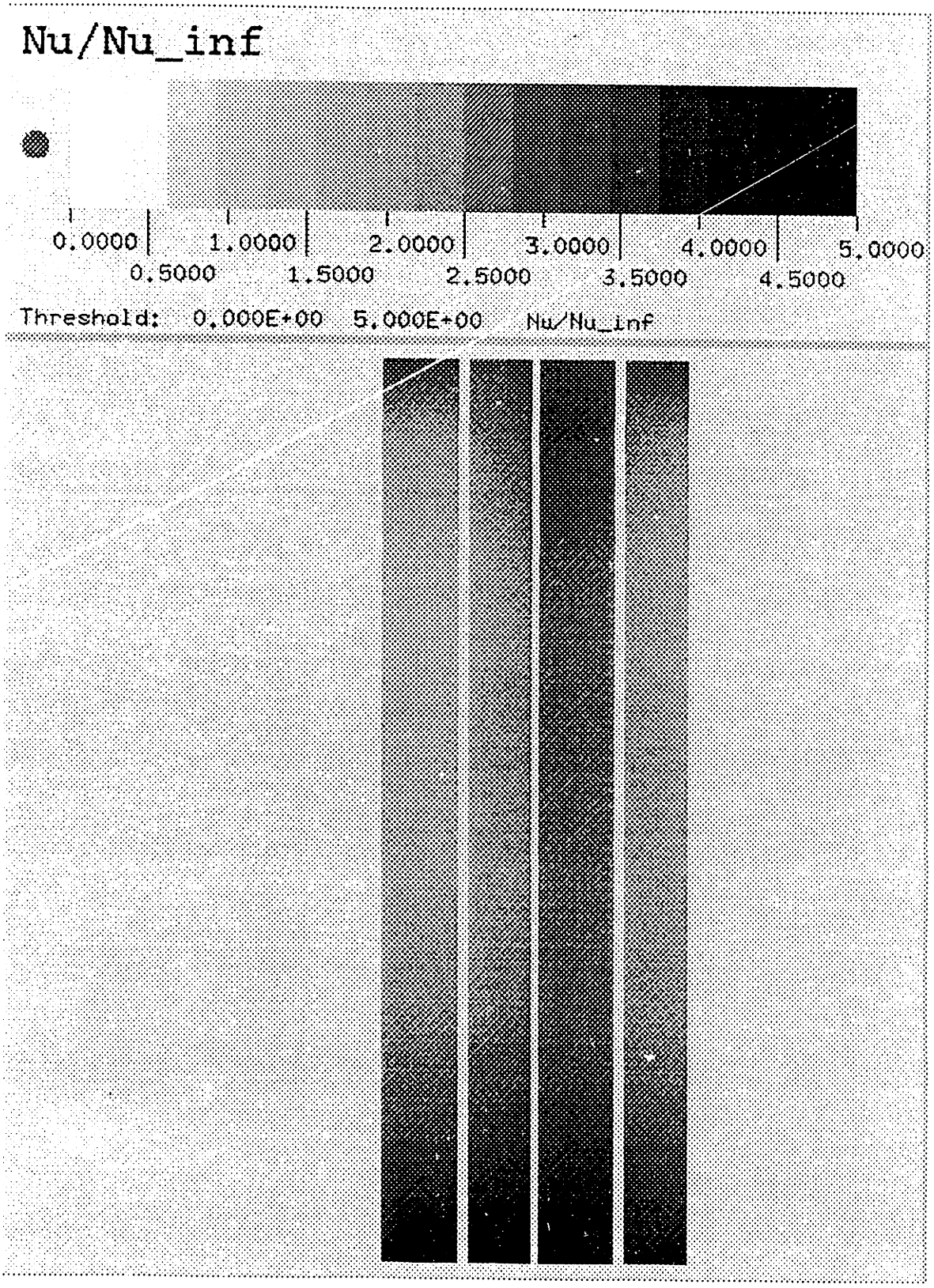

Heat Transfer Map M44

Re = 25,000, Ro = 0.41, $\Delta\rho/\rho$ = 0.27, B = 2.76

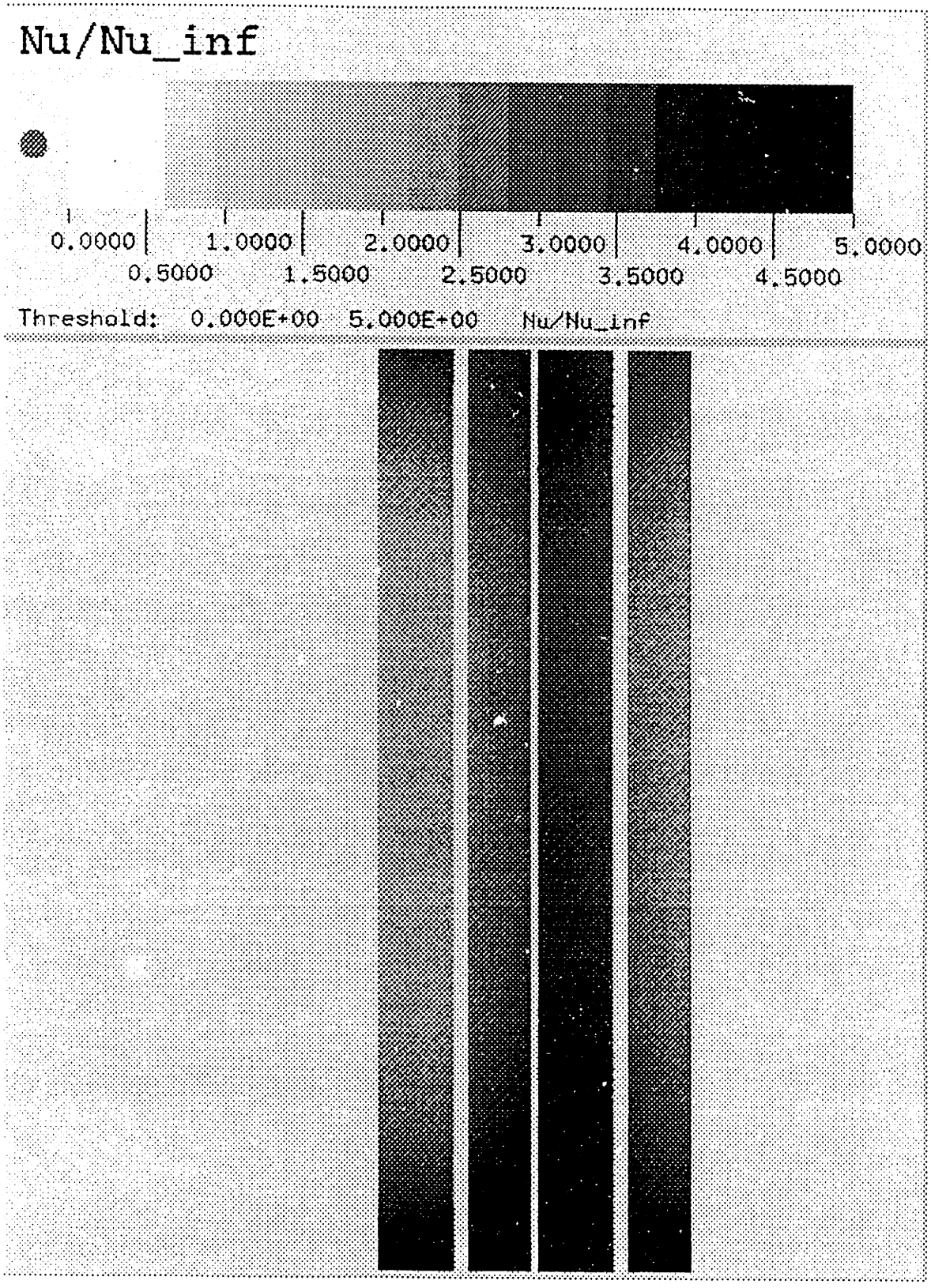

Heat Transfer Map M43

Re = 25,000, Ro = 0.64, $\Delta\rho/\rho$ = 0.22, B = 5.59

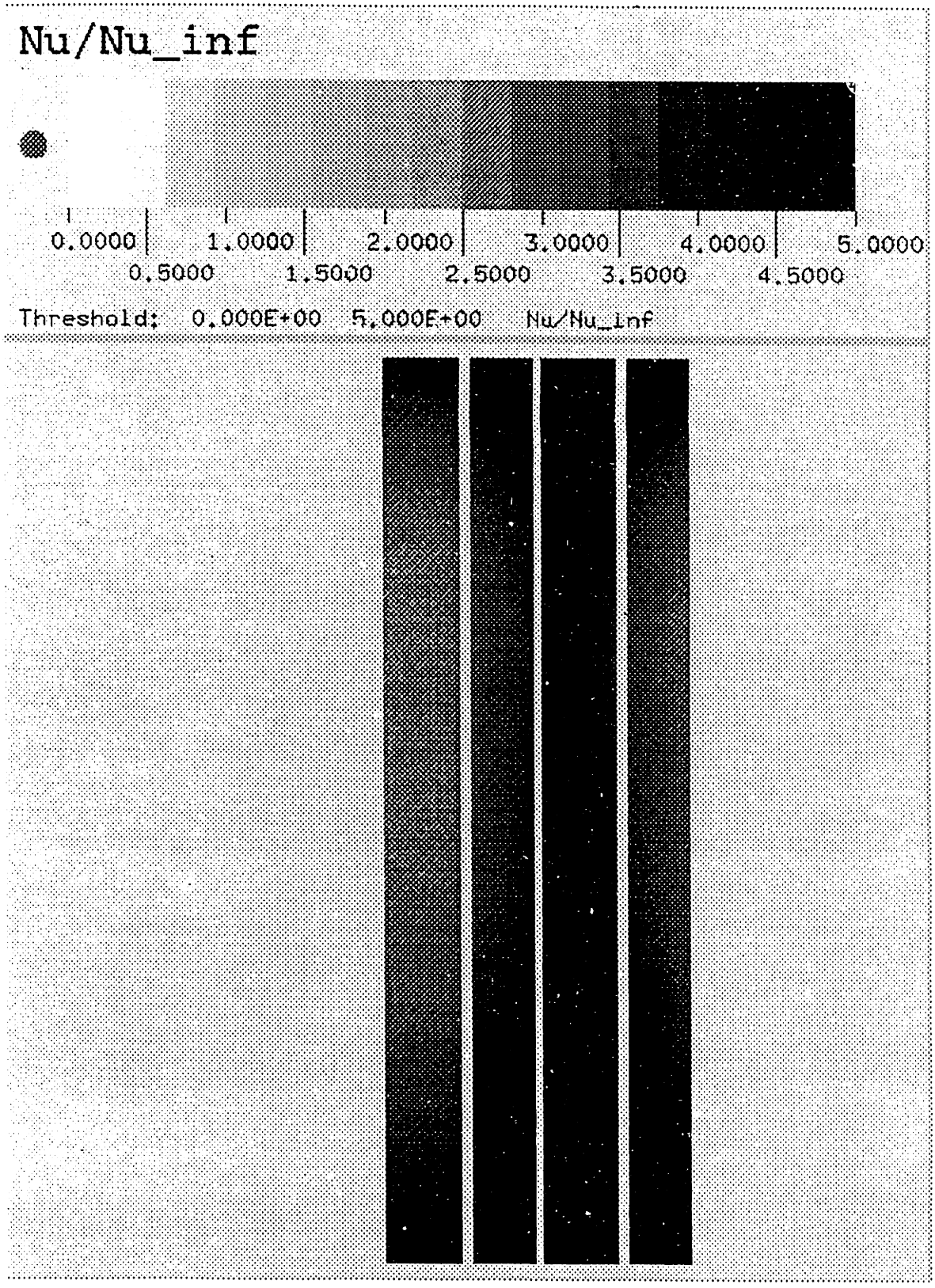

Figures 4.4a-c and 4.5a-c show the magnitude of the heat transfer dependence on rotation for a Reynolds number of 25,000 and 50,000 respectively. The arrows indicate the direction of increasing rotation number. Figures a and b display Nu/Nu_{∞} versus X/Dh along the model for the trailing and leading surface respectively. Figure c displays the ratio of the trailing to leading surface Nusselt number.

The data shows that as the buoyancy parameter is increased the heat transfer rate on both the leading and trailing surfaces increases. On the trailing surface, at an X/Dh of 8.5, the Nusselt number ratio increases from 1.9 to 3.9 as the buoyancy parameter is increased from 0.39 to 5.59. On the leading surface the Nusselt number ratio increases from 1.25 to 2.25 as the buoyancy parameter is increased from 0.39 to 5.59. These trends are consistent with results reported by Wagner. Wagner found that the heat transfer increased on the trailing surface with increased buoyancy parameter and in general, increased on the leading surface with increased buoyancy parameters for buoyancy parameters of 0.40 and larger. A more detailed comparison of Wagners results and the GTL data is not informative since the internal structure of the flow is different due to the methods used to simulate the external heat transfer to the channel. The temperature profile radially, and circumferentially depends on whether the heat transfer was modeled by a uniform temperature or a uniform heat flux. For the GTL data it seems that at the larger buoyancy parameters, the buoyancy forces assist the Coriolis force in thinning the boundary layer on the leading surface to increase the heat transfer.

From the trailing/leading plot, at the low buoyancy parameter of 0.39 the leading and trailing surfaces get cooled about the same amount except for the slight increase in cooling for the trailing surface near the outlet region. For the buoyancy parameter of 1.40, the trailing surface gets cooled more than the leading surface and this difference increases with distance along the model (i.e. the trailing/leading Nusselt number increases radially). This trend shows that for a buoyancy parameter of 0.39 and 1.40, the Coriolis force has a stronger effect on the trailing surface then on the leading surface in the outlet region. For the buoyancy parameters of 2.76 and 5.59, the trailing surface is cooled more than the leading surface but this difference decreases with distance along the model. This seems to imply that the Coriolis and buoyancy forces are enhancing the heat transfer on the leading and the trailing surfaces. Near the inlet, the large trailing/leading ratio is related to the large increase in heat transfer on the trailing surface due to the way the cooling flow enters the channel.

Figure 4.4a: Square Model Trailing Surface Rotational Effects at Re = 25,000

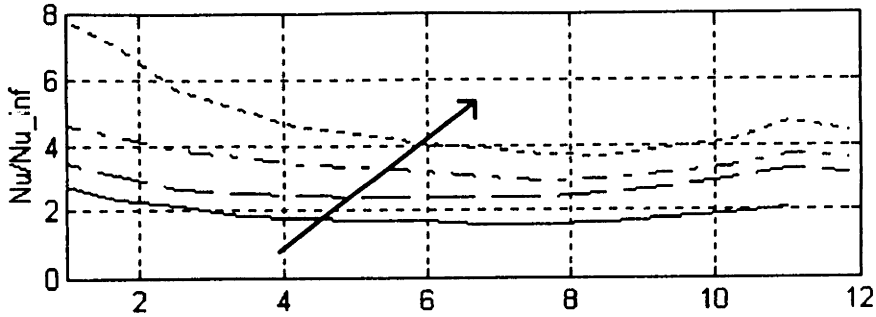

Figure 4.4b: Square Model Leading Surface Rotational Effects at Re = 25,000

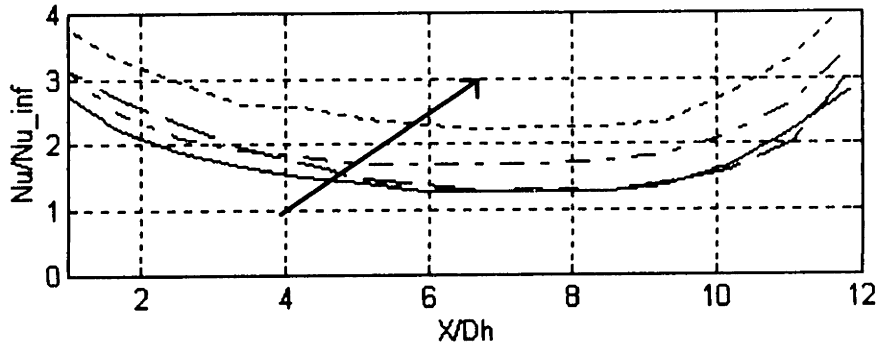

Figure 4.4c: Square Model Trailing/Leading Nu Rotational Effects at Re = 25,000

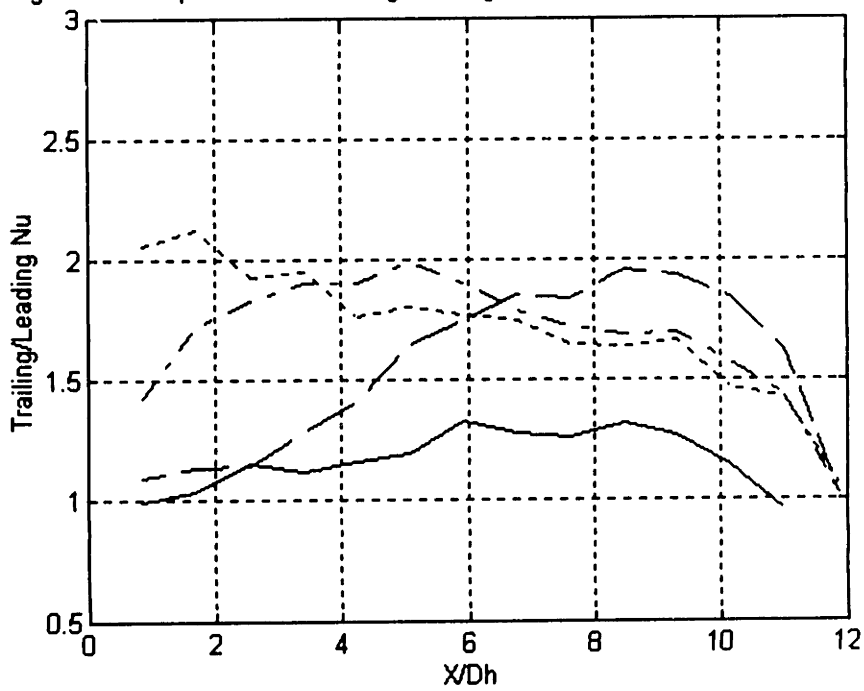

Key for Figure 4.4:

Line	Origin	Re	Ro	Δρ/ρ	B
Solid	GTL (m46)	26,000	0.14	0.32	0.39
Dashed	GTL (m45)	25,000	0.28	0.30	1.40
Dash-Dot	GTL (m44)	25,000	0.41	0.27	2.76
Dotted	GTL (m43)	25,000	0.64	0.22	5.59

Figure 4.5a: Square Model Trailing Surface Rotational Effects at Re = 50,000

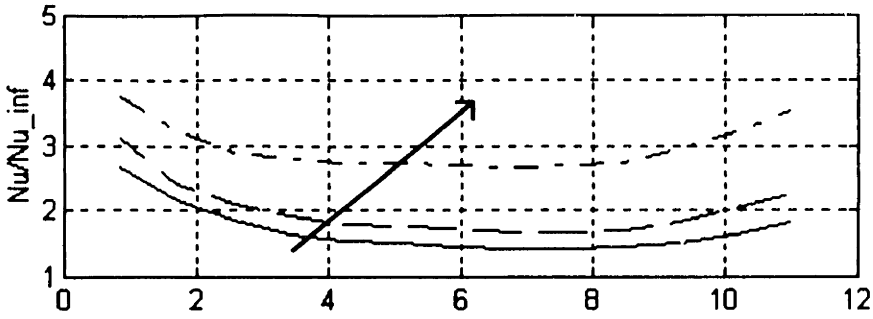

Figure 4.5b: Square Model Leading Surface Rotational Effects at Re = 50,000

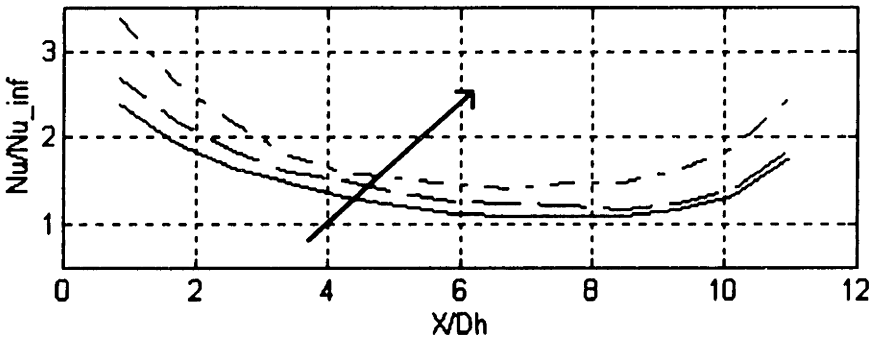

Figure 4.5c: Square Model Trailing/Leading Nu Rotational Effects at Re = 50,000

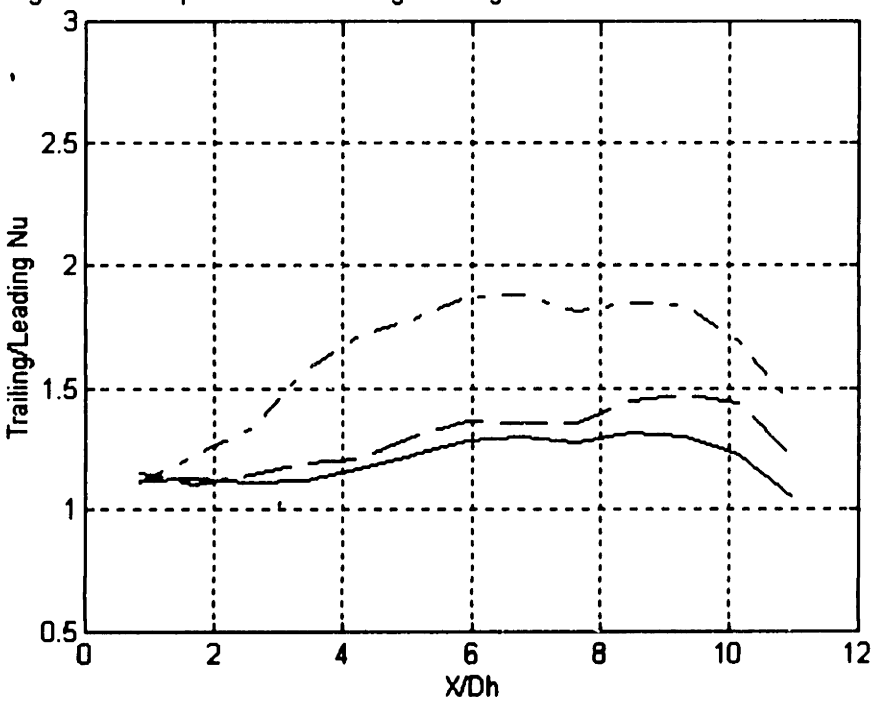

Key for Figure 4.5:

Line	Origin	Re	Ro	Δρ/ρ	B
Solid	GTL (m48)	51,000	0.11	0.31	0.24
Dashed	GTL (m51)	51,000	0.18	0.28	0.52
Dash-Dot	GTL (m50)	49,000	0.30	0.27	1.52

The data taken at a Reynolds number of 50,000, figures 4.5a-c, displays the same trend as the Re = 25,000 data. The leading and trailing surface Nu/Nu_∞ increases with increased buoyancy parameter and the trailing/leading Nu plots show the same variation as the buoyancy parameter is increased. Although, the increase in Nu/Nu_∞ with increased buoyancy parameter is larger for the Re = 50,000 data, the magnitude of the trailing/leading Nu is the same magnitude for Re = 50,000 and Re = 25,000 for the buoyancy parameters available. In general, this shows that the use of the buoyancy parameter and method of presenting the data in terms of Nu/Nu_∞ is useful in comparing data obtained at different operating conditions.

4.3.2 Effect of Reynolds Number Variation at Low Rotation

At a low rotation number of about 0.10, variations in Reynolds number do not significantly affect the leading surface Nusselt Number ratio except near the exit, but do have a significant affect near the inlet of the trailing surface. The following four sets of plots, figure 4.6 to figure 4.9, show Nu/Nu_∞ versus X/Dh for both the leading and trailing surface. Each set of plots is associated with a rotation number of 0.14 or lower. Figure 4.6 contains the data for Re ≅ 110,000, figure 4.7 for Re ≅ 50,000, figure 4.8 for Re ≅ 30,000 and figure 4.9 combines the data from the above mentioned Reynolds numbers. Each set of plots will be presented and discussed in turn.

Figure 4.6a: Square Model Trailing Surface Comparison at Re=110,000

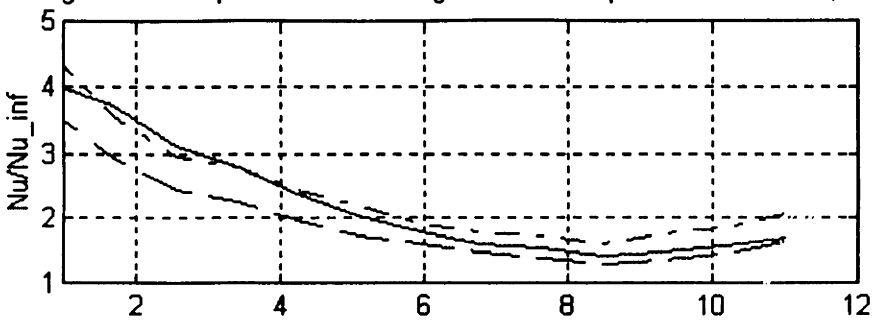

Figure 4.6b: Square Model Leading Surface Comparison at Re=110,000

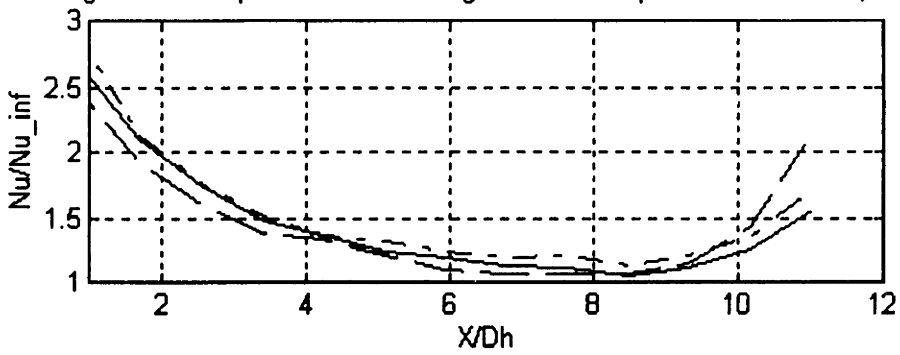

Key for Figure 4.6 (Re =110,000):

Line	Origin	Re	Ro	Δρ/ρ	B
Solid	GTL(m52)	114,000	0.04	0.29	0.04
Dashed	GTL(m54)	104,000	0.07	0.25	0.07
Dash-Dot	GTL (m53)	107,000	0.12	0.25	0.21

Discussion for Re = 110,000:

The data for the leading and trailing surfaces are similar but do provide interesting information. At a Reynolds number on the order of 110,000, the effects of rotation are slight for these small rotation numbers. The Nusselt number ratio increases from 1.4 to 1.6 on the trailing surface (X/Dh = 8) and from 1.1 to 1.2 on the leading surface (X/Dh = 8) as the rotation number was increased from 0.07 (dashed line) to 0.12 (dash-dot line).

Further, the combination of the three sets of data is consistent. Near the trailing surface inlet GTL-m52 (Re = 114,000 solid line) is closer to GTL-m53 (Re = 107,000) which is closer in Reynolds number and would have similar inlet conditions. Near the trailing surface outlet GTL-m52 (B=0.04, solid line) is closer to GTL-m54 (B=0.07, dash-dot line) which is closer in buoyancy parameter and would have similar Coriolis and buoyancy forces.

Figure 4.7a: Square Model Trailing Surface Comparison at Re=50,000

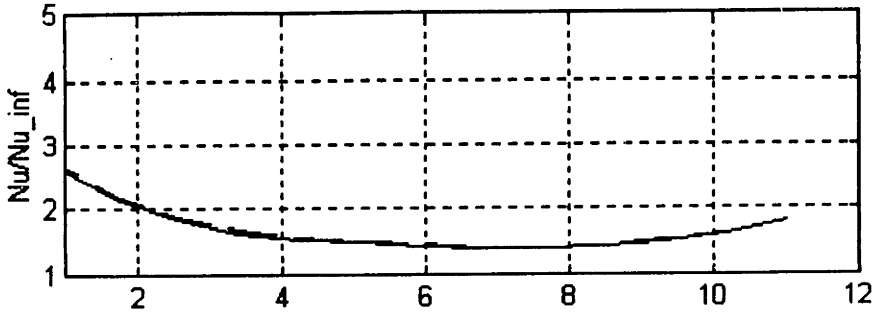

Figure 4.7b: Square Model Leading Surface Comparison at Re=50,000

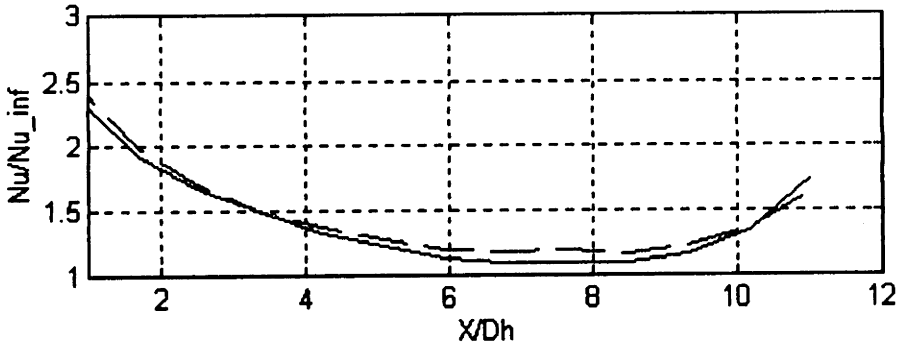

Key for Figure 4.7 (Re = 50,000):

Line	Origin	Re	Ro	Δρ/ρ	B
Solid	GTL(m48)	51,000	0.11	0.31	0.24
Dashed	GTL(m49)	53,000	0.11	0.31	0.24

Discussion for Re = 50,000:

The two cases plotted in figure 4.7a-b are at virtually the same Reynolds number, density ratio and rotation number. By comparing the data, it is apparent that the experiment is able to reproduce results within the accuracy of the experiment.

Figure 4.8a: Square Model Trailing Surface Comparison at Re=30,000

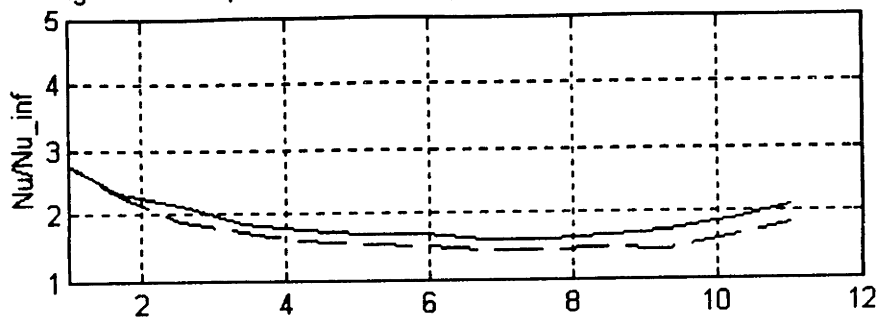

Figure 4.8b: Square Model Leading Surface Comparison at Re=30,000

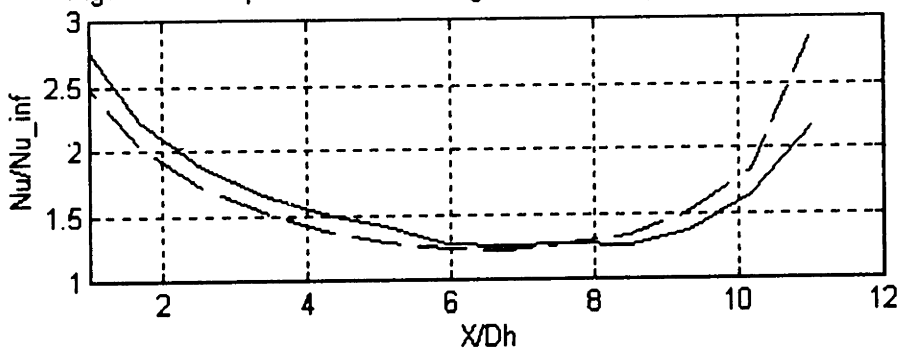

Key for Figure 4.8:

Line	Origin	Re	Ro	Δρ/ρ	B
Solid	GTL(m46)	26,000	0.14	0.32	0.39
Dashed	GTL(m42)	32,000	0.08	0.36	0.14

Discussion for Re = 30,000:

The GTL-m46 (solid line) and GTL-m42 (dashed line) are at two different conditions. On the trailing surface the solid line has a larger Nusselt number ratio than the dashed line. This is consistent with the solid line also being at a larger rotation number than then the dashed line. The leading surface shows that the minimum heat transfer shifted from X/Dh of 8 for the solid line to X/Dh of 6 for the dashed line.

Figure 4.9a: Square Model Trailing Surface Overlay

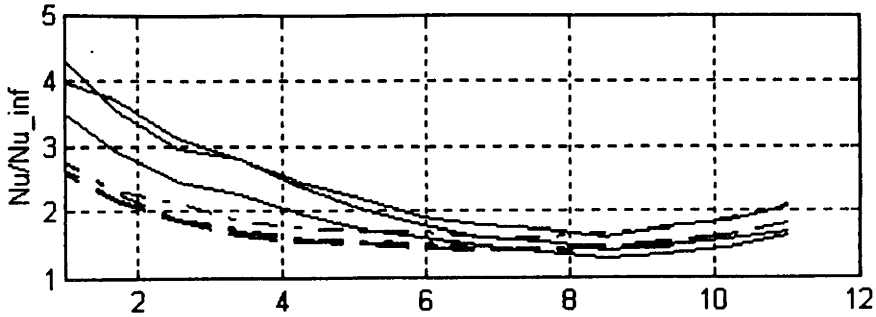

Figure 4.9b: Square Model Leading Surface Overlay

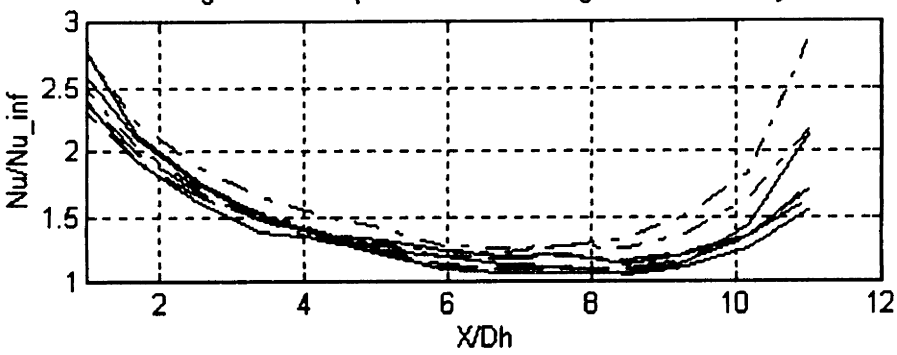

Key for Figure 4.9 (Overlay):

Line	Origin	Re	Ro	Δρ/ρ
Solid	GTL(m52,53,54)	104,000-114,000	0.04-0.12	0.25-0.29
Dashed	GTL(m48,49)	51,000-53,000	0.11	0.31
Dash-Dot	GTL (m46,42)	26,000-32,000	0.08-0.14	0.32-0.36

Discussion for Overlay:

This plot is an overlay of all of the data exhibited in the previous three plots. The solid line represents the cases where Re = 110,000, dashed line - Re = 50,000 and the dash-dotted line - Re = 30,000. Overall, the data shows that on the leading surface the Nusselt number ratio is in the same range for all three sets of conditions. On the other hand, there is a significant variation in the Nusselt number ratio near the inlet of the trailing surface. Here, the ratio increases significantly as the Reynolds number increases from 50,000 to 100,000. The variation in the trailing surface inlet heat transfer may be a result of the way the flow enters the test section. The results seems to imply that the flow impinges on the trailing surface and thus enhances the trailing surface heat transfer rate. The effect of the inlet condition appears to take longer to dissipate as the rotation number is increased.

4.3.3 Effect of Density Ratio and Reynolds Number Variation at Ro near 0.3

Figures 4.10a-c, compare three tests representing rotation numbers of 0.28, 0.25 and 0.30 as wells as density ratios of 0.30, 0.23 and 0.27 and Reynolds numbers of 25,000, 28,000 and 49,000, respectively. The data shows that, at rotation numbers on the order of 0.25, variations in density ratio are significant.

From the leading and trailing surface Nu/Nu_∞ versus X/Dh plots, it appears that all three cases have a similar radial trend but slightly varying magnitude. Assuming that Reynolds number variations are accounted for by normalizing the local Nusselt number by the stationary case, then the primary difference between GTL-m45 (solid line) and GTL-m50 (dash-dot line) is that GTL-m45 is at a rotation number of 0.28 and GTL-m50 is at a larger rotation number of 0.30. Both figure 4.10a and 4.10b show the typical trend of increased heat transfer with increased rotation number for the two cases. If variations in density ratio were not important at rotation numbers of 0.25, then GTL-m47 (dashed line), which has a rotation number of 0.25, would have a lower magnitude in heat transfer for both the leading and trailing surface then GTL-m45. However, the data shows that although the leading surface GTL-m47 (Ro = 0.25) has a lower magnitude than GTL-m50 (Ro = 0.28), the trailing surface Nu/Nu_∞ is larger for the lower rotation number test case.

Figure 4.10c shows that the buoyancy parameter is an effective way of comparing data sets of varying density ratios and rotation numbers. In figure 4.10c, the two lines that overlap (solid line and dash-dot line) are at a buoyancy parameter of 1.40 and 1.52. The third test case which is at a buoyancy of 0.88 shows a much larger trailing/leading Nusselt number ratio in the region of X/Dh from 5 to 11. The sharp rise is due to enhanced heat transfer on the trailing surface, however, it is not clear why the trailing surface heat transfer is enhanced for the lower density ratio (lower buoyancy parameter) test case.

The heat transfer distribution for the three cases of interest have the same basic shape as can be viewed from the subsequent heat transfer maps.

Figure 4.10a: Square Model Trailing Surface Ro ~0.3

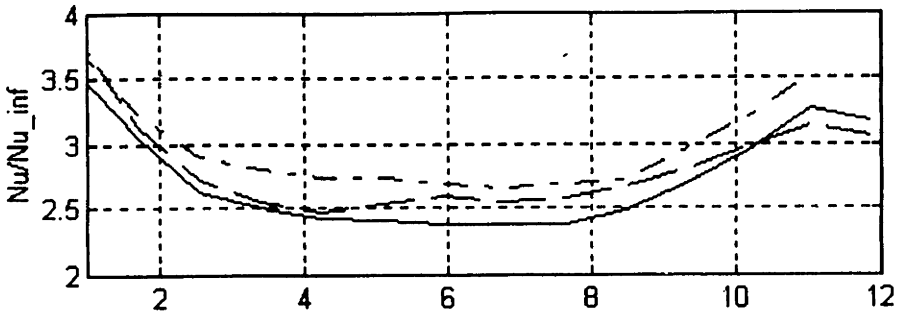

Figure 4.10b: Square Model Leading Surface Ro ~0.3

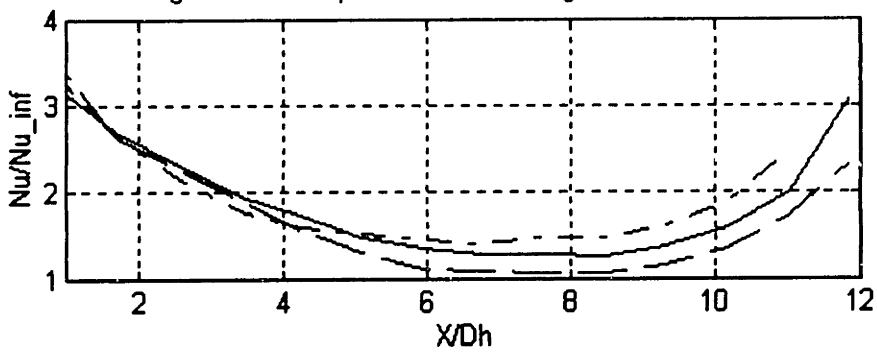

Figure 4.10c: Square Model Trailing/Leading Nu Ro ~0.3

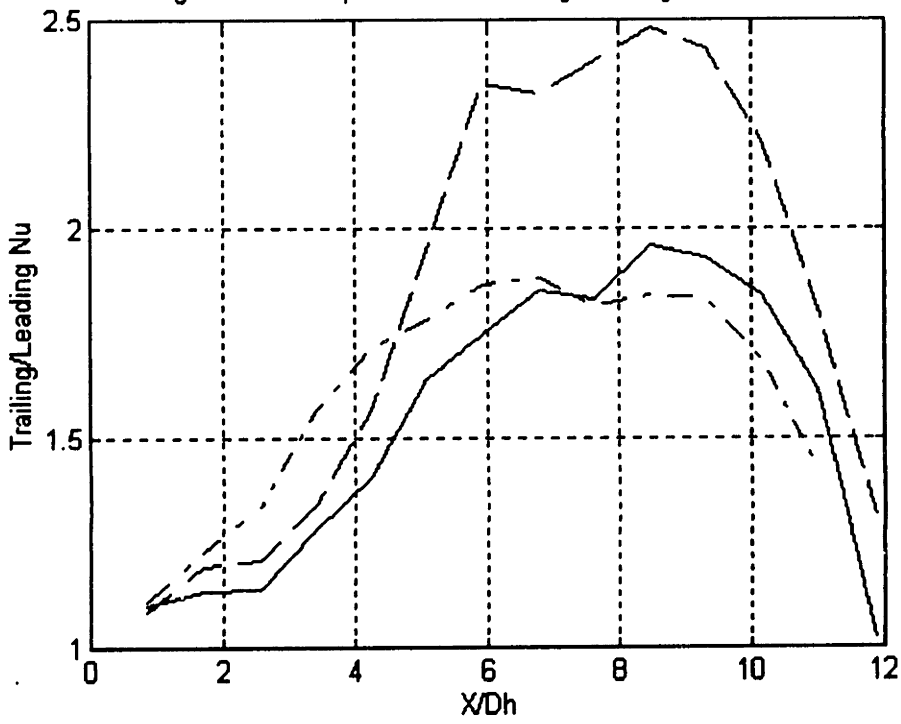

Key for Figure 4.10:

Line	Origin	Re	Ro	Δρ/ρ	B
Solid	GTL(m45)	25,000	0.28	0.30	1.40
Dashed	GTL(m47)	28,000	0.25	0.23	0.88
Dash-Dot	GTL (m50)	49,000	0.30	0.27	1.52

Heat Transfer Map M45

Re = 25,000, Ro = 0.28, $\Delta\rho/\rho$ = 0.30, B = 1.40

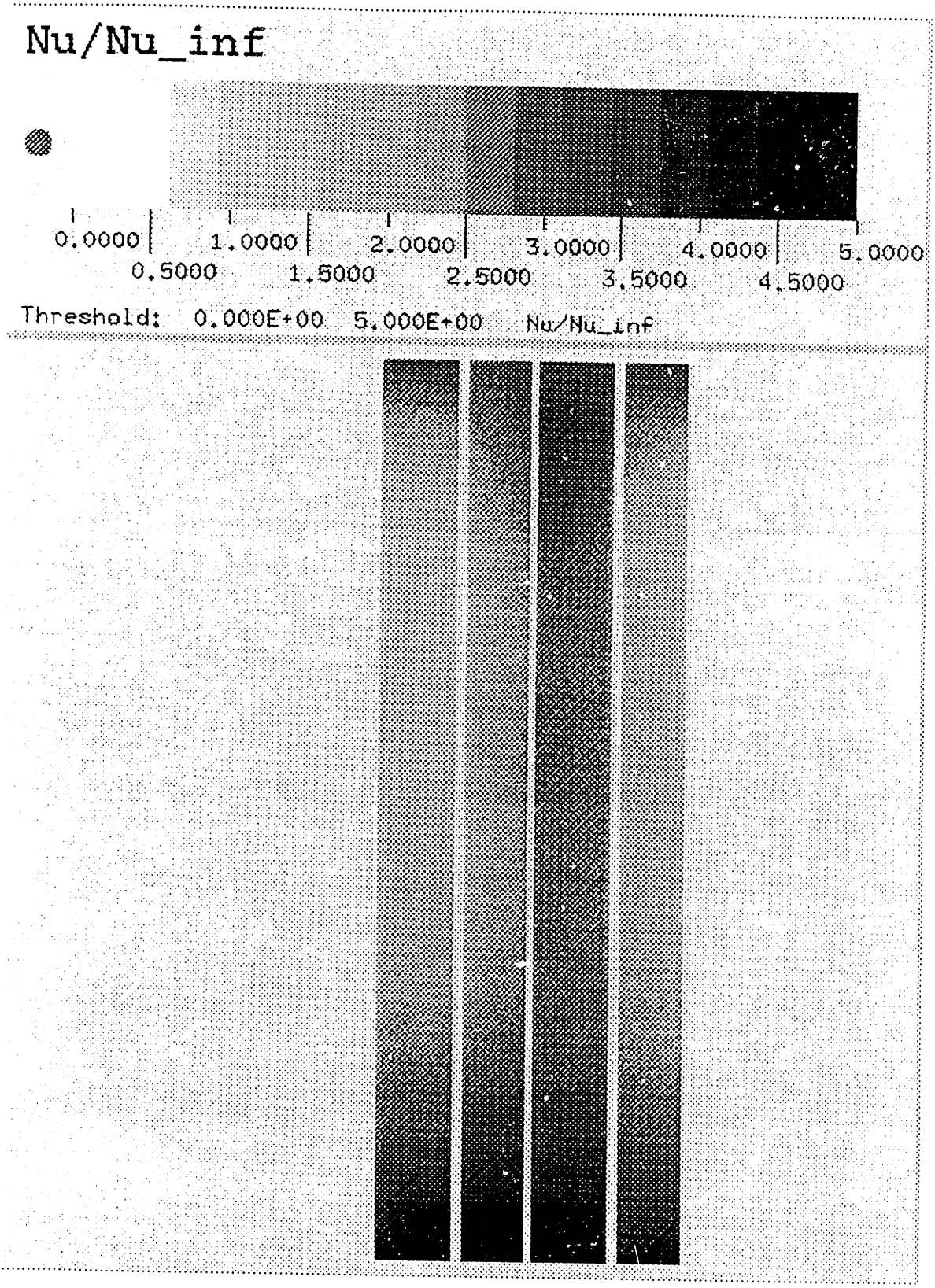

Heat Transfer Map M50

Re = 49,000, Ro = 0.30, $\Delta\rho/\rho$ = 0.27, B = 1.52

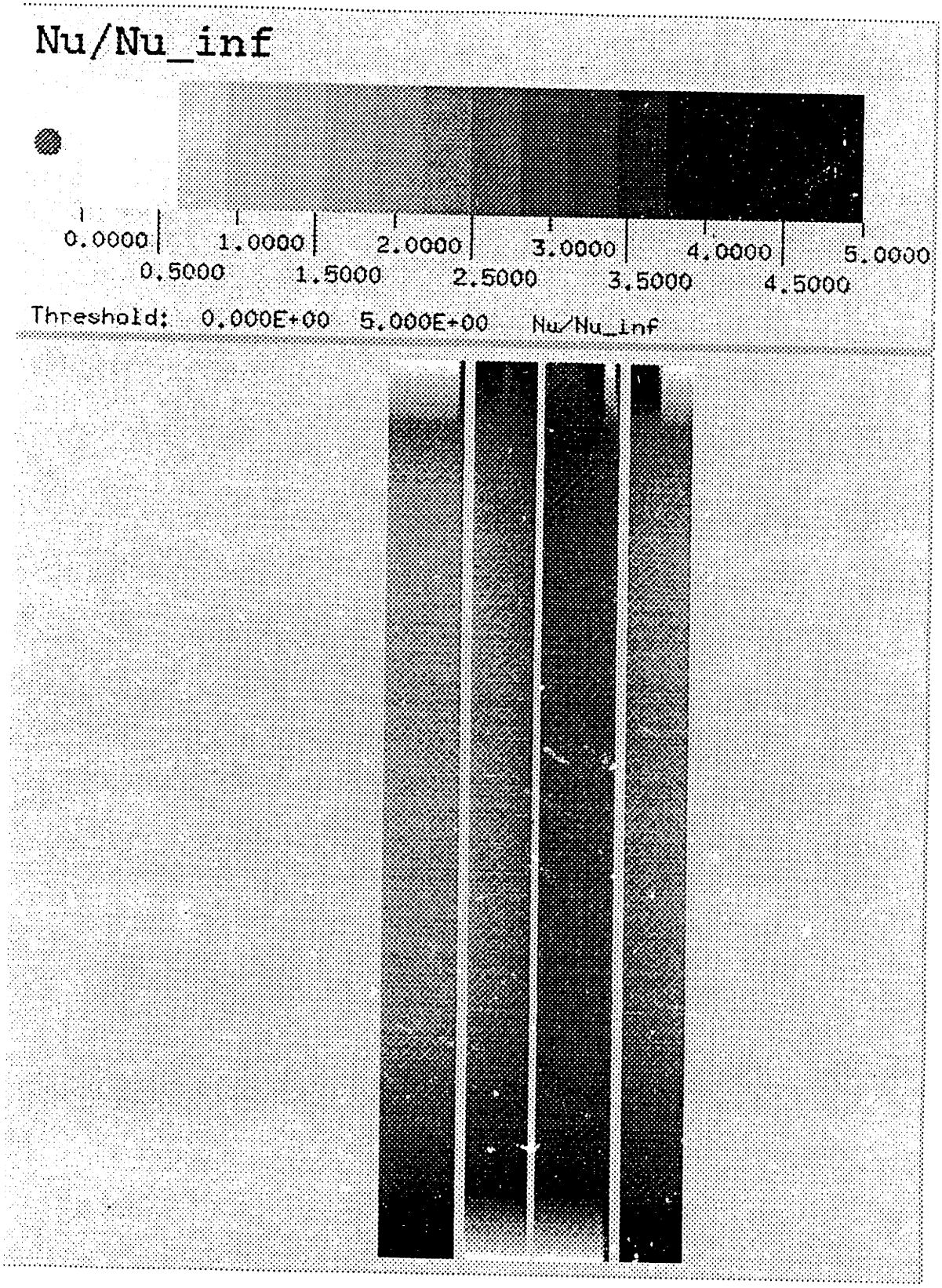

Heat Transfer Map M47

Re = 28,000, Ro = 0.25, $\Delta\rho/\rho$ = 0.23, B = 0.88

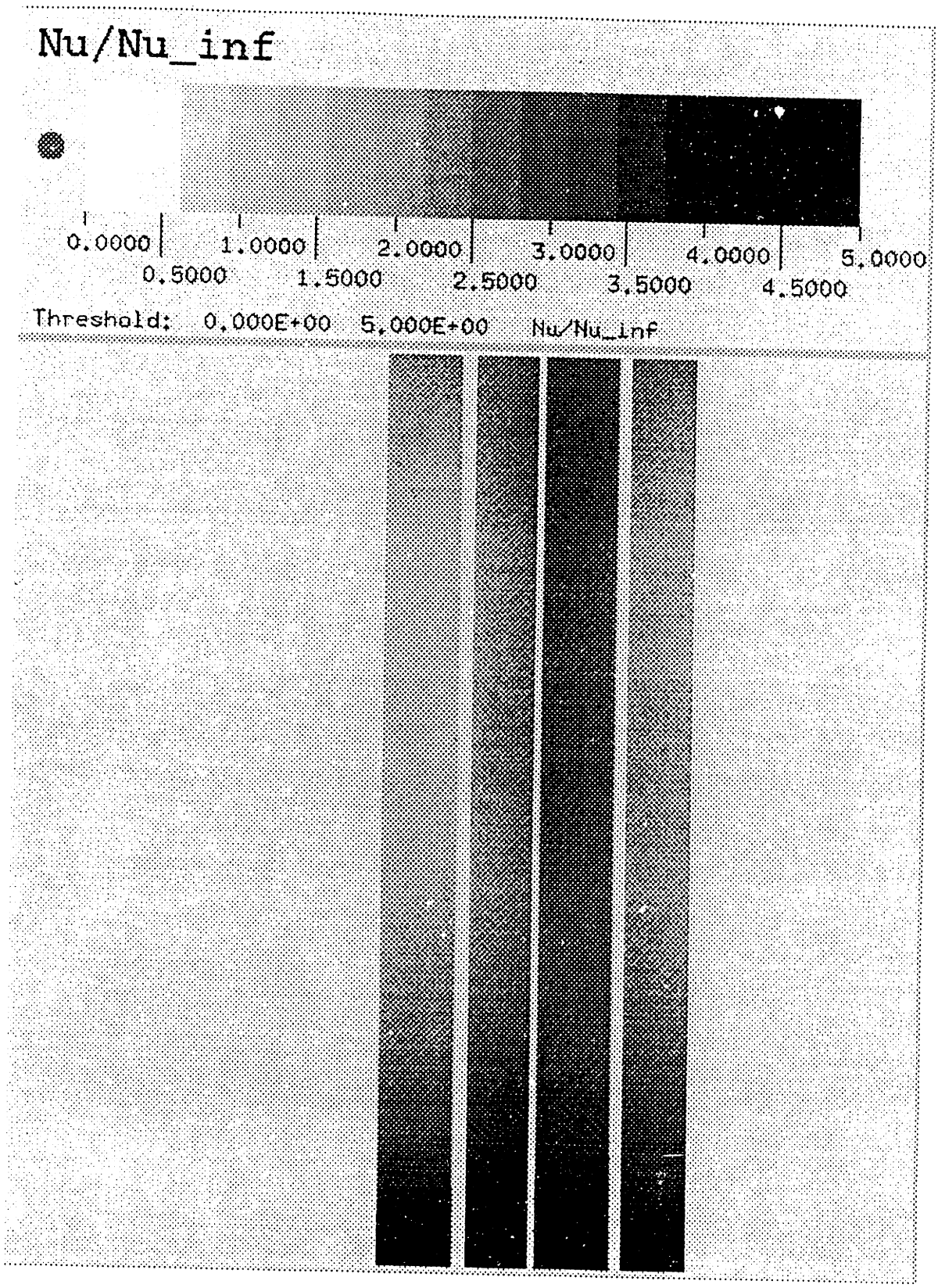

4.4 Smooth Rectangular Model Results

This section presents the data obtained for the smooth rectangular model. The aspect ratio of the model is 3.3 (0.635 in X 0.193 in), with the small sides being the leading and trailing surface.

4.4.1 Effect of Rotation at Re $\approx$ 25,000

Below is a series of heat transfer maps which show the effect of rotation on the smooth rectangular test section. Each test is held at a Reynolds number close to 25,000 as the buoyancy parameter was varied from 0.18, to 1.81 to 3.77. The maps represent the Nusselt number ratio on the unwrapped surface of the model. From left to right, the figures in the map represent the leading, side-front, trailing and side-back surface. Figures 4.11a-c show the magnitude of the heat transfer results. It should be noted that for m26 a region of data on the trailing surface is known to be incorrect as a result of particles coating the side mirror. The corrupted data points were removed in the line plots and smoothed in the heat transfer maps. Data for the three other surfaces of that test case are believed to be accurate.

From the maps it can be seen that at a buoyancy parameter of 0.18 the heat transfer distribution appears to be uniform on the surface of the model. At a buoyancy parameter of 1.81 the trailing surface near the outlet becomes significantly cooled and that with increased rotation the region of the trailing surface which is cooled extends closer toward the inlet. This phenomenon is associated with the formation of the Coriolis cross stream vortices. At larger rotation number the vortices become stronger and develop faster thus having more of an affect earlier in the channel.

Figures 4.11a-c display the magnitude of the heat transfer result for the three buoyancy parameters. Figures a-b plot Nu/Nu_∞ versus X/Dh for the trailing and leading surfaces. Figure c displays the trailing/leading Nusselt number with increased distance along the test section. The data shows that at a buoyancy parameter of 0.18 the trailing surface Nu/Nu_∞ is approximately level, at about 1.8, where as the leading surface Nu/Nu_∞ decreases from about 1.5 to 1.1 with increased radial distance. At a buoyancy parameter of 1.81, the leading surface Nu/Nu_∞ slightly increases from 1 near the inlet to 1.2 near the outlet where as trailing surface heat transfer increases from Nu/Nu_∞ near 2 at the inlet and

to 4 near the outlet. The heat transfer rate, in general, increased as the buoyancy parameter was increased from 1.81 to 3.77.

More data is needed to form solid conclusions however, it appears that although the Coriolis force is developing faster with increased buoyancy parameter, the resulting affect on the heat transfer distribution is different from what was seen for the square model. For example, the trailing/leading Nu for the buoyancy parameters in the range of 1.5 to 3.5 increased from 2 to 3.5 for the smooth rectangular model yet decreased from 2.0-1.5 for the square model. In addition, the large increase in heat transfer seen near the inlet of the square model is not present in the rectangular model data.

Heat Transfer Map M24

Re = 28,000, Ro = 0.10, $\Delta\rho/\rho$ = 0.30, B = 0.18

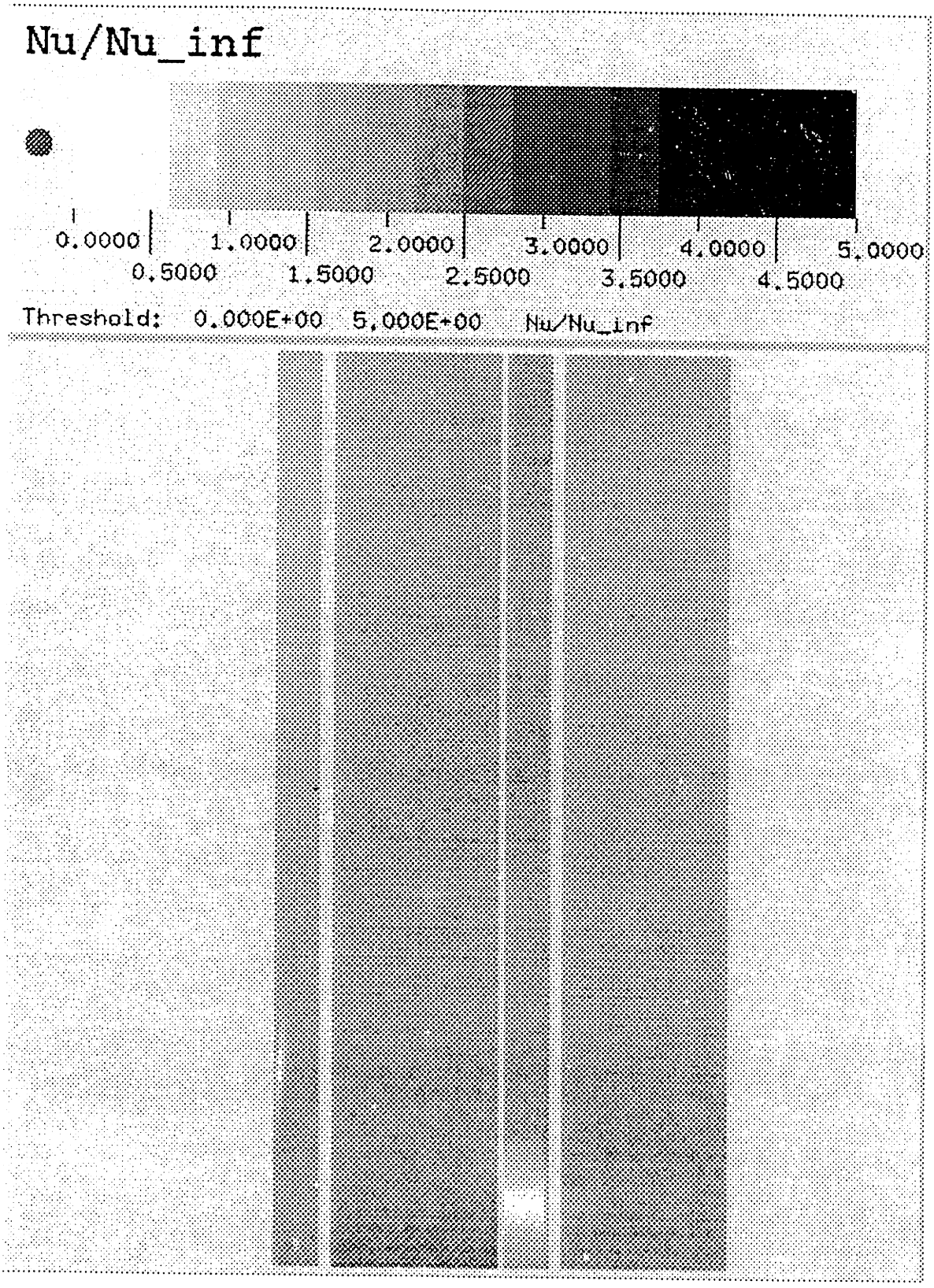

Heat Transfer Map M25

Re = 25,000, Ro = 0.32, $\Delta\rho/\rho$ = 0.29, B = 1.81

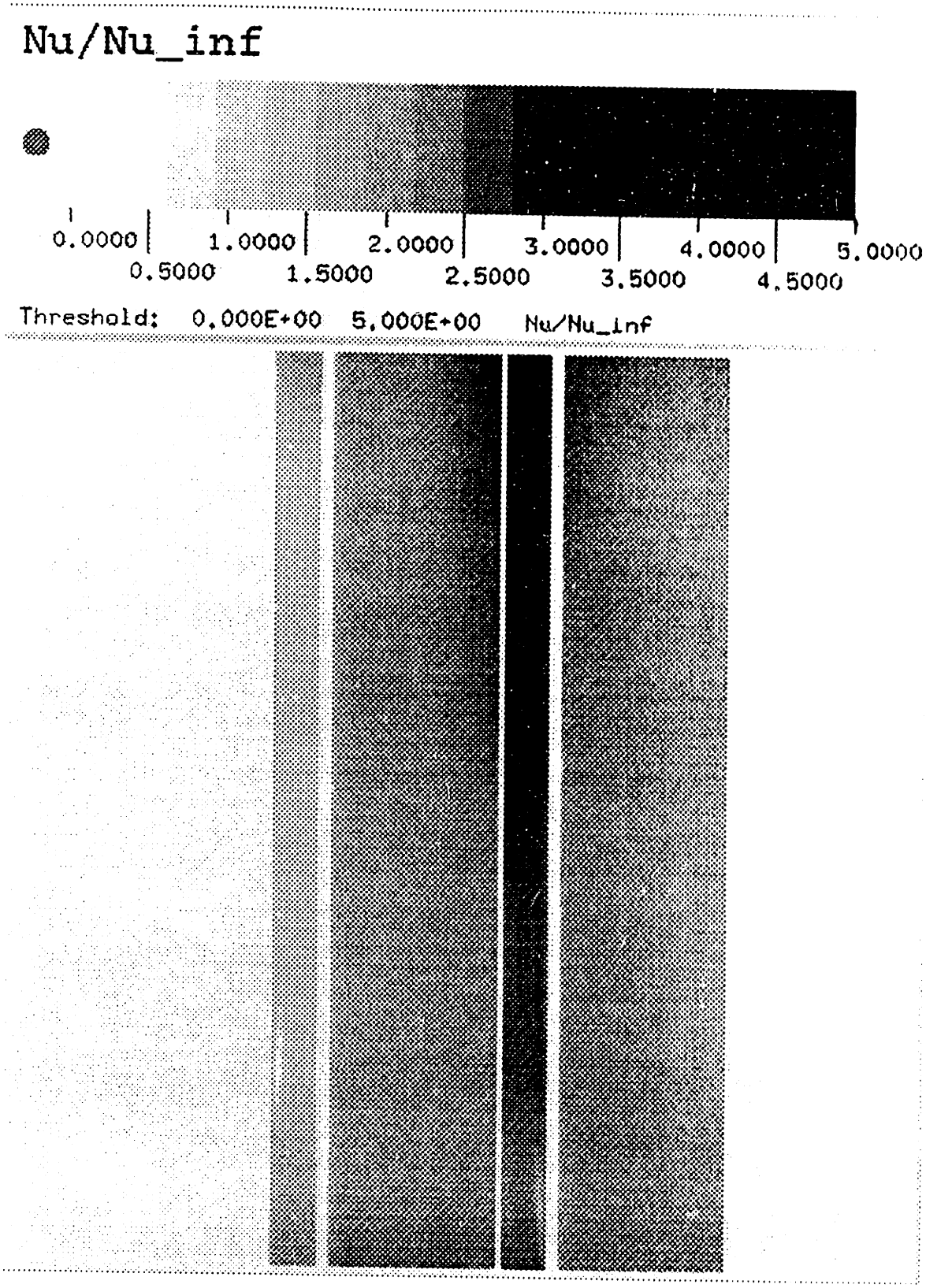

Heat Transfer Map M26

Re = 25,000, Ro = 0.49, $\Delta\rho/\rho$ = 0.25, B = 3.77

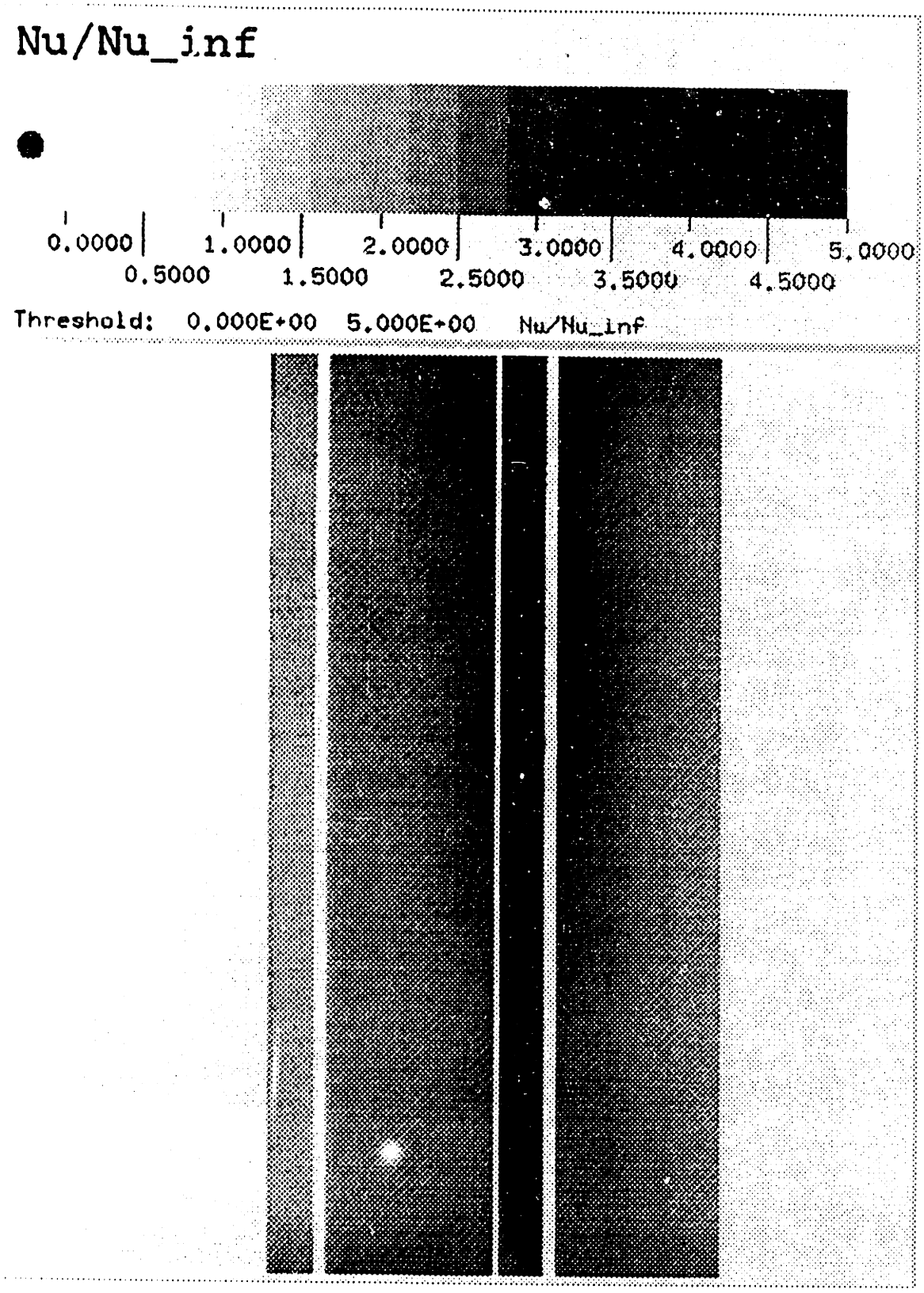

Figure 4.11a: Smooth Rect. Trailing Surf. Buoyancy Parameter Variations

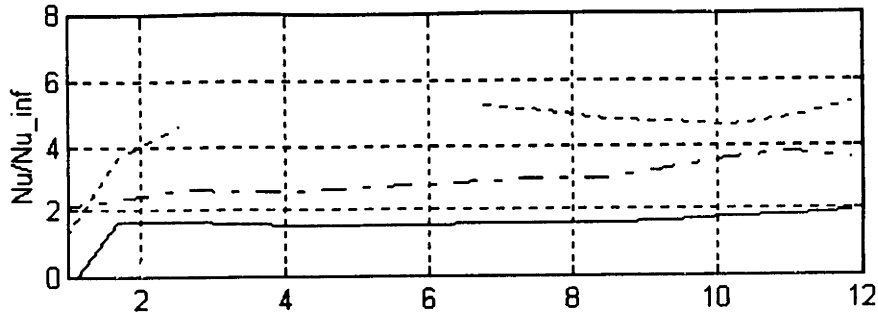

Figure 4.11b: Smooth Rect. Leading Surf. Buoyancy Parameter Variations

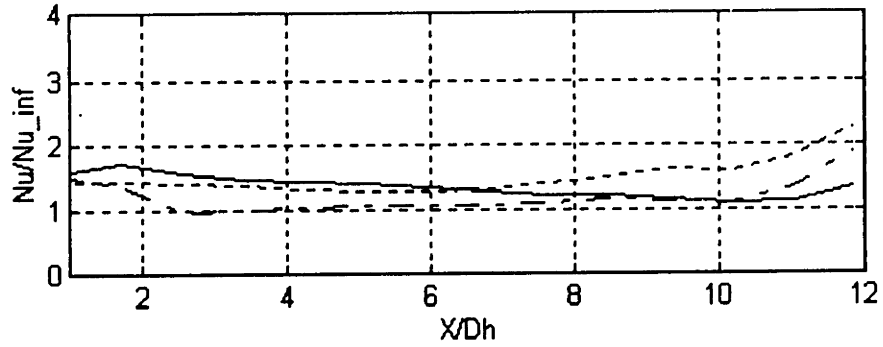

Figure 4.11c: Smooth Rect. Trailing/Leading Nu Buoyancy Parameter Variations

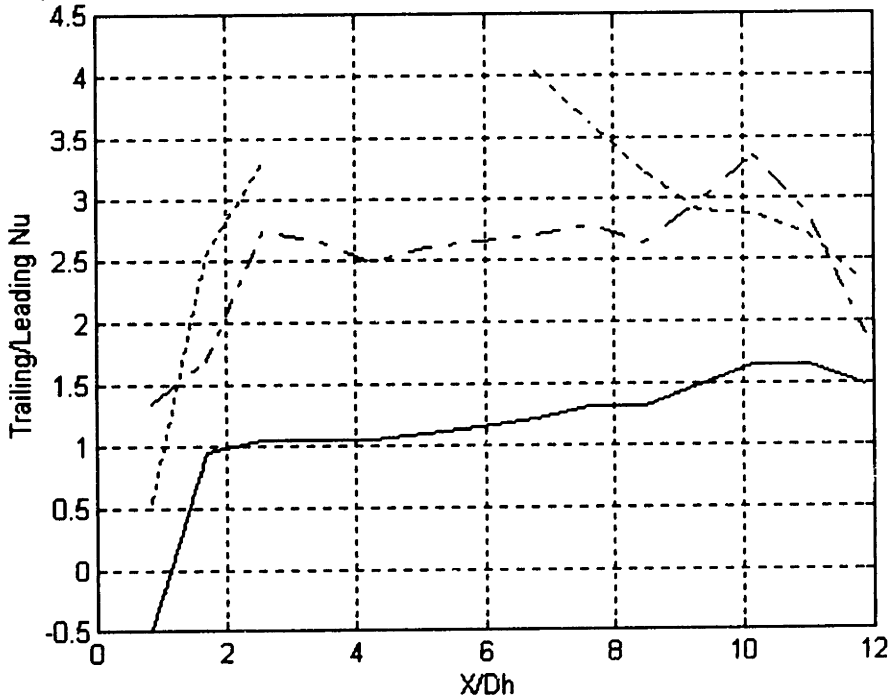

Key for Figure 4.11:

Line	Origin	Re	Ro	Δρ/ρ	B
Solid	GTL(m24)	28,000	0.10	0.30	0.18
Dash-Dot	GTL(m25)	25,000	0.32	0.29	1.81
Dotted	GTL(m26)	25,000	0.49	0.25	3.77

4.5 Ribbed Rectangular Model Results

The data presented in this section demonstrates the significant cooling enhancement caused by the ribbed surface. The model has an aspect ratio of 3.3 (0.635 in X 0.193 in), with the small sides being the leading and trailing surface. The ribs, which are located on the leading and trailing surfaces are described in more detail in Section 2.2.

4.5.1 Effect of Buoyancy Parameter Re ≈ 25,000

The heat transfer maps show the heat transfer distribution for buoyancy parameters of 0.27, 0.72, 1.38 and 3.63. Even at the lowest buoyancy parameter of 0.27, which was at a rotation number of 0.12, significant cooling appears at the outlet of the test section. (Recall, that for the smooth square model, and the smooth rectangular model, significant cooling did not occur for small buoyancy parameters.) As the buoyancy parameter is increased the cooling near the outlet appears to begin at locations closer to the inlet. This is result due of the Coriolis generated flows. At the largest buoyancy parameter of 3.63, a significant enhancement of heat transfer is apparent on the leading surface outlet region. For all of the maps, the side surfaces show the continuity between the trailing and leading surface heat transfer. The Coriolis cross stream vortices travel from the trailing surface along the side walls to the leading surface. When the flow passes by the side walls, the flow temperature increases as heat is being added from the side walls. Since the flow temperature increases from the leading to trailing surface, the heat transfer decreases. The decrease in heat transfer along the side walls is clearly seen in the heat transfer maps.

The ribs are responsible for the increased heat transfer. As the flow encounters the ribs, the near wall turbulence is increased, the boundary layer is thinned and vortices near the ribs are generated. As a result, the near wall flow is able to transport the heat from the wall to the bulk flow more effectively.

Figures 4.12 a-c show the magnitude of the Nusselt number ratio and the magnitude of the trailing/leading Nu for the cases depicted in the heat transfer maps. Figures a and b show an increase in Nu/Nu_∞ as the buoyancy parameter is increased. The exception to this trend is the leading surface for the buoyancy parameter of 0.27. In this case, the Nusselt number ratio is 2.2 near the inlet, decreases to a minimum of 1.1 at about X/Dh of 7 and then increases to 1.4. From figures a and b it can also be seen that the flow enters the ribbed rectangular test section the same way the flow entered the smooth

rectangular test section since variations in heat transfer below X/Dh of 3 are similar for the two models.

Figure 4.12c, trailing/leading Nusselt number versus X/Dh, shows a trend similar to the trend found for the smooth square model. The relative trailing to leading Nusselt number changes with increased buoyancy parameter. At a low buoyancy parameter of 0.27, the trailing surface outlet region has noticeably larger heat transfer than the corresponding leading surface. As the buoyancy parameter is increased to 0.72, the trailing surface is cooled more than the leading surface in a region which is closer the center of the test section. As the buoyancy parameter is increased to 1.38, the trailing to leading Nusselt number ratio is largest near the entrance of the model. At the largest buoyancy parameter of 3.63, the trailing/leading Nusselt number is lower than in the previous case, with the largest ratio again occurring near the inlet region. The variation in trailing/leading Nu with increased buoyancy parameter is a result of the interaction between the Coriolis and buoyancy forces. The variations trailing/leading Nu versus X/Dh with increased buoyancy parameter is discussed further in section 4.6 where it is also compared to the variation found for the smooth square model.

Heat Transfer Map M33

Re = 26,000, Ro = 0.12, $\Delta\rho/\rho$ = 0.30, B = 0.27

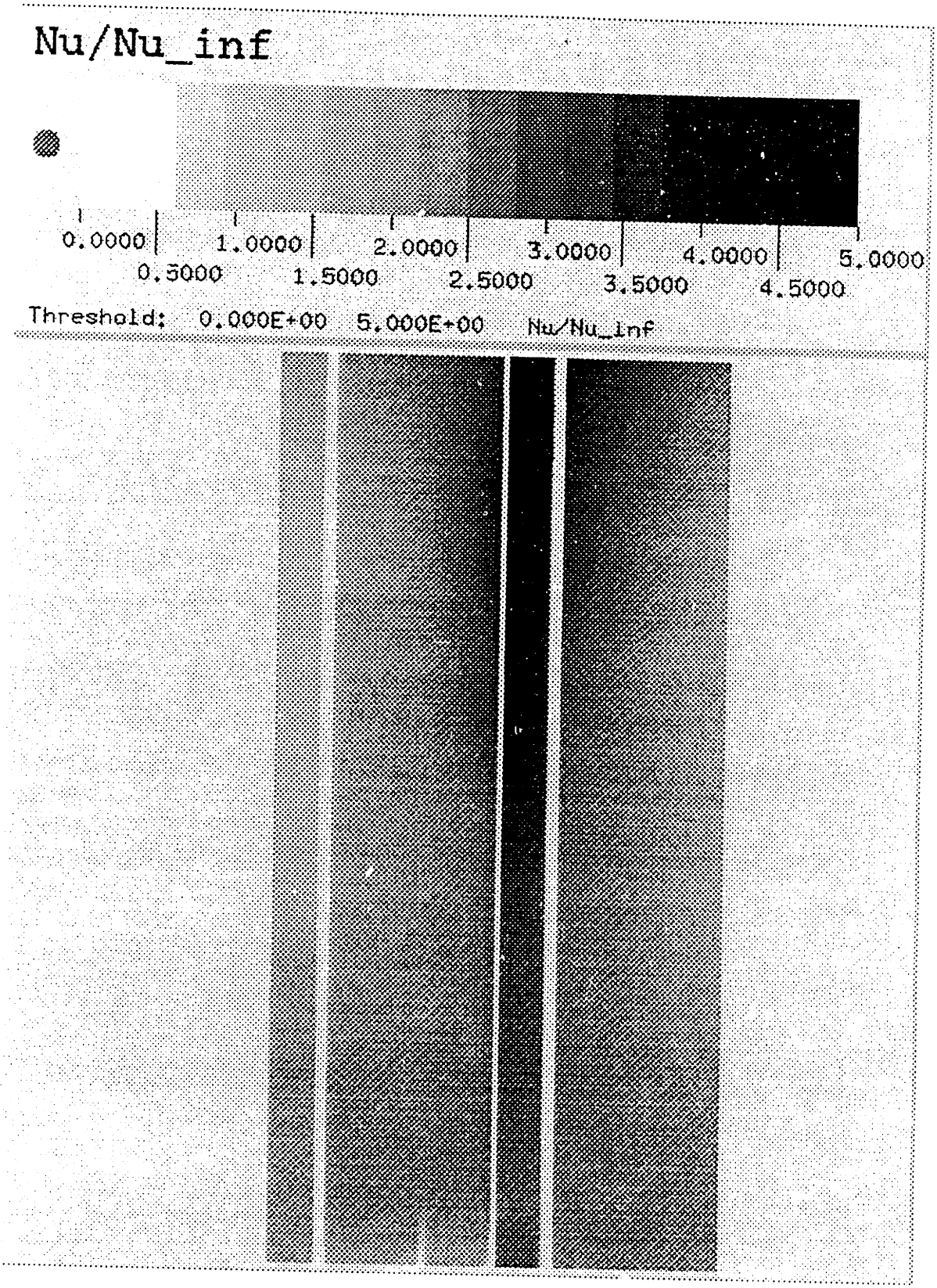

Heat Transfer Map M34

Re = 24,000, Ro = 0.21, $\Delta\rho/\rho$ = 0.26, B = 0.72

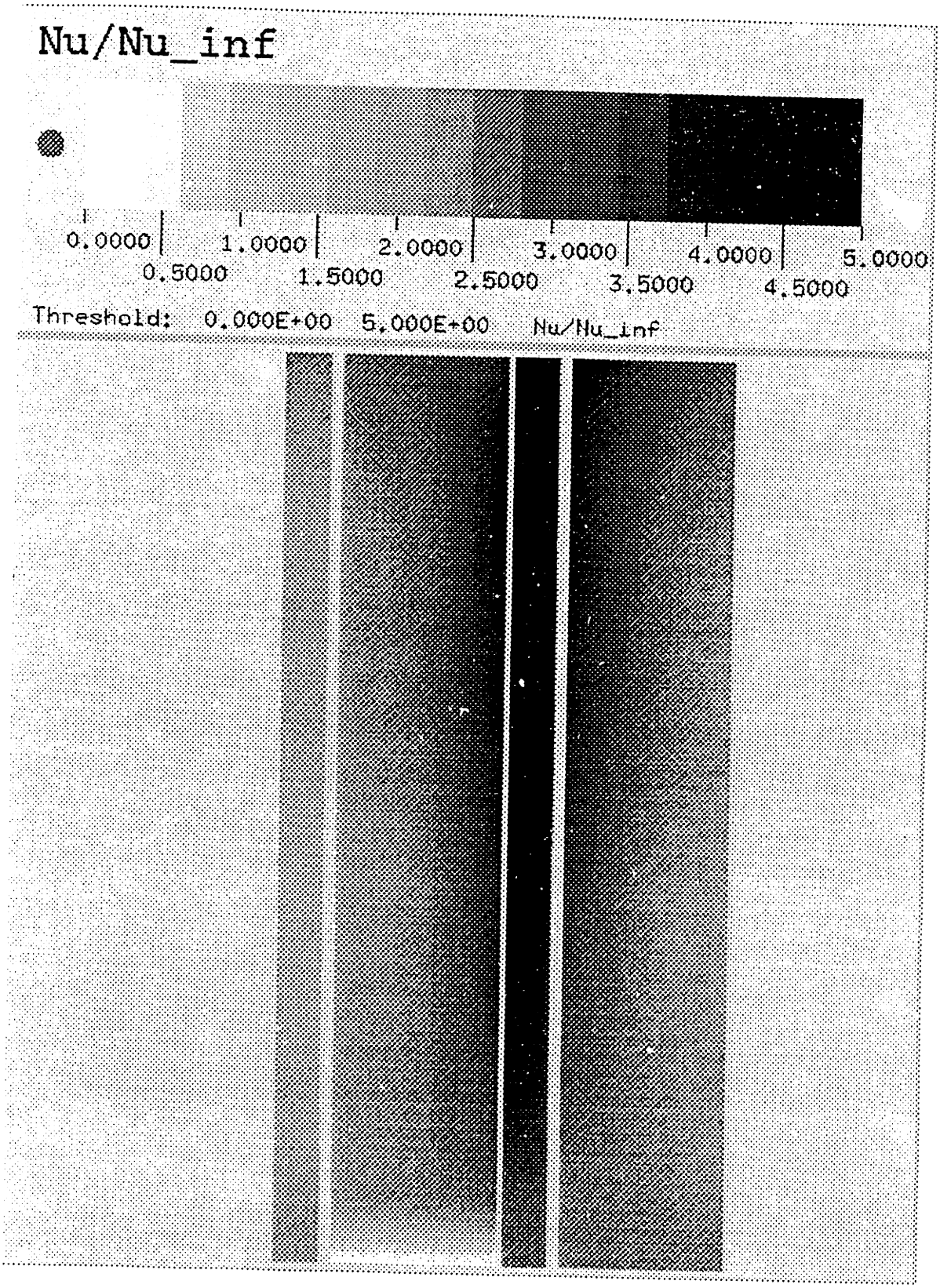

Heat Transfer Map M35

Re = 26,000, Ro = 0.30, $\Delta\rho/\rho$ = 0.25, B = 1.38

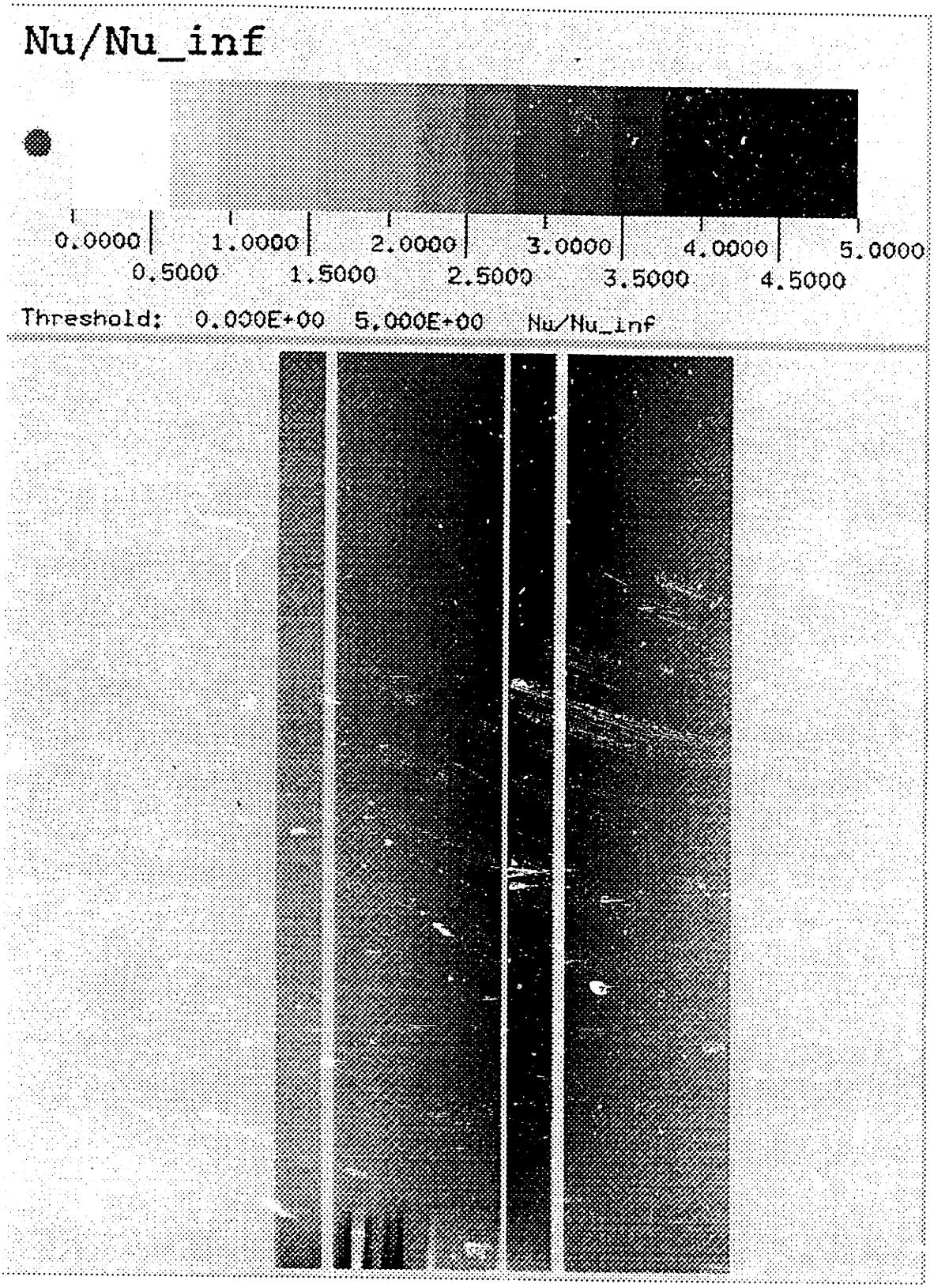

Heat Transfer Map M36

Re = 26,000, Ro = 0.49, $\Delta\rho/\rho$ = 0.21, B = 3.63

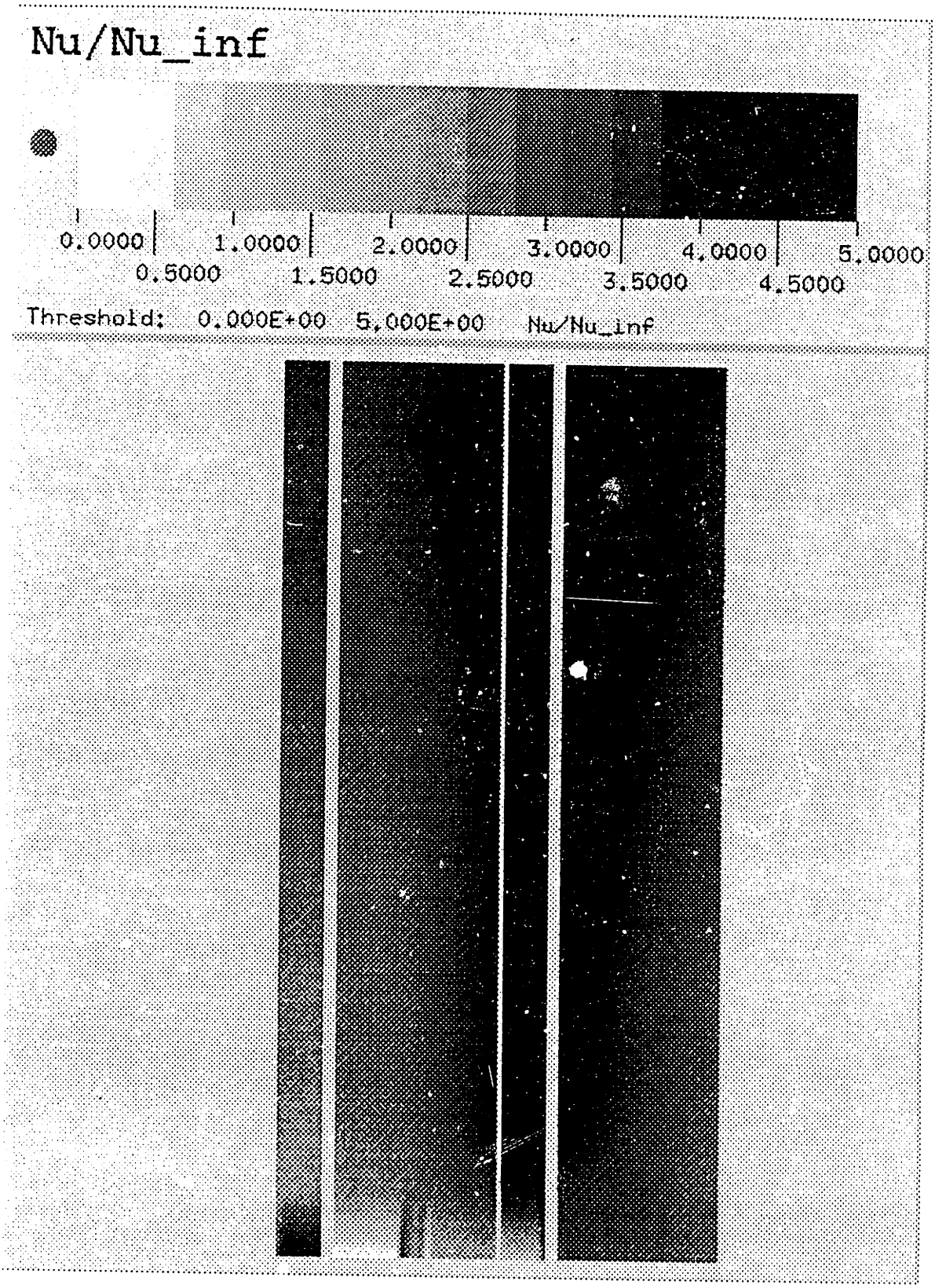

Figure 4.12a: Ribbed Rect. Trailing Surf. Buoyancy Parameter Variations

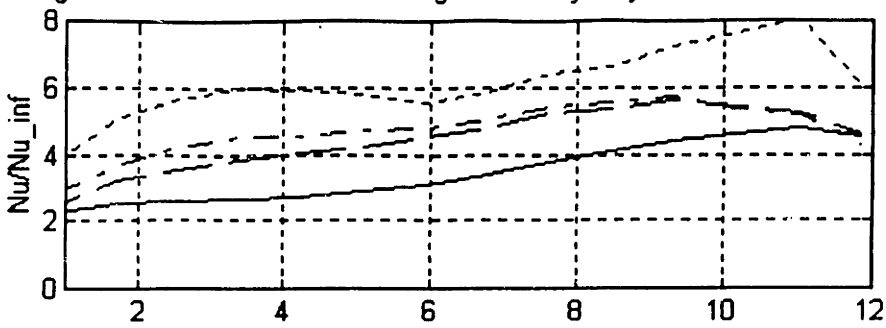

Figure 4.12b: Ribbed Rect. Leading Surf. Buoyancy Parameter Variations

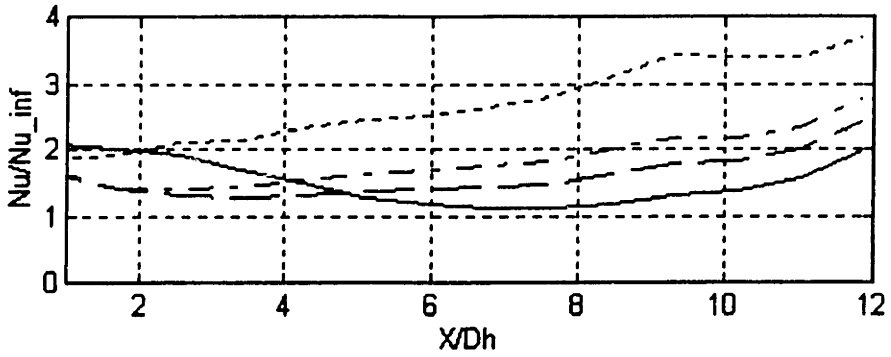

Figure 4.12c: Ribbed Rect. Trailing/Leading Nu Buoyancy Parameter Variations

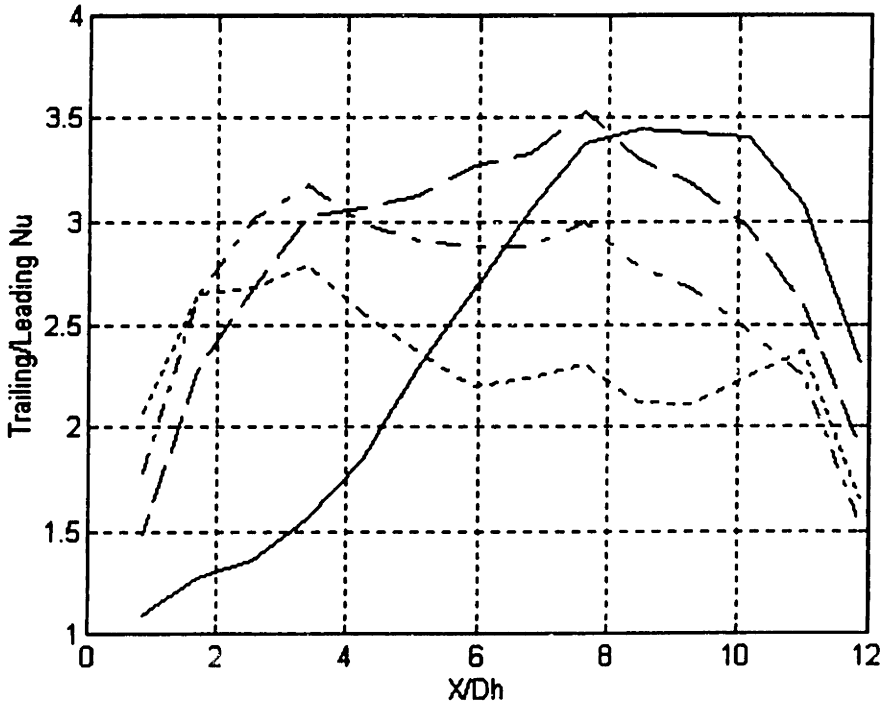

Key for Figure 4.12:

Line	Origin	Re	Ro	Δρ/ρ	B
Solid	GTL(m33)	26,000	0.12	0.30	0.27
Dashed	GTL(m34)	24,000	0.21	0.26	0.72
Dash-Dot	GTL(m35)	26,000	0.30	0.25	1.38
Dotted	GTL (m36)	26,000	0.53	0.21	3.63

4.6 Comparison of Results for Different Geometries

This section discusses the heat transfer results for each model. The data indicates that the Coriolis and buoyancy forces affect the heat transfer distribution differently for each model geometry. Further, the data indicates that the flow entering the model has an affect on the inlet heat transfer which depends on the cross section of the model.

4.6.1 Surface Heat Transfer Distribution

The heat transfer maps presented in sections 4.3 to 4.5 show the different patterns of heat transfer distribution. The inlet region of the square model showed an increase in heat transfer for all buoyancy parameters, where as the inlet region of the rectangular models did not. Further, at the lowest buoyancy parameter (below 0.4), enhanced heat transfer occurred at the outlet of the trailing surface for the ribbed rectangular model but was not encountered for the smooth models. In addition, at larger buoyancy parameters, the maps for the ribbed model continued to show signs of heat transfer rates that were larger than that of the smooth models.

Figures 4.13a-c and 4.14a-c compare the results obtained for the different geometries at a low and moderate buoyancy number respectively. Figures 4.13a-c demonstrate that at low buoyancy parameters, under 0.4, the smooth square and smooth rectangular model show the same magnitude and trend for both the leading and trailing surfaces. The figure also shows the significant heat transfer on the trailing surface ribbed rectangular model introduced due to the mixing caused by the ribs. Figures 4.14a-c show that at moderate buoyancy parameters, of about 1.4, the ribbed rectangular and smooth rectangular models show the same trend for both the leading and trailing surfaces. The magnitude of Nu/Nu_{∞}, however, is again larger for the ribbed model.

An experiment performed by Han [3], which investigated the effects of ribs on opposing walls for a stationary, square channel, found that the heat transfer for 45° ribs nearly doubled over the smooth wall data. The results in figures 4.14 and 4.13 show that the ribbed rectangular heat transfer is about 1.5 to 2.5 times the smooth rectangular heat transfer except for the leading surface at the low buoyancy parameter. In general, the GTL results are consistent with the enhancement found by Han.

Figures 4.4c and 4.12c, which are replotted for the readers convenience, show that as the rotation number is increased, the peak in trailing/leading Nu shifts from the outlet to the inlet for both the smooth square model and the ribbed rectangular model. The major difference between the two data sets however, is the larger magnitude of trailing/leading Nu for the ribbed rectangular model. The peak is as large as 3.5 for the ribbed rectangular model and is a maximum of 2 for the smooth square model. In addition, the peak near the outlet is present at a buoyancy number of 0.27 for the ribbed rectangular data set where as the peak near the outlet occurs at a buoyancy number of 1.40 for the smooth square model.

Figure 4.13a: Low Buoyancy Parameter Trailing Surface Varying Geometries

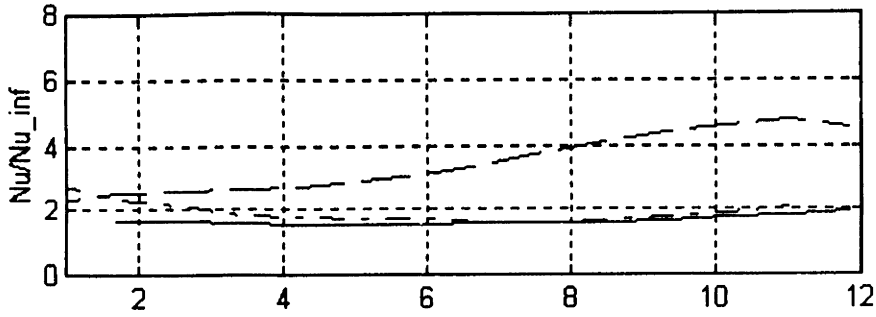

Figure 4.13b: Low Buoyancy Parameter Leading Surface Varying Geometries

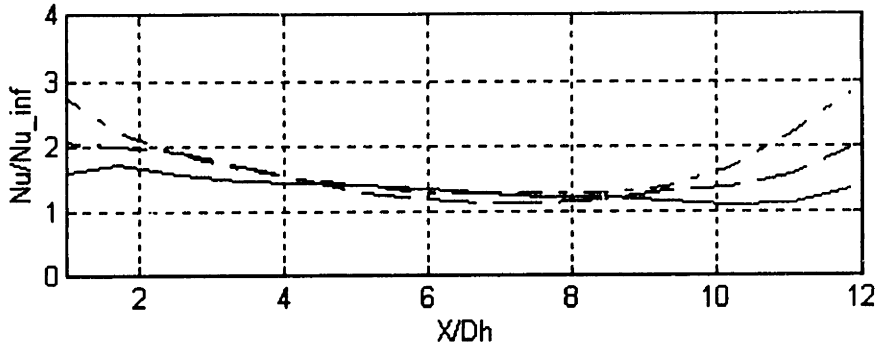

Figure 4.13c: Low Buoyancy Parameter Trailing/Leading Nu Varying Geometries

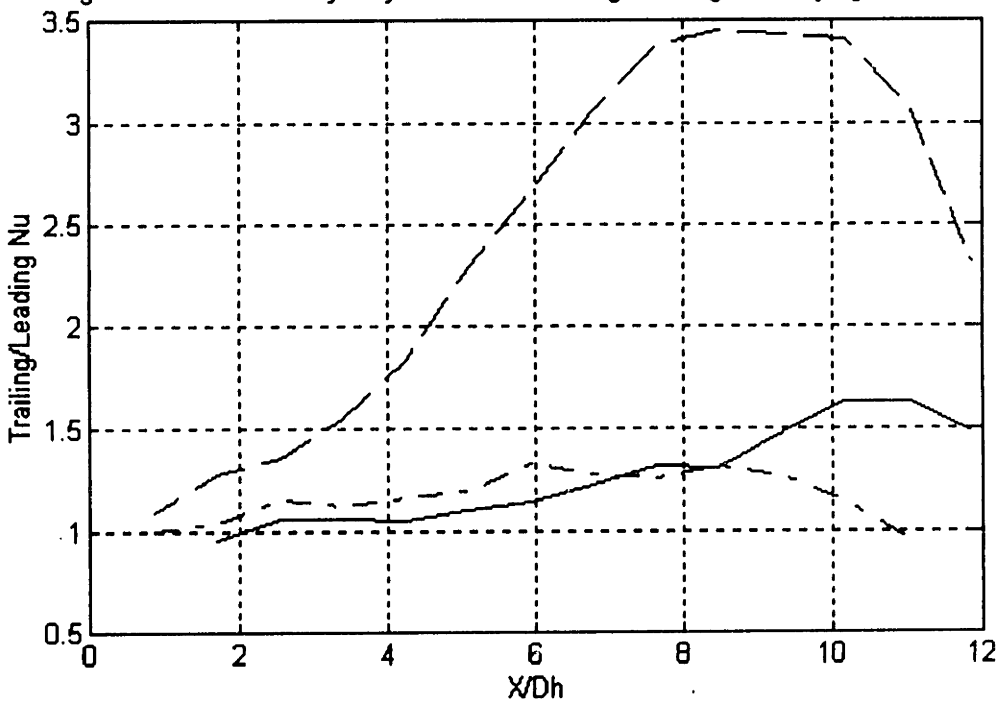

Key for Figure 4.13:

Line	Origin	Re	Ro	Δρ/ρ	B	Model
Solid	GTL(m24)	28,000	0.10	0.30	0.18	Smooth Rectangle
Dashed	GTL(m33)	26,000	0.12	0.30	0.27	Ribbed Rectangle
Dash-Dot	GTL(m46)	26,000	0.14	0.32	0.39	Smooth Square

Figure 4.14a: Moderate Buoyancy Parameter Trailing Surface Varying Geometries

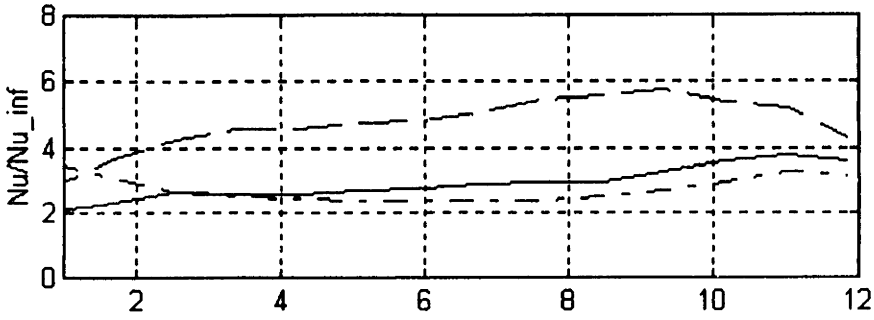

Figure 4.14b: Moderate Buoyancy Parameter Leading Surface Varying Geometries

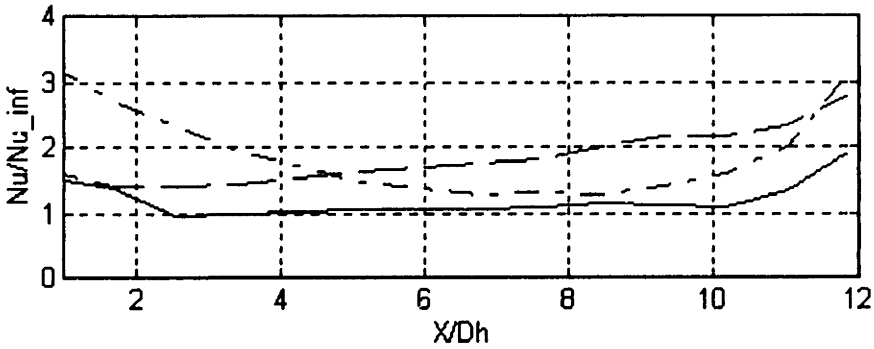

Figure 4.14c: Moderate Buoyancy Parameter Trailing/Leading Nu Varying Geometries

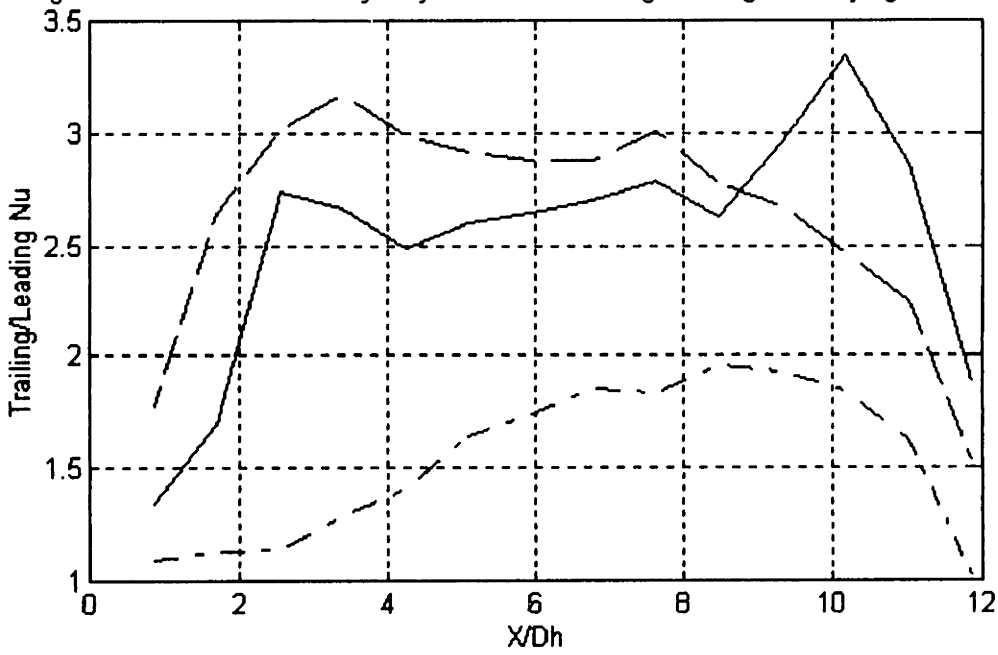

Key for Figure 4.14:

Line	Origin	Re	Ro	Δρ/ρ	B	Model
Solid	GTL(m25)	25,000	0.32	0.29	1.81	Smooth Rectangle
Dashed	GTL(m35)	26,000	0.30	0.25	1.38	Ribbed Rectangle
Dash-Dot	GTL(m45)	25,000	0.28	0.30	1.40	Smooth Square

Figure 4.4c: Square Model Trailing/Leading Nu Rotational Effects at Re = 25,000

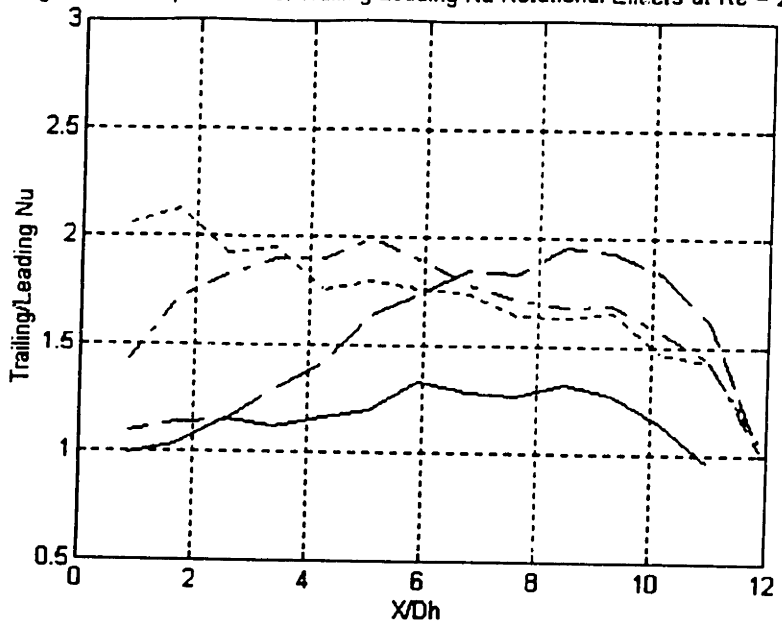

Key for Figure 4.4:

Line	Origin	Re	Ro	Δρ/ρ	B
Solid	GTL (m46)	26,000	0.14	0.32	0.39
Dashed	GTL (m45)	25,000	0.28	0.30	1.40
Dash-Dot	GTL (m44)	25,000	0.41	0.27	2.76
Dotted	GTL (m43)	25,000	0.64	0.22	5.59

Figure 4.12c: Ribbed Rect. Trailing/Leading Nu Buoyancy Parameter Variations

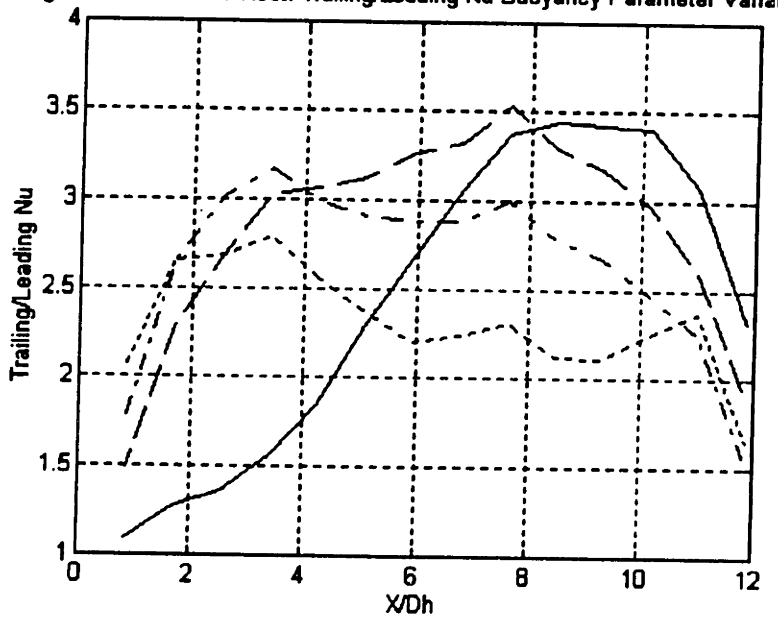

Key for Figure 4.12:

Line	Origin	Re	Ro	Δρ/ρ	B
Solid	GTL(m33)	26,000	0.12	0.30	0.27
Dashed	GTL(m34)	24,000	0.21	0.26	0.72
Dash-Dot	GTL(m35)	26,000	0.30	0.25	1.38
Dotted	GTL (m36)	26,000	0.53	0.21	3.63

4.6.2 Inlet Condition Effects

Figures 4.15a-b show the differences in the inlet region due to the way the flow enters the model. For the smooth square test section the flow entering the test section appears to significantly enhance the heat transfer near the inlet. This does not appear to be the case for the rectangular model. The data also shows that for the square model, at a practically stationary data set with Ro = 0.05, the trailing and leading Nusselt numbers are about 1.5 and 1.25 times the Nusselt number based on the Dittus-Boelter correlation $Nu_\infty = 0.023*Re^{.8} * Pr^{.4}$, which is a correlation for fully developed flow in stationary, circular channels.

Figure 4.15a: Inlet Region Trailing Surface Varying Geometries

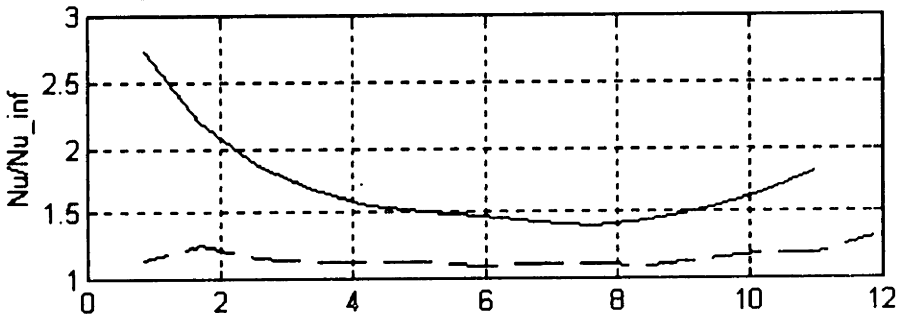

Figure 4.15b: Inlet Region Leading Surface Varying Geometries

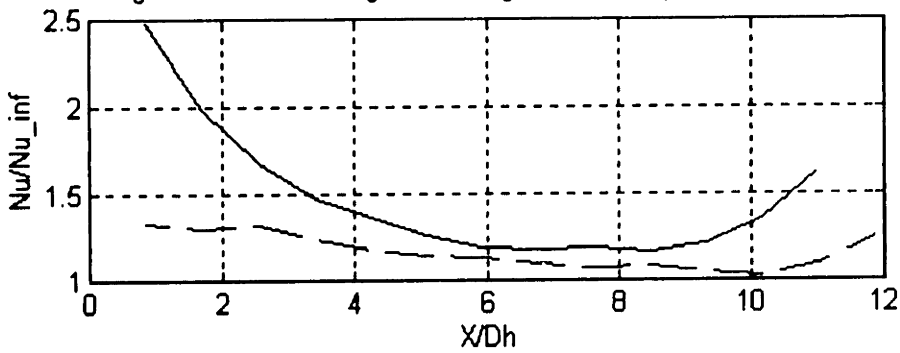

Key for Figure 4.15:

Line	Origin	Re	Ro	Δρ/ρ	B	Model
Solid	GTL(m23)	68,000	0.05	0.24	0.03	Smooth Square
Dashed	GTL(m49)	53,000	0.11	0.31	0.24	Smooth Rectangle

Chapter 5
Conclusions

An experiment was devised to examine the effects of rotation on the first passage of a convective cooling system. The external heat transfer to the passage was simulated by imposing a constant heat flux to the passage walls. Rotational effects were induced by rotating the model in an orthogonal mode. The experiment used an infrared detector and an imaging system to measure the wall temperature. As a result of the technique used to measure the wall temperature, the experiment was able to determine the heat transfer coefficient in regions that are approximately 50 times smaller than previous experiments were able to obtain.

The experimental technique was validated by comparing the GTL results with the results obtained by Han, Guidez and Wagner. The GTL data was consistent with the results reported by each researcher where they overlap in dimensionless parameters. In comparing the Han data and the GTL data, the magnitude and radial variation of Nu/Nu_∞ was examined for both the leading and trailing surfaces. The GTL data was in good agreement with the Han data, with any differences between the two cases being within experimental error. For the Guidez results, the GTL Nu/Nu_∞ for the leading and trailing surface, at an X/Dh of about 7.5, was compared to the results published by Guidez for a series of rotation numbers. The data showed that the GTL data was consistent with the Guidez results. In comparing the Wagner data and the GTL data, the magnitude and radial variation of Nu/Nu_∞ was examined for both the leading and trailing surfaces. The GTL trailing surface was directly compared to the Wagner trailing surface but the GTL leading surface was multiplied by 0.5 to account for the difference between the constant temperature and constant heat flux experiment. After the GTL data was adjusted to account for the differences between the experiments, the GTL data showed excellent agreement with the data published by Wagner.

The experiment was used to perform tests on three models, a smooth square tube, a smooth rectangular tube and a ribbed rectangular tube. Conclusions based on the data obtained for the models are highlighted as follows:

Reynolds Number Variations:

Presenting the data in terms of Nu/Nu_∞, where Nu_∞ is based on the Dittus-Boelter correlation for fully developed flow in stationary, circular channels, was useful in

removing most of the effects caused by variations in Reynolds number. Data for the square test section ranging from Reynolds number of 25,000 to 110,000 showed the leading and trailing Nusselt number to have the same trend and close to the same magnitude.

Inlet and Outlet Region:

Data for the square test section indicated an enhancement of the heat transfer at the inlet and outlet of the model. The inlet enhancement typically relaxed by an X/Dh of about 3 and the outlet region began at about and X/Dh of about 10. The enhancement near the inlet and the outlet of the model is not fully understood. However, it is suspected that the inlet enhancement is due to the flow impinging on the inlet surfaces and that the outlet enhancement is related to the adjustment in pressure to match the pressure in the exit plenum. Enhancement near the inlet and the outlet of the rectangular models was not apparent.

Density Ratio, Rotation Number and Buoyancy Parameter Variations:

It was found that at rotation numbers of about 0.30 variations with density ratio for the square model are significant and that the buoyancy parameter was able to compare data from different combinations of density ratio and rotation numbers. The effect of density ratio increases with increased rotation.

Increased Buoyancy Parameter:

In general, the data for the square model, smooth rectangular and ribbed rectangular model, showed an increase in heat transfer with increasing buoyancy parameter for both the leading and trailing surfaces. Further, the peak in the trailing/leading Nu shifted from the inlet to the outlet with increased buoyancy parameter for both the square model and the ribbed rectangular model. The shift is a result of the Coriolis driven flow developing faster and the buoyancy force interacting with the cross stream flows.

Increase in Aspect Ratio:

As the aspect ratio was increased from 1 to 3.3, the trailing/leading Nu became larger. This is an indication of the Coriolis driven cross stream flows being less effective on the leading surface of the rectangular channel.

Rib Enhancement:

The data for the ribbed rectangular model showed a significant enhancement of heat transfer as compared to the smooth rectangular model results. At a moderate buoyancy parameter the Nusselt number ratio for the ribbed model was 1.5 to 2.5 times larger than the ratio for the smooth rectangular model. The ribs create vortices near the ribs that are more effective in transporting the heat from the wall to the bulk flow. The trailing/leading Nu was about the same for the ribbed rectangular and smooth rectangular model at a moderate buoyancy parameter (~1.5).

Heat Transfer Maps:

The heat transfer maps that were created using the resolution of the experiment show how the side surfaces provide the continuation from the trailing surface to the leading surface. In the maps, the decrease in heat transfer traveling on the side wall from the trailing surface to the leading is an indication of the increase in flow temperature as the Coriolis cross stream vortices pass the side walls. Further, the heat transfer maps are symmetrical which implies that the internal flow is also symmetrical. In addition the heat transfer maps show signs of the interaction between the Coriolis and buoyancy forces.

Appendix A
Data Acquisition

A.1 Introduction

There are two types of runs that are performed with the facility. Either a calibration run or a test run. In either case the scanning of the test section is controlled by a computer program. A scan involves collected data for each surface of the model at 15 radial locations. The first radial location is at the inlet of the model and each subsequent pass is at a radial increment of 0.25 in. The program which controls the scanning process, collects high speed data as well as low speed data. While the computer program is scanning, other operating conditions are monitored and recorded manually. The next two sections describe the data that is collected manually and by the computer, as well as the equipment used throughout the experiment. The third section describes the imaging system and infrared detection system used.

A.2 Manual Data Acquisition

A Welder power supply, with a maximum current of 1500 amps, controls the current to the test section. The actual current level, however, is measured to within 2% using a TIF 1000 DC ampmeter. A 7.5 HP US Electrical Motors variable speed motor powers the rotor. The speed of the rotor is determined roughly with a 5314A Universal Counter and more accurately with a computer routine. Both methods employ the pulses emitted by the BEI L25G-500-ABZ-7404-ED15-5 optical encoder which is mounted on the shaft.

A Blackmer oil free compressor, with a pressure ratio of 7, circulates the flow. The Freon-12 pressure is measured outside of the vacuum chamber using Robinair pressure gages. The temperature of the Freon leaving the compressor, as well as at the inlet and outlet of the channel, are measured using K-type thermocouple wires that are hooked up to a Monogram Omega temperature reader. The Freon mass flow rate is measured using a F. & P. Co. Precision Bore Flowrator Tube No. FP1/2-35-G-10/55.

The vacuum is maintained by a Stokes 149H-11 Microvac Pump.

A.3 Computer Controlled Data Acquisition

The scanning of the test section is controlled by a C compiled routine that operates on a Dell 450 DE/2DGX personal computer. The routine positions the vertical and horizontal stepper motors in a specified sequence. The routine also determines the rotor speed, collects high speed data and collects low speed data. Two ADTEK AD830 data acquisition cards are used for the low and high speed data collection.

A feedback loop is used to position the imaging system. The vertical stage is driven by a SLOSYN M091-FC09 stepper motor with a step resolution of 0.005 steps/in. The horizontal stage, however, is driven by combining a SLOSYN HS25 (M062-LS03 equivalent) stepper motor with a step resolution of 0.001 steps/in and a Warner Electric MCS-2007 Linear Actuator. (The linear actuator is manually positioned and was added to the horizontal slide to enable a larger range of motion.) Each SLOSYN motor is connected to a 440-EPI indexer which translates the computer commands into pulses that move the motor. The computer commands are a string of letters and numbers that tells the indexer how many steps, in what direction and how fast the motion should be. Communication between the indexer and computer is through an RS232 serial port at a rate of 1200 baud, no parity, 8 bits, 2-stop bits. When not in motion the indexer, by default, commands a holding torque on the stepper motor. This holding torque significantly interferes with the IR signal and, as a result, is turned off when the motor is not in motion. A linear potentiometer, attached to each stage, identifies the location of the stage. The position of the imaging system is adjusted until the voltage from the potentiometers agrees with the desired position within 0.005 in.

The high and low speed data acquisition is performed using two ADTEK AD830 data acquisition boards. The main computer program independently initializes and configures each board by calling ADTEK written subroutines that set the frequency of data collection, set the desired buffer size, enable certain channels, and set the triggering. The low speed data, consisting of the linear potentiometer signals, is collected at a frequency of 24 kHz. The acquisition of the high speed data, consisting of the IR signal and Channel A of the optical encoder, is triggered by the optical encoder index pulse and is collected at a rate that maintains a 0.02 in spacing between data points. The rotor speed, which is required in order to determine the proper frequency that will

supply 0.02 in spacing, is calculated by collecting Channel A data points at a set frequency of 333.3 kHz and counting the number of pulses detected in a certain amount of time.

A.4 Imaging and Detection Systems

The primary imaging system consists of two spherical mirrors. The primary mirror is a concave spherical mirror that has a radius of curvature of 150 mm, and a diameter of 100 mm. A 26 mm. aperture was drilled in the center of the primary mirror. The secondary mirror, a convex spherical mirror, has a radius of curvature of 138 mm and a diameter of 50.8mm. The primary imaging system has a magnification of about 1.1, in which an element that is 1.1 mm wide is focused onto the 1 mm wide detector. The distance from the detector to the surface of interest needs to be 334.4 mm for the image to be in focus. Other critical distances are labeled in Figure A.1. The distances are measured from the vertex of each curved mirror.

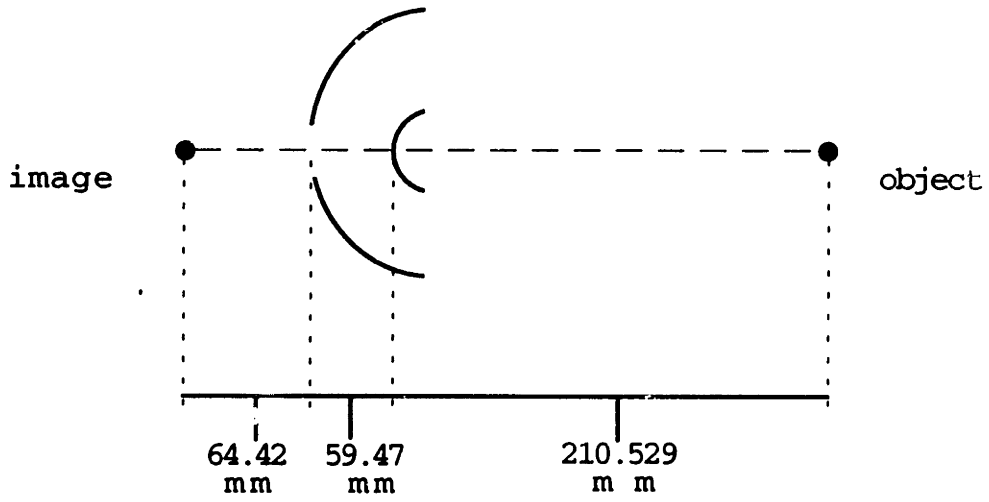

Figure A.1 Imaging system optical distances

Table A.1 Mirror Dimensions

Mirror	Shape	Size	Radius of Curvature	Manufacturer
Primary	Spherical Concave	100 mm diam. 26 mm aperture	150 mm	OPCO Laboratory Inc.
Secondary	Spherical Convex	50.8 mm diam.	138 mm	Virgo Optics
Flat	Flat	cut to fit mounts (~96.5x83.5mm)	∞	Newport

All of the mirrors are coated with protected aluminum, AlSiO, which has a reflectance of greater than 97% in the infrared regime. The surface quality of the mirrors is not critical since IR waves are not effected much by small surface imperfections. A surface quality of 3λ and a scratch/dig of 60/80 are acceptable. Although surface imperfections or even slight cracks do not effect the image, a coat of film on the surface of the mirror will potentially distort the image.

An Electro-Optical Systems, Inc. HgCdTe (MCT Series) infrared detector Serial 49409 is used in the experiment. The dewar, containing the detector is 6.75 inches long and has a holding time for the liquid nitrogen of 12 hours. An AC coupled preamplifier is internal to the dewar and has a high/low gain switch. The low gain of 100 and a high gain of 1000 has a bandwidth of 5-500 kHz and 5-50 kHz respectively. The amplifier is set to the low gain since the high gain signal is not fast enough at 30 rev/sec. Other significant qualities of the detector are listed in the table below.

Table A.2 Infrared Detector Specifications

Manufacturer	Electro-Optical Systems, Inc.
Area	1mm x 1mm
Dewar Window	ZnSe
FOV	60 NOM. deg
Peak Wavelength	12.5 μ m
Cut-Off Wavelength	14.5 μ m
Noise Equivalent Power	1.7x10e-12 W/Hz$^{1/2}$
D* (peak, 10kHz, 1Hz)	5.7x10e10 cm-Hz$^{1/2}$/W
Responsivity (Blackbody)	2.4x10e5 V/W @ HI gain
Responsivity (Peak)	5.7x10e5 V/W @ HI gain
Noise	1.0x10e-6 V/Hz$^{1/2}$
Time Constant	300 nsec

Appendix B
Experimental Procedure

B.1 Focusing Run

Before calibration and test runs are performed on a model, a focusing run is made. The focusing run is used to determine where the imaging system should be placed in order for the image of the surface to be in focus. This distance, or focal position, is different for each surface. The focusing run keeps the vertical stage stationary and moves the horizontal stage through a range of positions. During a focusing run the model is heated but cooling flow is not passed through the channel. Instead, material (boron nitride) is placed inside the model to promote a uniform circumferential surface temperature and, correspondingly, a square IR data signal from the model. The imaging system is in focus when the number of points seen for the model is consistent with the model width and magnification of the imaging system. (Recall that the frequency of the high speed data collection is set to maintain a 0.02 in spacing between points.) Further, when the system is in focus, the drop from either end of the model is the most pronounced. For example, the solid line below is in focus.

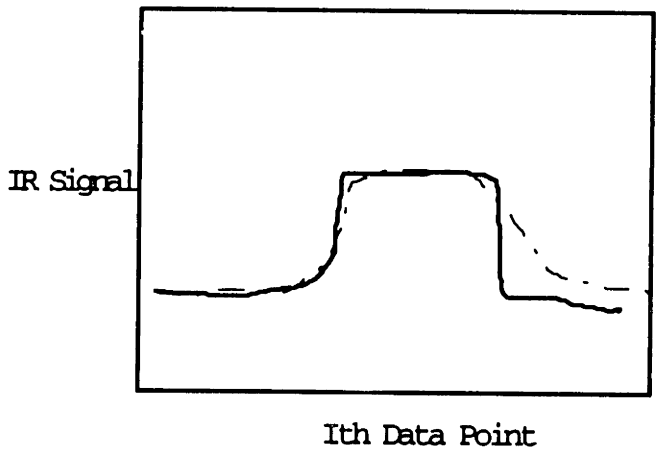

Figure B.1 Example of Focusing Run Data. (the solid line is in focus)

A focal position is determined for each surface independently. However, since the location of the flat mirrors behind the model is known, the difference between the front focal position and the focal position to any other surface can be geometrically

estimated. (see below). The focal positions are confirmed when the differences based on the results of the focusing run agree with the geometrical differences. For example, the table below shows the geometric and focusing run determined focal positions. The focusing run is performed only once each time a model is installed on the rotating shaft. The resulting focal positions are then used to focus the imaging system during subsequent calibration and tests runs.

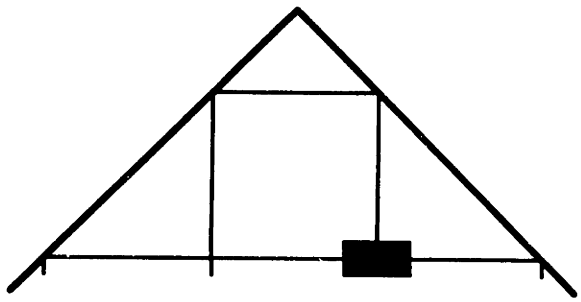

Figure B.2 Schematic of the increase in distance the radiation travels

Rectangular Smooth Test Section

Difference	Based on Focusing Run	Based on Geometry
Trailing - Front	0.715	0.700
Leading - Front	1.64	1.718
Back - Front	2.84	2.931

B.2 Calibration Run

During a calibration run the model is heated but cooling flow is not passed through the test section. Instead a boron nitride plug is placed in the test section. The 'plug' helps to ensure that the circumferential temperature is uniform and that the principle heat loss is by conduction out the ends. Under these conditions, the plug thermocouples, which are located at three known radial locations, are used to estimate the temperature of the test section over the entire surface. A constant flow of current is passed through the test section and the plug thermocouple readings are monitored. The model scan is started when the temperature of the model approaches a pseudo-steady state condition which is assumed to be when the thermocouple readings vary less than $2^{o}F$ in a five minute period. At the beginning of each surface scan, the current level, thermocouple readings, and the rotor speed are manually recorded. Although typically, each thermocouple temperature varies less than $2^{o}F$ over the entire scan, data is considered acceptable if the thermocouple readings vary up to $5^{o}F$ over the entire scan.

Typically, five calibration runs are performed, each run corresponds to a current level for which the center thermocouple reads a temperature of either 250, 300, 400, 500 or $600^{o}F$.

B.3 Test Run

During the actual test run, current is passed through the model and the oil free compressor circulates the Freon 12 at the desired pressure and mass flow rate. The amount of current that passes through the model affects the model surface temperature and also the temperature rise of the cooling flow. Since the cooling flow travels through counterflow heat exchangers the temperature rise of the cooling flow also affects the bulk inlet temperature. The scan of the model is initiated when the bulk inlet and outlet temperatures reach a pseudo-steady state condition which is assumed to be when the thermocouple readings vary less than $2^{o}F$ in a five minute period. At the beginning of each surface scan the current level, the thermocouple readings, the mass flow rate, the compressor outlet pressure, and the rotor speed are manually recorded. Due to the number and type of variables that are involved in the experiment, such as the current, mass flow rate, flow pressure, and flow temperature, the data taken during a test run scan is considered acceptable if the mass flow rate varied less then 2%, flow pressure varied

less than 2 psi, flow temperature varied less than 5^{O}F and the current varied less than 1 amp over the entire scan.

Appendix C
Data Reduction

C.1 Stripping the Data

When a model scan is performed, the imaging system is focused by the computer on one surface for a series of radial positions. Although, the imaging system is focused on one surface at a time it detects the three remaining surfaces, albeit out of focus, as indicated in Figure C.1. Shown in Figure C.1 is the site one would see when looking at the model with the flat mirrors placed behind the model. The shape below "F" represents the front surface of the model. The shape below "T" represents the image of the trailing surface as it is reflected off the right side mirror. Likewise, "L" and "B" are the images of the leading and back surface respectively. The leading surface is reflected off the left side mirror and the back surface is reflected off both the right and left side mirror. Each time the model makes a revolution the imaging system will sense the radiation from each surface of the model. However, only one surface will be in focus, the image of the other surfaces will be distorted or not detectable. Keep in mind that the imaging system collects a cone of radiation from each point on the surface. Only if the distance between the detector and the surface, including the distance the radiation travels as it gets reflected, is the correct focal length will the image that gets focused on the detector represent the true surface conditions. (Note: When we look at the front surface and the model reflections we see focused images, however the imaging system used in the experiment and our eyes are two different types of optical systems.)

256 data points of the IR signal are collected and stored each time the model rotates by the field of view of the infrared detector. Data collection always starts at the same location since it is triggered by the index pulse of the optical encoder. The number of points collected is large enough for the image from all four surfaces to be collected. The computer program averages 10 such passes and writes the average to a file. Of the final 256 data points only 9 to 40 of these points correspond to the actual focused model data on a particular surface. (The number of model points depends on the surface width of the model, the magnification of the imaging system and the frequency of data collection.) Another program is used to extract the focused model data and store the "stripped" data in a different file.

This section discusses the procedure to separate the data points that correspond to the surface of the model in focus from the data that is recorded.

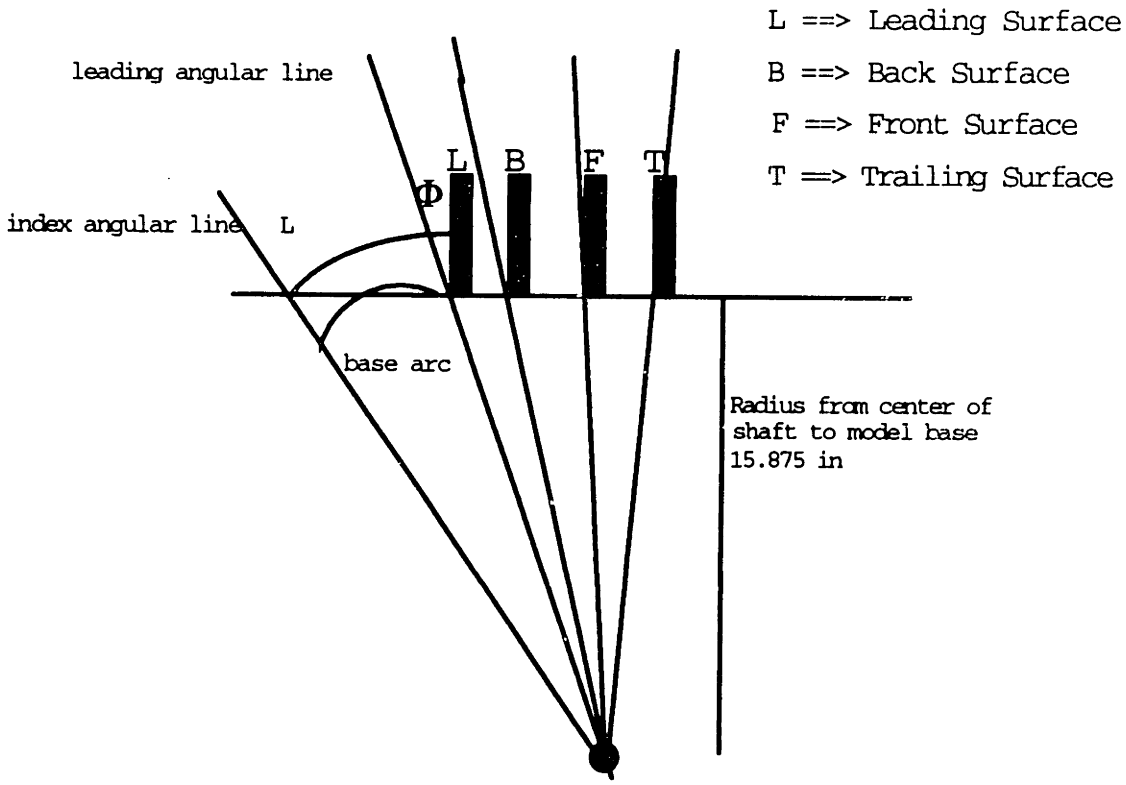

Figure C.1 Frontal view of the model and the model images, as well as the arc length definitions used in stripping the data. (Not to Scale)

The general procedure of the stripping process is in terms of arc lengths. Since data collection is triggered by the encoder index pulse, each arc length is started at the index angular line of the optical encoder index pulse, A first approximation to the start point of each model surface is made by estimating the arc length between the index angular line and the left most point on the base of each model surface. The base arc length for the leading surface is shown in Figure C.1. The arc length L is updated based on the radial position of the pass. A refinement to this estimation of L is made by calculating the arc length between the angular line corresponding to the base of the particular surface, and the beginning of the surface at the actual radial location. The leading surface angular line is pictured in Figure C.1. Adding this refinement to the base arc length gives the distance

from the index pulse to the first point on the model for each radial position. The total arc length directly corresponds to the number of points collected before the model surface since data is collected at a rate such that there is 0.02 in (0.5 mm) arc length spacing between points for each height level. Knowing the start point of the model surface and the number of points per model width these data points are extracted from the 256 points and plotted for visual inspection. The stripping of the data is further refined manually to ensure that only points corresponding to the model surface are used in the data reduction process.

C.2 Calibration Process

A major step in the data reduction process is converting the test run IR voltage to temperature data. The process starts with the calibration run in which a surface temperature distribution is calculated from the three radially located thermocouple readings. It is assumed that the circumferential model temperature is constant and that the radial temperature is parabolic due to conduction losses out the ends. Taking the three thermocouple readings, a parabolic curve is generated which gives the temperature of the model at every radial location. Since the circumferential temperature is assumed to be constant, the radial temperature distribution can be applied to each surface of the model.

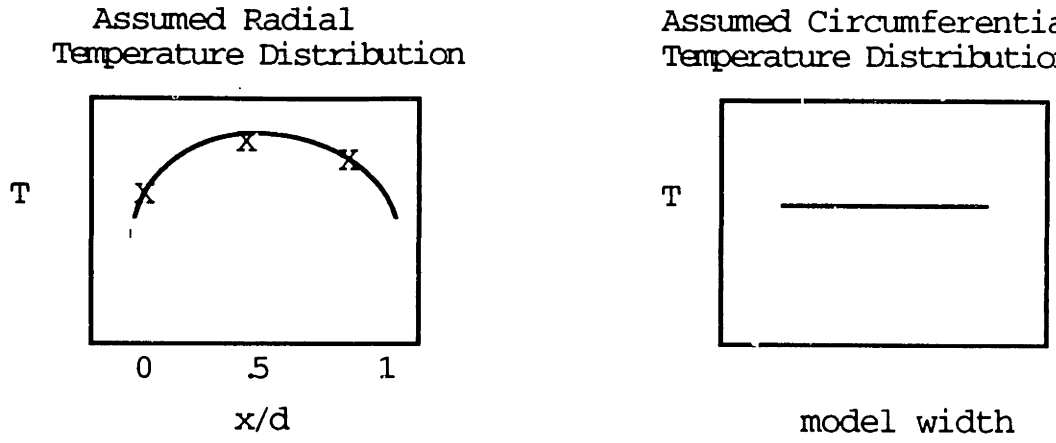

Figure C.2 Assumed Radial and Circumferential Temperature Distribution

Using the calculated surface temperature distribution, a temperature-voltage pair is assigned to each location on the model. Using the five calibration runs, five temperature-voltage pairs are obtained for each location on the model. A cubic spline function based on the five temperature-voltage pairs, is generated and is used to convert the test run IR voltage to temperature. Since a different cubic spline function is found for each location on the model the calibration process is considered to be a local calibration.

The cubic spline function generated for each location, is based on the relation $V = \epsilon_{factor} T^4$, since it is known that the radiation from each point on the surface scales with temperature raised to the fourth power. Although the relation is linear with T^4, a cubic spline fit was used instead of a linear fit since the detector output voltage is not precisely linear with radiation. The detector has a slightly different percent transmission depending on the wavelength of the radiation.

Another important aspect of the calibration being a local calibration is that the radiation from each location travels a unique path and may be effected by certain geometric effects and/or mirror losses. These effects/losses are factored out in the calibration process. Below is a plot showing a local average emmisivity factor based on five calibration runs which were used to reduce the smooth rectangular model data. It is important to remember that this emmisivity factor is not the emmisivity of the surface, it is the factor that relates the voltage to the temperature raised to the fourth power. The

plot shows how the emmisivity factor changes circumferentially at each radial location. Each line is at a different radius on the model and represents the surface unwrapped, going from the leading, to the front, to the trailing, to the back and to the leading surface. The emmisivity factors are the lowest at the inlet of the test section, and increase to almost constant level. (Data was not collected at the extreme outlet of the test section.) Primarily, the plot shows that circumferentially around the model the front surface and back surface emmisivity factor is nearly constant indicating that the losses from the side mirrors are negligible. The decrease in the trailing surface as well as the decrease and variation in the leading surface emmisivity factor are due to the path the radiation travels and gets reflected off the side mirrors. For the leading and trailing surfaces not all of the radiation is reflected into the primary imaging system. Further, the emmisivity factor is lower near the inlet since some of the radiation is blocked by the mount the model is attached to. (A decrease in emmisivity would also occur at the outlet of the test section when the top support structure begins to block the radiation.) These variations in emmisivity factor are taken into account by performing the local calibration.

Figure C.3

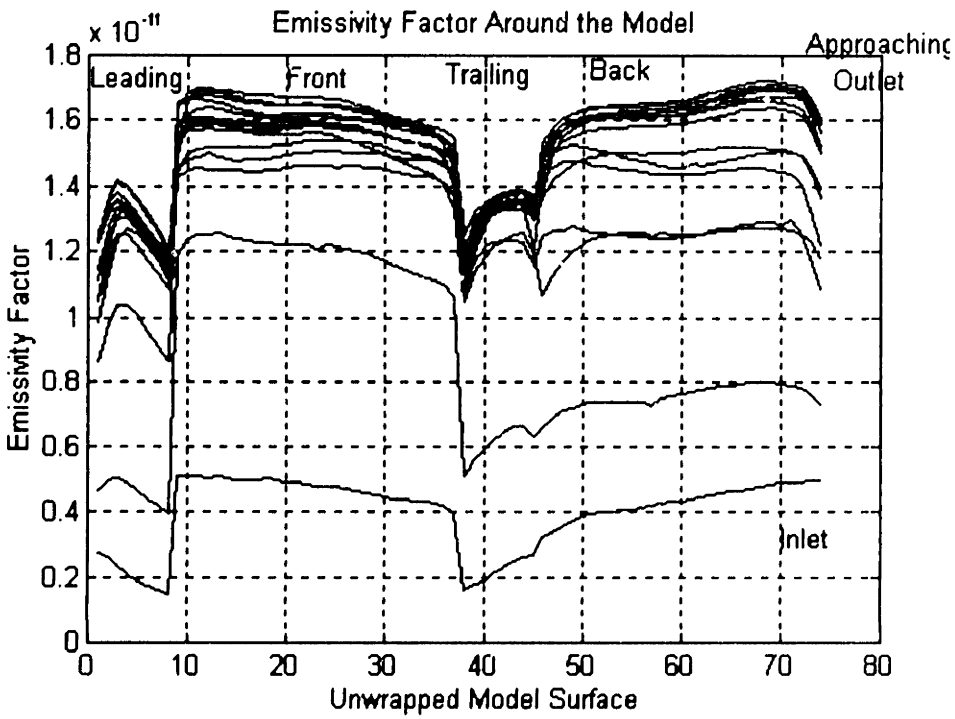

C.3 Energy Balance

Once the temperature for each location is determined an elemental heat balance is applied to the model. When performing the elemental balance it is assumed that the model is uniformly heated and the inner wall and outer wall temperatures are equal.

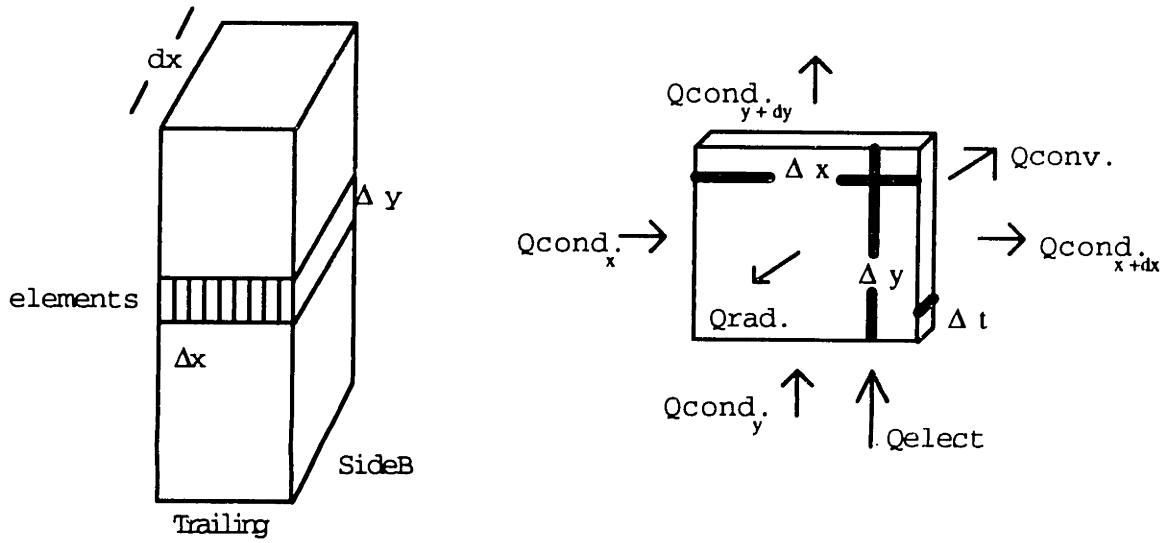

Figure C.4 Example of an elemental energy balance

The overall energy balance for an element relates the energy into the test section to the energy leaving the test section. The forms of heat transfer included in the formulation are shown above. External convection is not included since the tests are performed in a vacuum and the levels would be negligible. The heat balance equation in it's most general form is written below. The conduction term is the summation of the conduction of that element to the four elements surrounding the cell of interest. ΔS and ΔD can be either Δx or Δy depending on the direction of the conduction.

$$(I^2R_f/A_f)*\Delta x*\Delta y = -\Sigma\, k\,(\Delta T/\Delta S)*\Delta t*\Delta D + h(Tw - Tb)*\Delta x*\Delta y + \varepsilon\sigma(T^4-T^4_0)$$

In general the radial conduction and radiative terms were found to be negligible. The heat transfer coefficient is determined by equating the electric energy to the internal convective and lateral conductive energy. The lateral conduction, however, is assumed to

travel from the leading surface to the trailing surface. In the experiments, when the model is rotating, the leading surface temperature is larger than the trailing surface temperature and the side temperatures provide the continuity between these two surfaces. The temperature profile on the side surfaces is generally linear. Theoretically the side surface temperature should match the leading surface temperature and then decrease to the trailing surface temperature. As a result, the lateral conduction is calculated based on the temperature gradient on the side walls and is uniformly subtracted from the leading surface and added to the trailing surface. This simplification is made since the temperatures around the corners of the model were found not to match exactly, even though physically the temperatures should match. Any slight mismatch in the temperature, or errors in stripping the data, will cause unreasonable conduction terms.

In the above equation, Tb is the bulk temperature of the coolant at the radius of interest. The measured inlet and outlet bulk temperatures are used to calculate the intermediate bulk temperatures by assuming that the temperature from the inlet to the outlet increases linearly. Once this calculation has been made, the last unknown is h, and the above equation is solved for h. The final results are given as Nu/Nu_∞, where $Nu = hd_h/k$ is the local Nusselt number and $Nu_\infty = 0.023*Re^{0.8}*Pr^{0.4}$ is the correlated Nusselt number for fully developed turbulent flow in smooth, circular, stationary channels. The transport properties μ and k, that are needed in the calculations, are based on the temperature of the bulk flow at the radial level of interest.

In addition, when applying a power balance to the entire model, the joule heating applied to the model should go into the temperature rise of the bulk flow according to the relationship below. In the data reduction process, both terms are calculated and compared to check the quality of the results.

$$mdot*C_p(Tout-Tin) = I^2R_f$$

Appendix D
Error and Uncertainty Analysis

D.1 Discussion

We estimate that the experiment determines the absolute magnitude of the heat transfer coefficient to ± 44 W/K of the true value. For a typical heat transfer coefficient of 346 W/K this implies the accuracy of the data to approximately 13% accurate. The shape of the heat transfer distribution, however, is much more accurate, on the order of 5%, since errors in the bulk temperature, calibration process, and joule heating measurement would affect points in the same region in the same manner.

The method used to calculate the uncertainty, in the magnitude of the heat transfer results, was based on the method highlighted by Kline & McClintock. In their method each measured variable is described by a mean value plus or minus some uncertainty with a given confidence indicator. For example, the bulk temperature would be 340°K ± 2°K (20 to 1), where the mean value is 340°K and the experimenter is confident at 20 to 1 odds that the true value is within ± 2°K of the measured value. Kline & McClintock [8] proposed a way to combine the uncertainty of each measured quantity to represent the uncertainty in the final variable. If the result R is a function of variables $\upsilon_1, \upsilon_2, \upsilon_3, \ldots \upsilon_n$ with uncertainties $\omega_1, \omega_2, \omega_3, \ldots \omega_n$ then the uncertainty in the result can be described by:

Equation D.1

$$\omega_r = [\ (\partial R/\partial \upsilon_1 * \omega_1)^2 + (\partial R/\partial \upsilon_2 * \omega_2)^2 + \ldots + (\partial R/\partial \upsilon_n * \omega_n)^2\ ]^{1/2}$$

Recall, that an elemental heat balance was applied to each element (figure C.4). When equating the energy entering the element to the energy to the energy leaving the element the correct form of the equation is:

$$Qelect + Qcond_x = Qconv + Qcond_{x+dx}$$

where $Qcond_{x+dx} = Qcond_x + \partial Qcond_x/\partial x * dx$

Combining and rewriting these two equations the elemental equation becomes:

$$(I^2R_f/A_f)*\Delta x*\Delta y = -\partial/\partial x(k\partial T/\partial x)*\Delta x*\Delta y*\Delta t + h(Tw - Tb)*\Delta x*\Delta y$$

This equation is equivalent to the form below when the first term on the right hand side is evaluated by using a centered difference approximation.

$$(I^2R_f/A_f)*\Delta x*\Delta y = -\sum k\,(\Delta T/\Delta x)*\Delta t*\Delta y + h(Tw - Tb)*\Delta x*\Delta y$$

The resulting heat transfer coefficient, h, in terms of the measured values I, Tw, Tb and $\partial^2T/\partial x^2$ is then

$$h = [\,(I^2R_f/A_f)*\Delta x*\Delta y + k\partial^2T/\partial x^2*\Delta x*\Delta y*\Delta t\,] / ((Tw - Tb)*\Delta x*\Delta y)$$

In the formulation the current I, model resistance Rf, the second derivative of temperature $\partial^2T/\partial x^2$, the wall temperature Tw, and the bulk temperature Tb were taken to be the measured variables. Table D.2 lists these measurables with an associated typical value and uncertainty. In determining the uncertainties, a worst case error was given. In most cases the bulk temperature and wall temperature are expected to be accurate within ±4 °K and 2 °K respectively.

Table D.3 lists the partial derivatives used in the calculation and table D.1 lists other related parameters. The uncertainty in the heat transfer coefficient ω_h was calculated to be ± 44 W/K. Assuming the h = 346 W/K then, the accuracy of the experiment is better than 13 %. The actual value of the heat transfer coefficient will vary considerably based on the Reynolds number of the flow and the rotation rate. At the lowest Reynolds number of 25,000 and a Nusselt number ratio of 2 the actual heat transfer coefficient is on the order of 150 W/K (29% accurate), where as for the largest Reynolds number case of 100,000 and a Nusselt number ratio of 2 the actual the actual heat transfer coefficient is on the order of 440 W/K (10% accurate).

Regardless of the accuracy of the magnitude of the heat transfer, the accuracy of the spatial variation in heat transfer between points is accurate to within 5%. When examining the heat transfer distribution, errors due to inaccuracies in measuring the amount of joule heating, bulk temperature and wall temperature, will have the same affect within a region of points. As a results, these errors are canceled out when looking at the distribution of the heat transfer.

However, due to the stripping process, points at the edges of the surfaces are the most questionable. If the data is not stripped correctly, meaning the data is off by one point, incorrect temperatures may be calculated for the point that is off. Incorrect stripping does not affect the interior points since one point is approximately 1/2 mm in

width and the resolution of the imaging system is on the order of 1mm. Further, data for the first and second height level of the model (X/Dh = 0.0 and 0.85) are questionable, since almost 50% of the radiation emitted from a point on the surface is blocked by the mount.

A comment also needs to be made concerning the bulk temperature measurements. Thermocouples are placed at the inlet and outlet of the channel. At the outlet of the channel, cross stream flows have had a chance to develop. It is not precisely known how these cross stream flows, passing by the thermocouples, affect the outlet bulk temperature measurement. Similarly, for the large rotation numbers, if recirculation occurs, it is no longer certain that the inlet thermocouples are measuring the inlet bulk temperature. However, for each test case the energy corresponding to the bulk temperature rise and the joule heating are calculated and compared. It was found that the two quantities of energy, which should be equal, were almost always within 87% of each other.

Table D.1 Sample Values

Variable	Value
Δx	5.35e-3 m
Δy	6.35e-3 m
Δt	2.54e-4 m
A_f	3045e-6 m^2
k	20 W/mK
h	346 W/K

Table D.2 Measurable, Mean and Uncertainty

All at 20 to 1 odds

Measurable	Mean	Uncertainty
I	100 A	3 A
$\partial^2T/\partial x^2$	3.5e6 $^oK/m^2$	0.7e6 $^oK/m^2$
Tw	500 ^oK	5 ^oK
Tb	340 ^oK	10 ^oK
Rf	0.0169	0.0001
mdot	0.0049 kg/sec	0.0002 kg/sec
ΔTb	58 ^oK	5 ^oK

Table D.3 Partial Derivatives

Partial Derivative	Value
$\partial h/\partial I$	6.94
$\partial h/\partial(\partial^2 T/\partial x^2)$	3.2e-5
$\partial h/\partial Tw$	2.86
$\partial h/\partial Tb$	2.86
$\partial h/\partial Rf$	20525
$\partial h/\partial mdot$	57143
$\partial h/\partial \Delta Tb$	2.86

Nomenclature

Greek Symbols

ε	= emissivity	
ε_f	= emissivity factor	($V/^oK^4$)
μ	= viscosity	($N\text{-}sec/m^2$)
ρ	= density	(kg/m^3)
$\Delta\rho/\rho$	= (Tw - Tb)/Tw = density ratio	
σ	= 5.67e-8 = Stefan Boltzman constant	($W/m^{2*}\ ^oK^4$)
Ω, ω	= angular velocity	(rad/sec)
ω	= uncertainty	

English Symbols

A_f	= surface area of the model	(m^2)
B	= $\Delta\rho/\rho * Ro^2 * R/d_h$ = buoyancy parameter	
C_p	= specific heat under constant pressure	($J/kg\ ^oK$)
d_h	= hydraulic diameter	(m)
h	= heat transfer coefficient	($W/m^{2*}\ ^oK$)
I	= current	(amp)
k	= thermal conductivity	($W/m^*\ ^oK$)
mdot	= mass flow rate	(kg/sec)
Nu	= hd_h/k = Nusselt number	
Nu_∞	= Nusselt number based on Dittus-Boelter correlation	
p	= pressure	(N/m^2)
Pr	= $\mu C_p/k$ = Prandtl number	
R	= distance from shaft to center to center of the model	(m)
Re	= $\rho v d_h/\mu$ = Reynolds number	
R_f	= resistance of the model	(Ohms)
Ro	= $\omega d_h/v$ = rotation number	
Tb	= bulk temperature	(^oK)
Tw	= wall temperature	(^oK)
x	= radial distance from the inlet	(m)
y	= circumferential distance	(m)

References

[1] Guidez, J., 1989, "Study of the Convective Heat Transfer in a Rotating Coolant Channel," ASME *Journal of Turbomachinery*, Vol. 111, pp 43-50.

[2] Hajek, T.J., Wagner, J.H., Johnson, B.V., Higgins, A.W., and Steuber, G.D, 1991, "Effects of Rotation on Coolant Passage Heat Transfer," NASA Contractor Report 4396, Vol. I

[3] Han, J.C., Zhang, Y.M., and Lee, C.P., 1991, "Augmented Heat Transfer in Square Channels With Parallel, Crossed and V-Shaped Angled Ribs," ASME *Journal of Heat Transfer*, Vol. 113, pp 590-596.

[4] Han, J.C., and Zhang, Y.M., 1992, "Effect of Uneven Wall Temperature on Local Heat Transfer in a Rotating Square Channel With Smooth Walls and Radial Outward Flow," ASME *Journal of Heat Transfer*, Vol. 114, pp 850-858.

[5] Hwang, G.J., and Kuo, C.R., 1993, "Experimental Study of Convective Heat Transfer in a Rotating Square Duct With Radial Outward Flow," ASME *Gas Turbine Heat Transfer*, HTD-Vol. 242, pp 53-60.

[6] Incropera, F.P. and DeWitt, D.P., *Introduction to Heat Transfer*, John Wiley &Sons, N.Y., 1985.

[7] Iskakov, K.M., and Trushin, V.A., 1985, "The Effect of Rotation on Heat Transfer in the Radial Cooling Channels of Turbine Blades," *Thermal Engineering*, 32 (2), pp 93-96.

[8] Kline, S.J., and McClintock, F.A., 1953, "Describing Uncertainties in Single Sample Experiments," *Mechanical Engineering*, Jan., pp 3-8.

[9] Morris, W.D., and Ghavami-Nsar, G., 1991, "Heat Transfer in Rectangular Channel With Orthogonal Mode Rotation," ASME Paper 90-GT-138.

[10] Prakash, C., and Zerkle, R., 1992, "Prediction of Turbulent Flow and Heat Transfer in a Radially Rotating Duct," ASME *Journal of Turbomachinery*, Vol. 114, pp 835-846.

[11] Wagner, J.H., Johnson B.V., and Hajek, T.J., 1991a, "Heat Transfer in Rotating Serpentine Passages With Smooth Walls and Radial Outward Flow," ASME *Journal of Turbomachinary*, Vol. 113 pp 42-51.

[12] Wagner, J.H., Johnson B.V., and Kopper F.C., 1991b, "Heat Transfer in Rotating Serpentine Passages With Smooth Walls," ASME *Journal of Turbomachinary*, Vol. 113 pp 321-330.

[13] Wagner, J.H., Johnson B.V., Graziani, R.A. and Yeh F.C., 1992, "Heat Transfer in Rotating Serpentine Passages With Trips Normal to the Flow," ASME *Journal of Turbomachinary*, Vol. 114, pp 847-857.